Louisiana Transportation Research Center

Final Report 657

Cost-Effective Detection and Repair of Moisture Damage in Pavements

by

Mostafa A. Elseifi, Ph.D., P.E.
Nirmal Dhakal
Hossam Abohamer
Ye Ma
Zia U. A. Zihan

LSU

4101 Gourrier Avenue | Baton Rouge, Louisiana 70808
(225) 767-9131 | (225) 767-9108 fax | www.ltrc.lsu.edu

TECHNICAL REPORT STANDARD PAGE

1. Title and Subtitle
Cost-Effective Detection and Repair of Moisture Damage in Pavements

2. Author(s)
Mostafa A. Elseifi, Nirmal Dhakal, Hossam Abohamer Ye Ma, and Zia U.A. Zihan

3. Performing Organization Name and Address
Department of Civil and Environmental Engineering
Louisiana State University
Baton Rouge, LA 70803

4. Sponsoring Agency Name and Address
Louisiana Department of Transportation and Development
P.O. Box 94245
Baton Rouge, LA 70804-9245

5. Report No.
FHWA/LA.17/657

6. Report Date
December 2021

7. Performing Organization Code
LTRC Project Number: 18-4P
SIO Number: DOTLT1000241

8. Type of Report and Period Covered
Final Report
05/2018 – 05/2021

9. No. of Pages
161

10. Supplementary Notes
Conducted in Cooperation with the U.S. Department of Transportation, Federal Highway Administration

11. Distribution Statement
Unrestricted. This document is available through the National Technical Information Service, Springfield, VA 21161.

12. Key Words
Flexible pavement; moisture damage; ground penetrating radar; pavement evaluation

13. Abstract
The major objective of this study was to evaluate the use of non-destructive evaluation (NDE) test methods to identify moisture damage in the field, to classify surface cracking in flexible pavements as top-down or bottom-up cracking, and to predict roughness conditions from surface images. NDE test methods evaluated in this study included Traffic Speed Deflection Device (TSDD) and Ground Penetrating Radar (GPR). In addition, the performance and cost-effectiveness of treatment methods including asphalt concrete (AC) overlay and chip seal were analyzed with and without moisture-induced damage. The study also developed a decision-making tool to identify top-down, bottom-up, and cement treated (CT) reflective cracking in in-service flexible pavements using Convolutional Neural Networks (CNN) model and Artificial Neural Networks (ANN). The developed CNN model was found to achieve an accuracy of 93.8% and 91.0% in the testing and validation phases, respectively. The ANN based decision-making tool achieved an overall accuracy of 92% indicating its effectiveness in cross-checking the prediction from the CNN model.

Measurements from the Rolling Wheel Deflectometer (RWD) were evaluated to identify pavement sections that may suffer from stripping damage. Statistical and ANN models that used RWD measured deflections and pavement characteristics were developed to predict the probability of stripping damage in the tested sections. A regression-based classification tree was also developed that is easy to interpret and is convenient for highway agencies for preliminary stripping evaluation. A moisture detection protocol was also developed based on GPR measurements as a noninvasive and continuous evaluation technique to detect moisture damages in flexible pavements. A novel GPR-based indicator, known as the Accumulating In-layer Peaks (AIP), was introduced to detect stripping damage in asphalt pavements. The AIP predicted accuracies for stripped and non-stripped sections were 82% and 96%, respectively, indicating its effectiveness to detect AC stripping damage in flexible pavements.

The study also evaluated the effects of AC stripping damage on the performance and cost-effectiveness of chip seal and AC overlays in pavement maintenance and rehabilitation. Results showed that for chip seal, moisture damage negatively affected the performance of the sections especially for low traffic volumes. For AC overlays, moisture-induced damage significantly affected the long-term pavement performance at all traffic levels. On average, moisture-induced damage decreased the extension in pavement service life and cost-effectiveness by 4.6 years and 0.5%, respectively.

The study also employed CNN to classify pavement sections into different International Roughness Index (IRI) categories and to predict IRI values using Three-Dimensional (3D) pavement images. The developed CNN model classified pavement sections according to their roughness conditions with an accuracy of 93.4% and 89.6% in the training and validation stages, respectively. In addition, a CNN model was developed for the prediction of IRI values from 3D pavement images. The model yielded accurate predictions with a coefficient of determination (R^2) of 0.985 and an average error of 5.9%.

Project Review Committee

Each research project will have an advisory committee appointed by the LTRC Director. The Project Review Committee is responsible for assisting the LTRC Administrator or Manager in the development of acceptable research problem statements, requests for proposals, review of research proposals, oversight of approved research projects, and implementation of findings.

LTRC appreciates the dedication of the following Project Review Committee Members in guiding this research study to fruition.

LTRC Administrator/Manager

Qiming Chen

Pavement Research Manager

Members

Eric Ponte

Chris Fillastre

Xingwei Chen

Mark Ordogne

Scott Nelson

Directorate Implementation Sponsor

Christopher P. Knotts, P.E.

DOTD Chief Engineer

Cost-Effective Detection and Repair of Moisture Damage in Pavements

By
Mostafa A. Elseifi, Ph.D., P.E.
Nirmal Dhakal
Hossam Abohamer
Ye Ma
Zia U. A. Zihan

Department of Civil and Environmental Engineering
Louisiana State University
Baton Rouge, LA 70803

LTRC Project No. 18-4P
SIO No. DOTLT1000241

conducted for
Louisiana Department of Transportation and Development
Louisiana Transportation Research Center

December 2021

Abstract

The main objective of this study was to develop non-destructive field-testing methods to identify moisture damage and to classify surface cracking in flexible pavements as top-down or bottom-up cracking. In addition, the effect of moisture damage on the performance and cost-effectiveness of asphalt concrete (AC) overlay and chip seal was evaluated. The study also developed a model to predict pavement roughness conditions based on digital images of pavement surface. A Convolutional Neural Networks (CNN) model and a decision-making tool using Artificial Neural Networks (ANN) were developed to identify top-down, bottom-up, and cement-treated (CT) reflective cracking in in-service flexible pavements. The CNN model was developed by modifying a pre-trained network, which was fitted, tested, and validated using 350 pavement images. Input variables for the ANN model were pavement age, asphalt concrete (AC) thickness, annual average daily traffic (AADT), type of base, crack orientation, and crack location. The developed CNN model was found to achieve an accuracy of 93.8% and 91.0% in the testing and validation phases, respectively. The ANN-based decision-making tool achieved an overall accuracy of 92% indicating its effectiveness in cross-checking the prediction from the CNN model in crack identification and classification.

The present study also evaluated the use of deflection measurements of a Traffic Speed Deflection Device (TSDD), namely the Rolling Wheel Deflectometer (RWD), to identify pavement sections that may suffer from stripping and moisture damage. Statistical and ANN models that use RWD measured deflections, pavement characteristics, and performance data as inputs were developed to predict the probability of stripping damage in in-service pavements. A regression-based classification tree was developed based on the available dataset that is easy to interpret and is convenient for highway agencies for preliminary stripping evaluation. A moisture detection protocol was also developed based on Ground Penetrating Radar (GPR) measurements as a noninvasive and continuous evaluation technique that can be used to detect AC stripping damage in flexible pavements. A Finite-Difference Time-Domain-(FDTD)-based simulation program was used to study the propagation of GPR signals in a stripped pavement. Based on this analysis, a novel GPR-based indicator, known as the Accumulating In-layer Peaks (AIP), was introduced to detect stripping damage in asphalt pavements. The AIP predicted accuracies for stripped and non-stripped sections were 82% and 96%, respectively, indicating its effectiveness to detect AC stripping damage in flexible pavements. The

analysis and developed methods developed in the study may be used for stripping damage detection and as an additional benefit of TSDD and GPR.

The study also evaluated the effects of asphalt concrete (AC) stripping damage on the performance and cost-effectiveness of chip seal and AC overlays in pavement maintenance and rehabilitation. Pavement sections were categorized according to traffic volume and pavement conditions prior to treatment (PCI-). The average deterioration rate (ADR), extension in pavement service life (ΔPSL), increase in average pavement condition (PI), and cost-effectiveness (CE) were compared for stripped and non-stripped sections. Results showed that for chip seal, moisture damage negatively affected the performance of the sections with PCI-<80 and low traffic volumes. For sections with PCI->80, similar deterioration rates were observed for stripped and non-stripped sections. For AC overlays, moisture-induced damage significantly affected the long-term pavement performance at all traffic levels. On average, moisture-induced damage decreased ΔPSL, PI, and CE of AC overlays by 4.6 years, 23%, and 0.5%, respectively.

The study employed Convolutional Neural Networks (CNN) to classify pavement sections into different International Roughness Index (IRI) categories and to predict IRI values by analyzing the captured features in three-dimensional (3D) pavement images. In addition, the effectiveness of ANN-based pattern recognition and Multinomial Logistic (MNL) regression models to categorize the roughness conditions of pavement sections was investigated. A pre-existing CNN model was trained and was validated using 850 3D pavement surface images. In addition, 1,142 test observations including IRI measurements and distress data were used to develop the ANN-based pattern recognition and MNL models. The developed CNN model classified pavement sections according to their roughness conditions with an accuracy of 93.4% and 89.6% in the training and validation stages, respectively. However, the accuracy of both the ANN and MNL models was only 58%. In addition, a CNN model was developed for the prediction of IRI values from 3D pavement images. The model yielded accurate predictions with a coefficient of determination (R2) of 0.985 and an average error of 5.9%.

Acknowledgments

The authors would also like to acknowledge the invaluable efforts of Kevin Gaspard, Christopher Fillastre, and Zhongjie “Doc” Zhang of the Louisiana Department of Transportation and Development (DOTD).

The U.S. Department of Transportation (USDOT), Federal Highway Administration (FHWA), and DOTD through LTRC financially supported this research project.

Implementation Statement

Based on the results of this project, the following implementation recommendations are provided:

- A windows-based application was developed based on validated CNN- and ANN-based models. This tool should be implemented to allow the PMS section in DOTD to classify surface cracks as top-down, bottom-up, and cement-treated reflective cracks. The developed tool should only be used for classification of a single crack pattern in a given image during the early stages of development. It should not be used for high levels of cracking.
- The developed GPR-based indicator, known as the Accumulating In-layer Peaks (AIP), should be implemented to detect AC stripping damage in asphalt pavements based on GPR measurements.
- Pavement-underlying conditions including AC stripping damage should be taken into consideration in PMS decision and treatment selection processes. Furthermore, moisture damage should be effectively corrected before the application of maintenance or rehabilitation strategies for more durable pavements and optimum use of available funds.
- An image-based CNN model was developed to predict the IRI value of the pavement section based on surface images. The developed model, which accurately predicted the IRI values, provides numerous implementation opportunities into PMS activities. The developed model may also be incorporated to predict pavement surface roughness using camera-captured pavement images during the pavement evaluation phase.

Table of Contents

List of Tables

List of Figures

Introduction

Moisture damage is a significant distress that affects the overall performance of asphalt pavements in Louisiana. The effect of moisture-induced damage on asphalt pavements is manifested in the roadway through stripping and poor durability of the mixes. Moisture-induced damage in pavements has detrimental consequences on the long-term performance, durability, and user safety.

To ensure adequate long-term pavement performance against moisture damage, methods of early detection and repair are critically needed as moisture damage only appears at the surface after detrimental damage has already progressed in the underlying pavement layers. The conventional method to detect AC stripping and moisture damage is through core extraction, which is destructive, time-consuming, and is rarely conducted. Therefore, moisture-induced damage is rarely addressed during pavement preservation activities, which may result in loss of state funds due to unsatisfactory performance after repair. Ground Penetrating Radar (GPR) and Falling Weight Deflectometer (FWD) are nondestructive evaluation (NDE) techniques, which have been applied to assess as-built conditions and to evaluate pavement damage and deterioration that develop over time. They can also be used to measure layer thicknesses and to detect moisture-induced damage in pavements *[1]*.

The Texas Department of Transportation investigated the ability of GPR to detect stripping in asphalt pavement layers *[2]*. Scullion and Rmeili successfully detected stripping in asphalt pavement layers using GPR when the deterioration was at a moderate to severe level. The study found that asphalt pavement sections with stripping had higher moisture contents, higher air voids, or both, which resulted in an anomalous increase in the dielectric constants of the stripped layers. The authors also noted that intermittent negative peaks within the surface layer in a GPR scan is typically an indication of the presence of AC stripping in asphalt pavement layers.

Hammons et al. developed an asphalt pavement survey protocol using GPR, Infra-Red (IR), Seismic, and FWD to effectively detect stripping in in-service pavements *[3]*. The study introduced a Stripping Index (SI) to quantitatively evaluate the potential locations and extent of AC stripping. SI ranges from zero to three, where zero represents good condition and three represents severe stripping. When the estimated SI values were compared with the actual core conditions, the study found that the GPR predicted stripping with 77% accuracy. The study further attempted to correlate stripping

predictions from GPR with adjusted seismic and elastic modulus values, but no significant relationship could be found.

Literature Review

Pavement Cracking and Machine Learning

Pavement distress detection and quantification is an essential step in managing road networks and planning for effective rehabilitation and maintenance strategies. The accurate and up-to-date assessment of pavement conditions is necessary to predict future deterioration rates and to plan for effective preventive maintenance and rehabilitation strategies. State departments of transportation (DOTs) in the United States are routinely using pavement condition evaluation as an integral part of Pavement Management System (PMS) to provide detailed information of pavement serviceability. Computer vision and machine learning techniques were successfully implemented on devices such as Roadware's Automatic Road Analyzer (ARAN) system, and Road Measurement Data Acquisition System (ROMDAS) to automate the road survey. In Louisiana, the pavement network is surveyed biennially using the ARAN system to collect pavement surface conditions. The ARAN vehicle is equipped with cameras, lasers, sensors, and computers to collect high definition digital images of pavement right of way and pavement surfaces identifying major pavement distresses such as rutting, cracking, faulting, and macrotexture for both the primary and secondary travel directions *[4]*.

Until recently, pavement cracking was assumed to initiate at the bottom of the asphalt concrete (AC) layer and propagate upwards to the surface, i.e., bottom-up crack. The loss in structural support due to excessive loading conditions, inadequate design and construction, and pavement distresses such as stripping are the major causes of bottom-up cracking. In the past two decades, the opposite mode of crack initiation and propagation (top-down) gained significant attention amongst researchers and pavement practitioners. The literature suggests that longitudinal top-down cracks usually appear in the wheel paths due to high surface horizontal tensile stresses from tire loads while other forms of longitudinal cracks are usually bottom-up. Until now, the field characterization of these cracks has not been well established as compared to fatigue cracking, which initiates at the bottom of the AC layer. The accurate and up-to-date detection and characterization of pavement surface cracks would help highway agencies and state DOTs set up a more accurate schedule and budget for repair of these cracks.

The recent advancements in image acquisition and processing and machine learning techniques have proven image-based technology as a promising tool to assess flexible

pavements in terms of surface cracking. Recently, Convolutional Neural Network (CNN) models have been efficiently implemented in pavement crack classification with minimal image processing. CNN is a type of Artificial Neural Network (ANN), which uses images as inputs to extract the target features as outputs for classification *[5]*. The architecture of CNN is typically structured with convolutional, pooling, and fully connected layers that can analyze the shape change complexity of the pavement cracks *[5, 6]*.

In this study, a novel method of automatic pavement crack identification is proposed based on the successful application of CNN. The proposed approach uses processed pavement images as inputs in a pre-trained CNN model known as AlexNet. Furthermore, a decision-making tool was developed using ANN as a secondary screening tool and to cross-validate the image-based classification results obtained from the CNN model. The tool used six different variables namely pavement age, base type, AC thickness, annual average daily traffic (AADT) crack orientation, and crack location to classify the crack type in the pavement surface.

Top-down Cracking in Flexible Pavements

In the past, pavement cracking was assumed to initiate at the bottom of the AC layer and propagate upwards to the surface, i.e., bottom-up crack. Yet, the opposite mode of crack initiation and propagation gained a significant attention amongst researchers and pavement practitioners in the past two decades. Literature suggest that the longitudinal top-down cracks usually appear at wheel paths due to high surface horizontal tensile stresses due to tire loads while other forms of longitudinal cracks are usually bottom-up. Figure 1 presents pavement surface and a core with top-down cracking in a flexible pavement.

Three main stages of crack propagation have been described by Svasidisant et al. (2002). The single short longitudinal cracks appear just outside the wheel path in the pavement surface in the first stage. In the second stage, sister cracks develop parallel to and within 0.3 to 1.0 meters from the original cracks and the short longitudinal cracks in the pavement surface grow longer. Over time, the cracking reaches a third stage where the parallel longitudinal cracks get connected via short transverse cracks *[7]*.

Myers et al. also reported that the surface cracks initiate just outside the wheel path and the cracks propagate to depths ranging from just under the top surface to the full depth of the asphalt concrete layer. The authors considered a wide range of AC thicknesses in their study, which ranged from 50 to 200 mm (2 to 8 in.). The time frame for the initiation of

the surface cracking was reported to be five to ten years following construction. These cracks were observed to appear as longitudinal with widths of about 3 to 4 mm (0.12 to 0.16 in.), which decreased as the crack penetrated the AC layer. The total crack depths were noted to range from about 25 mm (1 in.) from the pavement surface to the entire depth of the AC layer *[8]*, see Figure 1.

Figure 1. (a) Longitudinal crack in wheel path and (b) field core

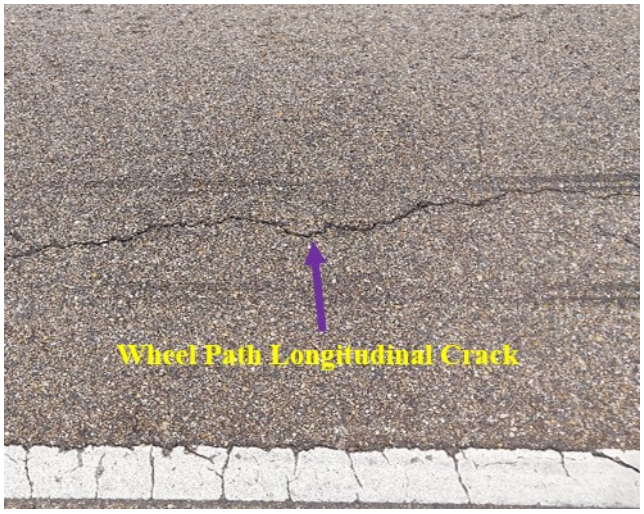

(a)

(b)

Stuart et al. reported that transverse bottom-up cracking starts in the wheel path area *[9]*. The location of these cracking was noted to be the outer edges of the wheel paths where the pavement surface has a high curvature. The authors also assessed the effect of

temperature on cracking; fatigue cracks were smaller at 28°C than at 19 and 10°C. This indicates that crack initiation and propagation vary with the pavement temperature.

The time period for the appearance of surface cracking has been reported to vary from one to ten years after construction. Svasidisant et al. (2002) observed that surface cracking penetrated through the entire depth of the AC layers in a 15-year-old pavement built with a rubblized base. However, surface cracks propagated through the full depth of the surface layers but only 50% and 20% propagated through the intermediate and base layers, respectively, in 9 to 10 years old pavements with the similar base structure *[7]*.

A study conducted for the Washington State Department of Transportation reported that thick asphalt concrete was also susceptible to top-down cracking *[10]*. The authors concluded that top-down cracking would randomly stretch, especially for asphalt layers with thicknesses surpassing 6 to 7 in. The number of years before TDC occurred varied from 1 to 5 years (Japan), 3 to 5 years (France), 5 to 10 years (Florida) and up to 10 years for the UK. Uhlmeyer et al. noted that top-down cracking occurred typically 3 to 8 years following construction in pavement sections that satisfied structural requirements and were designed for acceptable equivalent single-axle loads.

In the past 25 years, there has been an alarming increase of pavement distress related to top-down cracking in the longitudinal wheel path of asphalt pavements. Currently, TDC is a major asphalt pavement distress in Florida, Washington, Colorado, Louisiana, Michigan, and other states, as well as in many countries abroad. It has been a topic of frequent and continuing discussion between researchers worldwide, mostly focused on the roles of binder aging, segregation, thermal gradient within the surface asphalt layer in causing this distress. The cracking distress is further accelerated because of wheel loads and contact stresses. TDC identification in the field and consideration in pavement design methods are problematic compared to fatigue cracking that is assumed to initiate from the bottom of the AC layers. Maintenance and rehabilitation programming for pavement asset management at the network-level can benefit tremendously if TDC evaluation is feasible as a part of network-level condition surveys.

Louisiana Pavement Management System

In Louisiana, the pavement network is surveyed every two years to assess pavement surface conditions. The Automatic Road Analyzer (ARAN), which is equipped with computers, lasers, cameras, and sensors to capture and store high definition digital images of pavement right of way and surface conditions in both the primary and

secondary travel directions, is used. The control sections are divided into log miles in order to provide a reference location system to the distress data for all pavements. The control section log mile (CSLM) is a location reference method used for defining where treatment projects are located in the field. The distress data are collected and reported for every 1/10th of a mile *[4]*. The cracks are identified by types of distresses, which are categorized in terms of severity as low, medium, and high and labelled with green, yellow, and red colors, respectively *[11]*. The primary direction or direction 1 indicates South to North and West to East and the secondary direction or direction 2 indicates North to South and East to West (see Figure 2).

Figure 2. Primary (direction 1) and secondary (direction 2) directions for data collection *[11]*

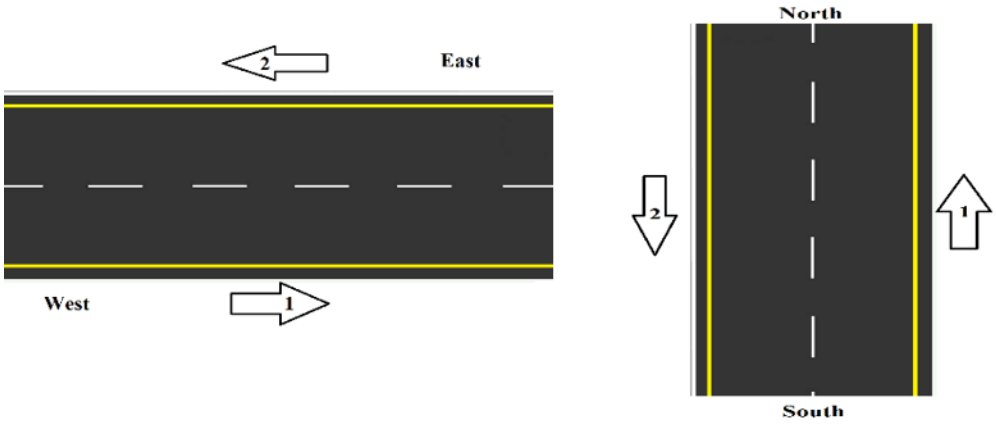

A Structure Query Language (SQL) enterprise database used by Deighton Transportation Infrastructure Management System (DTIMS) is used to store the data, which are available to the end user via iVision (Video Log view linked to pavement condition data), and the DOTD Pavement Management Intranet Web Portal *[12]*. A web application with a Geographical Information System (GIS) interface known as “intranet version of DOTD’s PMS” shown in Figure 3, allows the end user to access the desirable data collected from the survey.

Figure 3. DOTD pavement management page

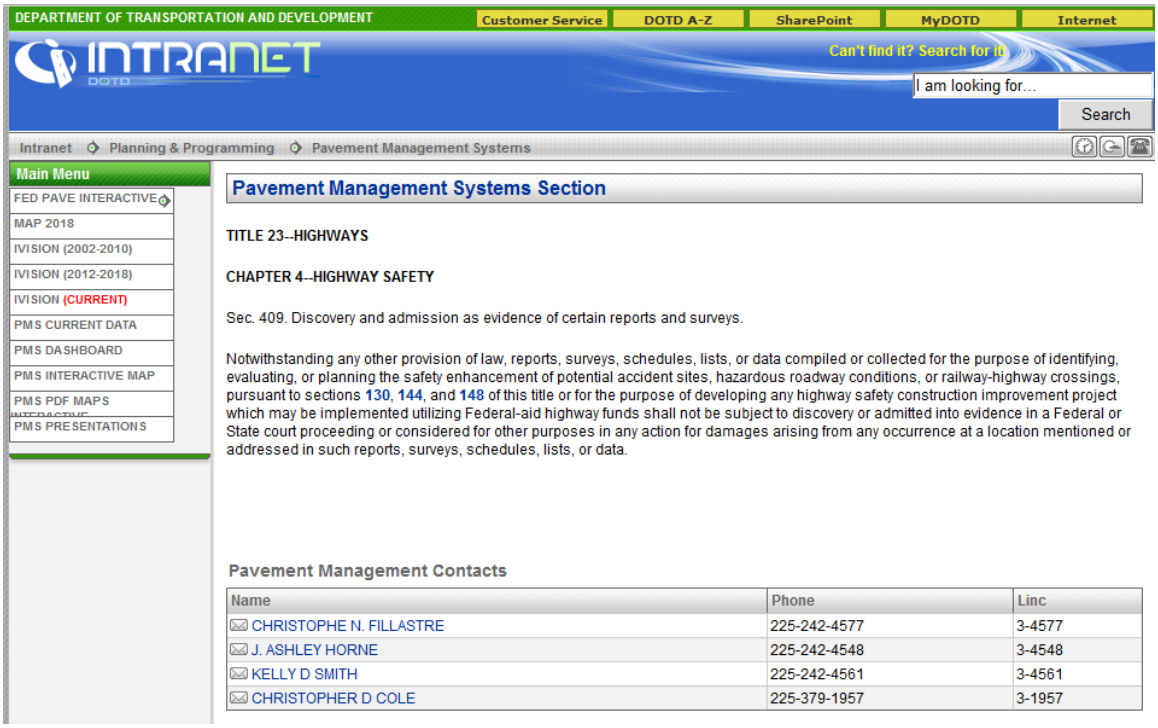

Image-Based Crack Identification Method

Early efforts in developing crack extraction algorithms were focused in statistical intensity thresholding approaches. Till date, this technique has been used by many researchers due to its simplicity and efficacy. Maser (1987) proposed a threshold-based segmentation for image analysis by enhancing the image using histogram equalization *[13]*. Li et al. employed a combination of image histogram and projection histogram to separate non-distress objects such as road markings, oils, and tire marks from major distresses on flexible pavements *[14]*. Koutsopoulos and Downey reported that the regression-based histogram method provided the best results compared to three other intensity thresholding methods, which included the Otsu's method *[15]*, relaxation method, and the Kittler's method *[16]*. The authors developed image enhancement, segmentation, and distress classification algorithms to address different distress types in flexible pavements. A different approach was suggested for image binarization, which assigned a value of 0 to 3 to each pixel based on its probability of belonging to the object *[17]*.

Georgopoulos et al. developed an algorithm and used a software "APDIS" to automatically identify the type, extent, and severity of pavement cracks *[18]*. Xu and

Huang developed an algorithm based on “grid cell” analysis, which divided the pavement into small cells where a cell is classified as a crack or non-crack based on its statistical characteristics *[19]*. Wu et al. developed a crack recognition and segmentation algorithm known as MorphLink-C; the algorithm consisted of two processes; (a) using morphological dilation transform to group crack fragments and (b) using thinning transform to connect the fragments *[20]*.

Wavelet transforms, edge detection, and texture analysis are three widely used techniques in pavement crack detection *[21]*. Zhou et al. used wavelet transform to separate road distresses into high-amplitude wavelet coefficients and pavement noise to low-amplitude wavelet coefficients before applying statistical functions to detect and segment cracks *[22]*. Ying and Salari proposed a beamlet transform based technique that can be used to extract linear features such as cracks in pavement after application of an image enhancement algorithm *[23]*. A method based on 2D wavelet continuous wavelet transform was applied to detect pavement cracks by Subirats et al. *[24]*. Multiscale complex coefficient maps were used before the application of an algorithm to search wavelet coefficient maximal values and their propagation through the scales for crack detection. Yet, the wavelet transform techniques have limitations in detecting high curvature or low continuity cracks *[21]*.

In edge detection techniques, algorithms are applied to search and detect edges (defined as sharp intensity transitions) without any inputs or human interference. Abdel-Qader et al. used bidimensional empirical mode decomposition (BEMD) smoothing method to remove noise and applied sobel edge detection technique to detect surface cracks *[25]*. The sobel edge detection technique was observed to produce better results for images with less irregularities and noise *[26]*. Maode et al. employed morphological operation tools to detect, extract and fill the crack edges. The procedure consisted of the application of morphological gradient operator with morphological closing operator after the use of median filter to smooth and enhance pavement image *[27]*. The texture analysis techniques employ crack extraction algorithms to separate cracks from highly textured pavements.

Song et al. presented an algorithm based on Wigner distribution to segment cracks from complex textured background. This model was adjudged highly effective and better than Fourier-based crack detector in terms of locality and discriminatory power *[28]*. In a study by Hu and Zhao, a gray-scale and rotation invariant operator known as the local binary pattern (LBP) was used for texture classification and crack detection *[29]*. Despite the advancements in various image processing techniques, researchers still encounter

various challenges in image processing due to texture inhomogeneity of pavement aggregate, random non-crack background noises, spots and stains, oils, road markings and so forth. These challenges demand further advancement in image preprocessing and thresholding techniques to accurately assess surface pavement conditions.

Latest Advancements in Image-Based Crack Detection Techniques. In recent years, significant improvements were achieved in crack recognition, classification, and characterization approaches that use computer vision techniques. These techniques are considered as promising approaches to assess pavement surface conditions in terms of cracking by analyzing captured pavement images. Koch et al. noted in their review the increasing use of high-level computer vision techniques such as neural models and support vector machines (SVM) with image processing in segmentation, classification, and feature extraction of pavement cracks *[30]*. Moussa and Hussain used SVM to classify surface cracks as transverse, longitudinal, block, and alligator cracking after the images were segmented using graph cut segmentation procedure *[31]*. Nguyen et al. combined Conditional Texture Anisotropy (CTA) method of crack segmentation with multi-layer perceptron neural network to classify the detected defects as cracks and joints *[32]*.

Mokhtari et al. compared four computer-vision based crack detection systems: artificial neural network (ANN), k-nearest neighbor, decision tress, and adaptive neuro-fuzzy inference system (ANFIS). ANN and ANFIS methods were observed to be more accurate in terms of prediction, computation time, and stability of the results and classifiers' performance *[33]*.

Deep Learning (DL) based computer vision approaches have gained significant interests amongst pavement researchers in recent years, particularly for distress classification. The four main DL architectures are Restricted Boltzman Machines (RBMs), Deep Belief Networks (DBNs), Autoencoder (AE), and Deep Convolutional Neural Networks (DCCNs or Deep ConvNets) *[34]*. The DCCNs are typically composed of convolutional, pooling and fully-connected layers. A filter bank, which is a set of weights, connects units in the feature maps of convolutional layers to local patches in the feature maps of the input data. The pooling layer units receive the maximum of a local patch of units in one feature map and also reduce the resolution of feature maps to select the spatial invariance. The fully connected layers are similar to traditional multi-layer perceptron in which all units in the feature maps are concatenated together in the form of a vector *[6]*. Figure 4 illustrates the feature map generation with the convolutional operator *[35]*. The convolutional layer consists of convolution filters and generates the same number of

feature maps as that of filters. The pooling layers, however, contain a stationary filter such that the convolution areas do not overlap. The pooling layer reduces the image size to improve computational efficiency and avoid data overfitting. An illustration of pooling operation is presented in Figure 4 *[35]*.

Figure 4. (a) Convolutional operator, (b) max pooling operator *[35]*

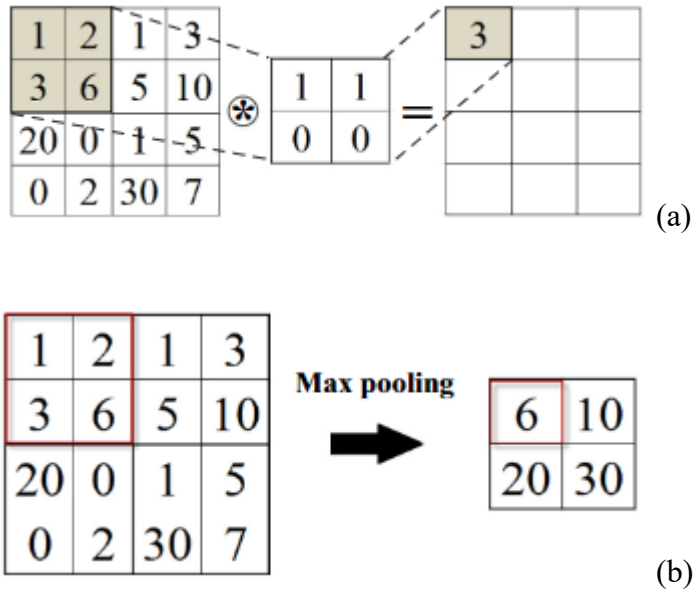

Zhang et al. developed an automatic crack detection DCNN based on manually-annotated image patches as inputs *[36]*. The dataset consisted of 500 pavement images of size 3264x2448 collected using a smart phone. The collected pavement images were sampled to generate one million three-channel (RGB) 99*99 pixel image patches; 640,000 samples were used for training, 160,000 samples were used for validation, and 200,000 samples were used for testing. The developed solution classified the crack and non-crack pixels referred to as positive and negative patches respectively based on a ConvNet trained in square image patches. The training process was amplified using the rectified linear units (ReLU) activation function. Figure 5 illustrates the architecture of the proposed DCNN *[36]*.

Figure 5. Architecture of proposed DCNN *[36]*

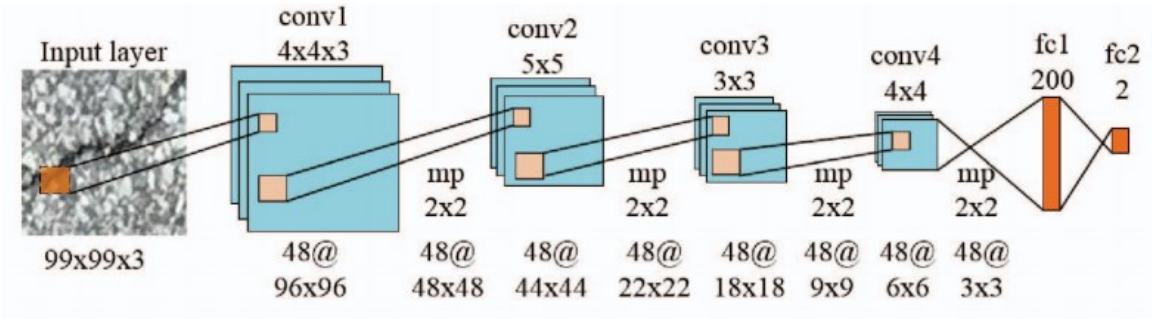

Elisenbach et al. developed a convolutional neural network for road crack detection and named it as RCD net, which used the same four-block ConvNet developed by Zhang et al. *[37]*. The German Asphalt Pavement Distress (GAPs) dataset was introduced as an attempt to create a standard benchmarking pavement distress dataset for DL applications *[38]*. A DL approach, known as ASINVOS, which consisted of eight convolutional layers, three max-pooling layers, and three fully-connected layers, was implemented to study the regularization effects on the generalization ability of DCNN. The proposed approach was observed to outperform the traditional distress detection approaches with higher generalization ability *[37]*. Maeda et al. used object detection CNN for automatic road distress detection. The images for the proposed approach were acquired using a smartphone installed in a moving vehicle. The authors also developed a mobile application that captures 600x600 pixels road images by a smartphone mounted on a car *[39]*.

Fan et al. proposed an automated crack detection procedure based on structural prediction using CNN. The CNN was modeled as a multi-label classification problem, which consisted of four convolutional layers, two max-pooling layers, and three fully-connected layers. The overall pavement condition was presented by probability map obtained by summing the center patch structure predictions of the trained CNN applied on all pixels. The proposed method was observed to be more accurate as compared with other existing methods of crack detection *[40]*. The CNN used by the authors is illustrated in Figure 6. The convolutional layers were with kernel of 3 x 3, stride 1 and zero padding and max pooling was performed with a stride 2 over a 2 x 2 window.

Figure 6. CNN architecture *[40]*

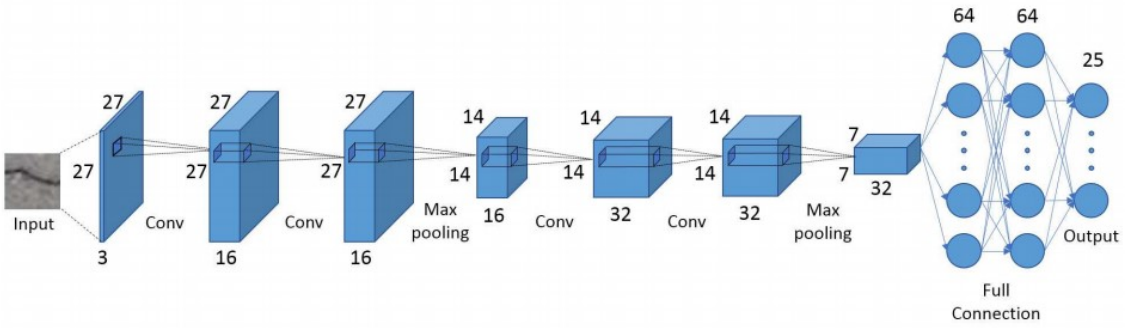

Wang and Hu employed principal component analysis (PCA) and CNN to classify pavement cracks as transverse, longitudinal, and alligator by first detecting cracks by segmenting image into grids after applying PCA to analyze the skeleton of the crack *[41]*. The authors used two different scales of grid (32x32, 64x64) for image segmentation. The CNN architecture consisted of two convolutional layers, two max-pooling layers, and one fully-connected layer. The proposed approach was observed to achieve higher classification accuracy; 97.2%, 97.6%, and 90.1%, respectively for longitudinal, transverse, and alligator cracks.

Nhat-Duc et al. conducted a study to compare pavement cracking detection using edge detection technique and convolutional neural network (CNN). The edge detection technique employed the Canny and Sobel algorithms for image processing and were dependent upon the selection of proper threshold parameters for better accuracy. The models were trained and validated with 400 images of crack and non-crack labels. Figure 7 presents the edge detection crack recognition model and CNN model structure, which was trained using the MATLAB image processing toolbox. The convolutional operations were employed with the 30 number of filters (K). The size of the first, second, third, and fourth convolutional layers were 12 x 12, 8 x 8, 5 x 5, and 3 x 3 respectively while the size was 6 x 6, 4 x 4, 4 x 4, and 3 x 3 for the four pooling layers. The accuracy of the CNN, Sobel algorithm, and Canny algorithm were reported to be 92.1%, 79.9%, and 76.7%, respectively *[35]*.

Figure 7. (a) Edge detection-based crack recognition model and (b) CNN model structure for crack detection *[35]*

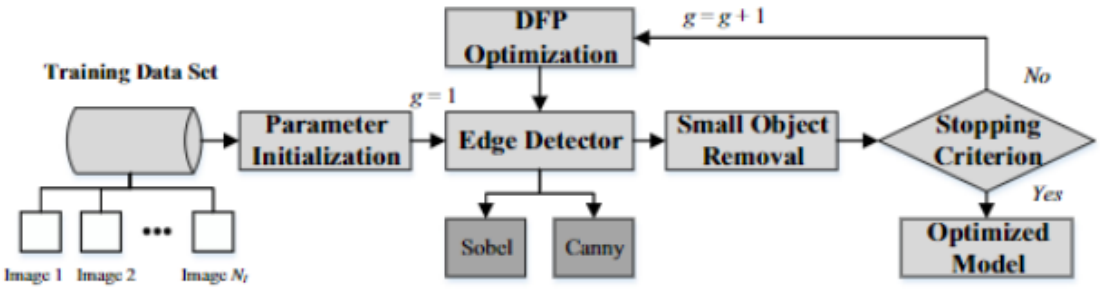

(a)

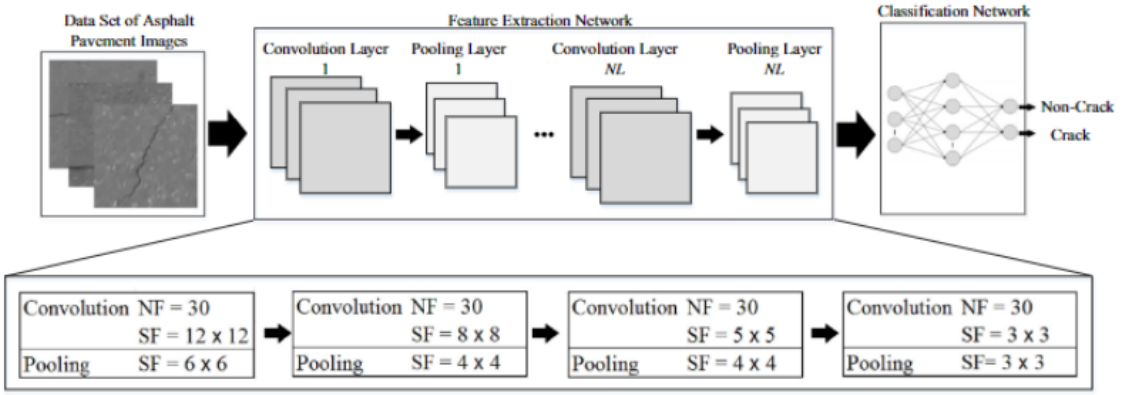

(b)

The testing and validation accuracy of DCCNs is usually dependent upon the training image dataset. Researchers have recommended to use at least 10,000 images in each class for higher classification accuracy using DL based classification *[42]*. In some cases where the acquisition of large dataset is difficult, the use of "off-the-shelf" DCNN features of well-established DCNN such as AlexNet, resnet, VGG-16, and GoogLeNet have proven to be the best approach in classification; these networks are pre-trained using large-scale annotated natural image datasets. This approach, also known as transfer learning, enables the learning ability of pre-trained models trained on large datasets to be deployed on new domains consisting of smaller-size datasets *[34]*. Li and Zhao successfully implemented AlexNet to detect pavement cracks; the authors modified the pre-trained AlexNet with five convolutional layers, three max-pooling layers, and three fully connected layers. The dropout and local response normalization techniques were implemented, where normalization was followed by the first two pooling layers, and

dropout was located after the first two fully connected layers *[43]*. Figure 8 presents the CNN overall architecture.

Figure 8. Illustration of a CNN's overall architecture *[43]*

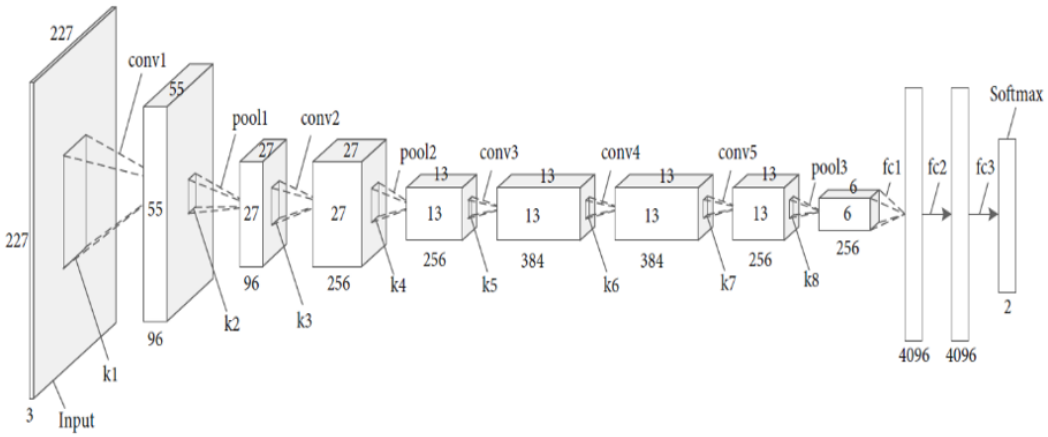

conv# = Convolution; pool# = Pooling; fc# = Full Connection; k# = Kernel of each Operation

Artificial Neural Network

Artificial Neutral Networks (ANNs) are parallel computing schemes that functions similar to the mechanism of the human biological nature of neurons and can model complex problems. ANNs are widely recognized as effective computational modelling tools that can be used to solve engineering problems because of their unique features such as non-linearity, noise tolerance in the input data, adaptability with complicated data patterns, and data generalization capability. These properties of ANN allow complex data fitting and facilitates the model implementation to unlearned data *[12]*. The generic, accurate, and complex mathematical models provide high capability to simulate numerical model components and are developed to solve complex engineering problems *[44]*. The learning ability of genetic flexible training algorithm in ANN allows it to make decisions based on given inputs *[45]*. The ANN provide robust models that can be continuously updated with new data and are more accurate with large database *[46]*.

Feed Forward ANN. A feed forward ANN is the most frequently used ANN structure for classification problems and regression analysis. It consists of (a) an input layer "i" that is typically used to train the model with multiple independent variables, (b) one or more hidden or processing layers "j" that adjust and update the weights to process the data, and (c) a target layer "k" *[45]*. The processing units called "neurons" are assigned a "bias"

and are connected to each other with each connection that is assigned a "weight." An example of ANN is presented in Figure 9 *[12]*.

Figure 9. Example of feed-forward neural network structures *[12]*

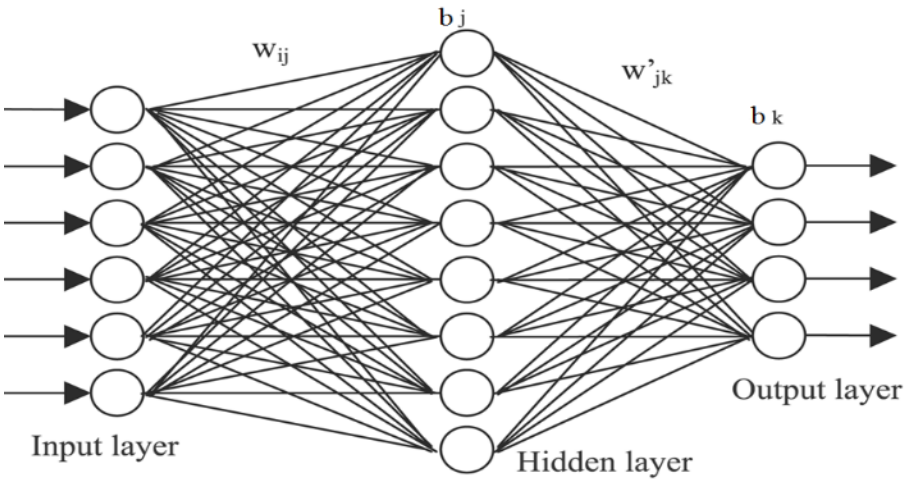

Back Propagation Algorithm. A most common algorithm for error optimization in the learning and training phases of ANN is called back-propagation, which calculates the weights and biases to match the desired output *[12]*. Figure 10 illustrates the concept of back-propagation algorithm. Equation (1) presents the objective function, which calculates the error from the network output. The target of the ANN is to minimize this objective function as in a regular optimization problem.

$$E = \frac{1}{2}(t - y)^2 = \frac{1}{2}[t - f(w, b, x)]^2 \quad (1)$$

Where, E= error function, y = network output, t = target value, w= weights, b= biases, and x= independent variables.

Figure 10. Backpropagation algorithm *[12]*

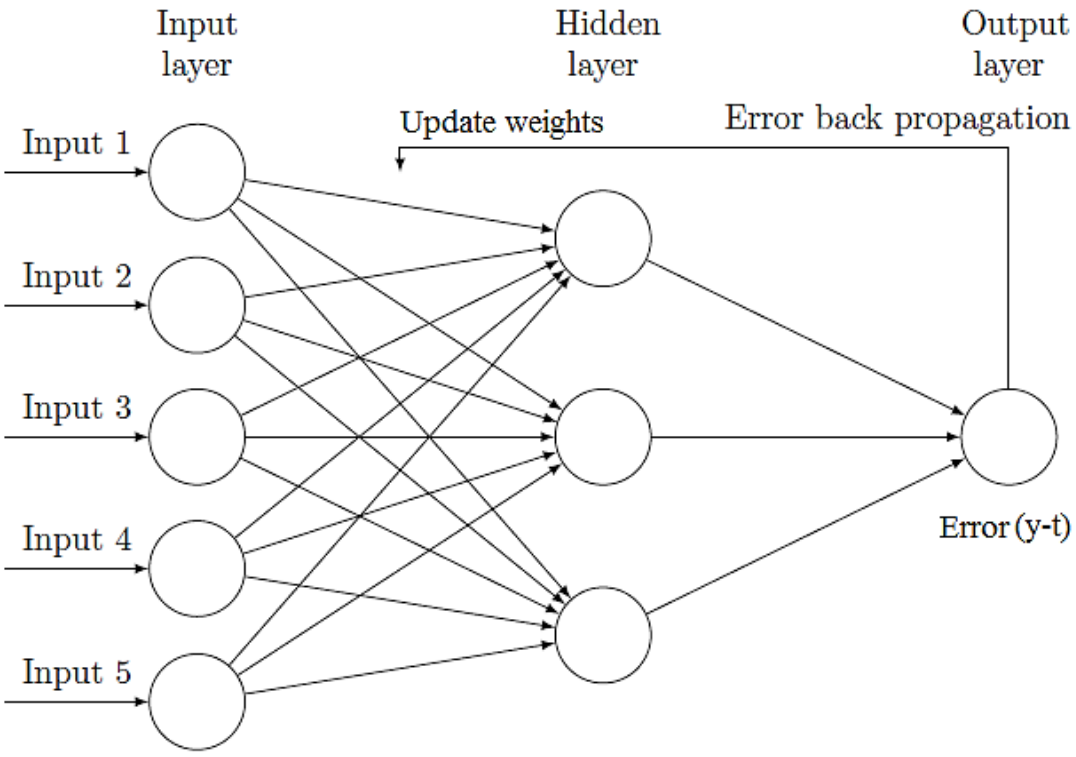

ANN Transfer Functions. The output of the network training is provided by different activation functions, which are assigned to the weighted input of the neurons. The transfer functions or the activation functions are the differentiable non-linear functions, which allow the neural network to acquire non-linearity. The logistic sigmoidal function (logsig), tan sigmoidal function (tansig), and "hardlim" are three major transfer functions used in ANN as shown in Figure 11. The logsig transfer function produces the output between "0" and "+1," tansig produces the output between "-1" and "+1." The hardlim is the most commonly used activation function and produces an output either "0" or "+1," which allows the ANN to perform the classification *[12]*.

Figure 11. ANN transfer functions, (a) logsig, (b) tansig, (c) hardlim *[12]*

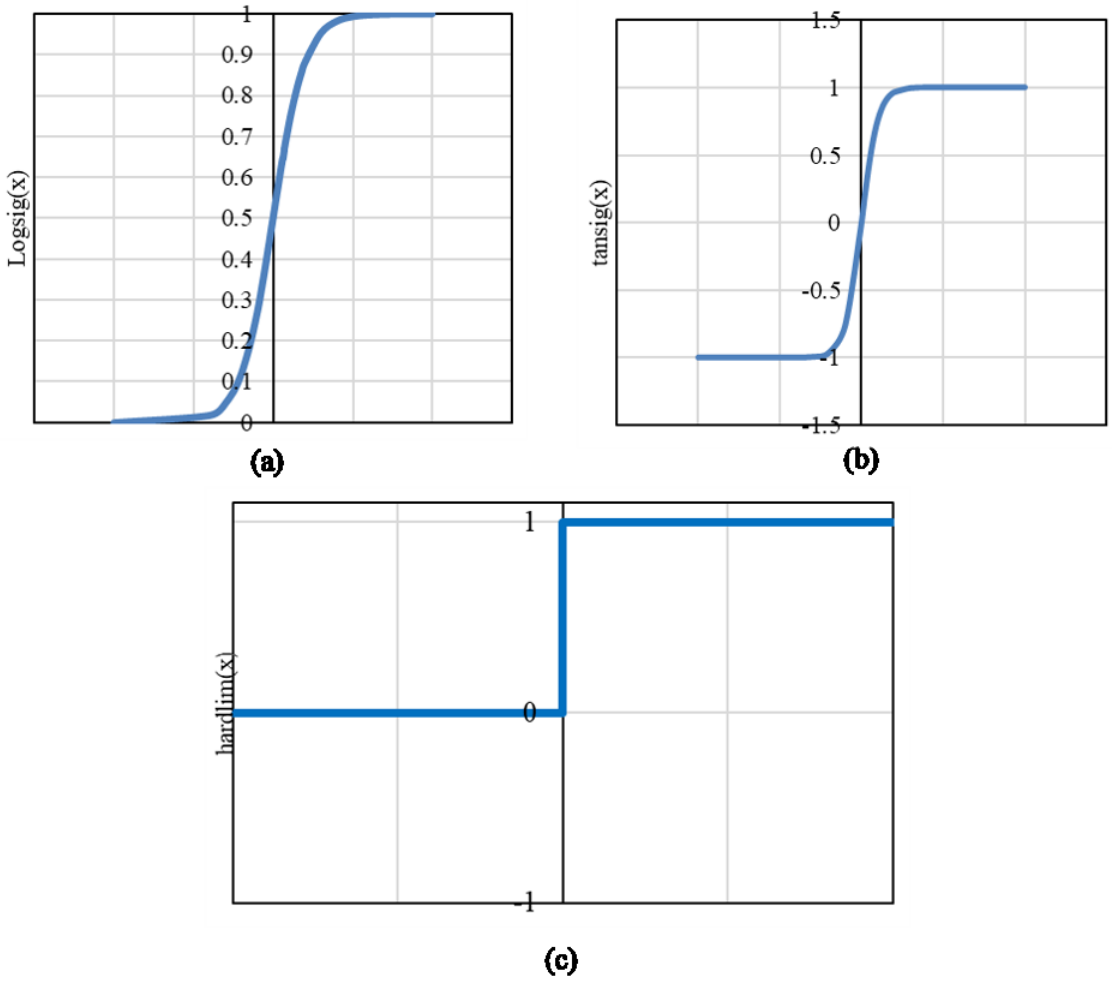

ANN Forward Calculations. The ANN network can be used as a forward calculation tool once the desired accuracies are achieved during the training, testing, and validation phases. The network assigns proper weights and biases to the connections and neurons, which can be used to perform forward calculation on new data sets. Leverington (2012) presented the general equation of the forward algorithm *[47]*. This equation is based on ANN with one output variable, one hidden layer variable, and a tan-sigmoid transfer function (see Equation 2).

$$y = (b_K + \sum_1^{n_j} \text{tansig}(b_j + \sum_1^{n_i} a_i W_{ij})\, W_{jk}) \quad (2)$$

Where, k= the model output at layer k, n_j = number of neurons in the hidden layer, n_i = number of neurons in the input layer, and a_i = the input variables.

The input vector is multiplied by the weight matrix (W_{ij}) and the hidden bias vector (bj) is added, which computes the inputs to the hidden layer (j) at the first step. Then, the outputs of the hidden layer (j) are calculated by using the activation function, which is then multiplied by the weight vector (W_{jk}) and is added to the bias value (bk) to calculate the output vector *[47]*.

Asphalt Concrete Stripping Failure Mechanism

Moisture damage can be defined as the reduction of strength and durability of the pavement structure due to the effects of moisture *[48]*. Moisture damage in pavements can occur in two primary forms, softening and AC stripping *[49]*. Softening is the loss in strength and stiffness of the asphalt mixture as a result of reduction in cohesion. Stripping, on the other hand is related to the loss of adhesion, which causes separation of the binder and the aggregate in the pavement surface layer. NCHRP Synthesis 175 characterized stripping as a three-stage process of reduction in contact angle between the asphalt and aggregate surface *[50]*. The process is illustrated in Figure 12.

Figure 12. Schematic of the stripping process *[50]*

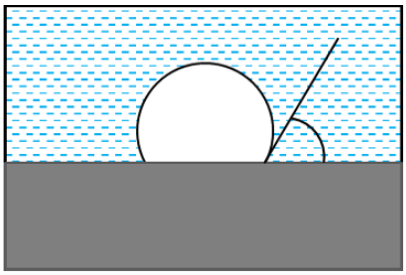

The moment at which the aggregate, with the drop of binder is immersed in water. The contact angle is less than 90°.

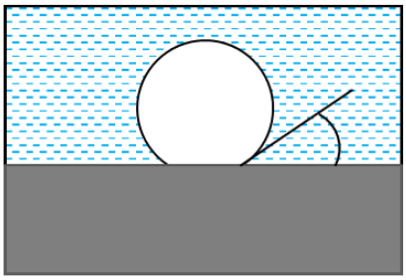

The water begins to remove the binder drop from the aggregate surface and the contact angle decreases.

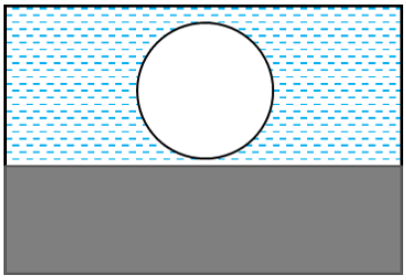

A state is reached where the contact angle is less than 0° and the binder losses contact with the aggregate surface.

Moisture damage permeates and weakens the mastic and makes the pavement structure more susceptible to damage under traffic. Repeated loading in a stripped pavement may cause severe cracks, deformation and failure of the pavement. Wearing courses placed over stripped flexible pavements are likely to exhibit potholes and raveling due to adhesion failure *[50]*. A wide range of physical processes have been associated as the cause of stripping including detachment, displacement, spontaneous emulsification, pore pressure etc. These processes are summarized in Table 1.

Table 1. Causes of stripping *[49]*

Mechanism	Description
Detachment	It is the separation of an asphalt film from an aggregate surface by a thin film of water with no breaks in the film.
Displacement	It involves the displacement of asphalt at the aggregate surface through a break in the asphalt film. Incomplete aggregate coating, sharp aggregate corners or edges, or pinholes originating in the asphalt film may lead towards the breaking of the film.
Spontaneous Emulsification	Spontaneous emulsification is an inverted emulsion of water droplets in asphalt cement. The presence of emulsifiers such as clays and asphalt additives further aggravate the formation of such emulsions.
Pore Pressure	Pore pressure due to entrapped water may lead to distress and it will in turn, disrupt the asphalt film from the aggregate surface under repeated traffic load or may cause the formation of microcracks in the asphalt mastic.
Hydraulic Scour	Hydraulic scour occurs at the pavement surface where stripping results from the action of tires on a saturated surface. Water suction into pavement by tire action, and subsequent osmosis and pullback processes cause this form of damage.
pH Instability	Asphalt-aggregate adhesion is strongly influenced by the pH of the contact water. The pH of the water affects contact angle and the wetting characteristics of the aggregate-asphalt interface region.
Environmental Effects	Environment affects water sensitivity, which works as an underlying mechanism leading towards the stripping of asphalt pavements. The environmental concerns identified are water from precipitation of groundwater sources, temperature fluctuations, and aging of the asphalt.

Asphalt Concrete Stripping Detection Methods

The traditional method of AC stripping detection (i.e., cores extraction followed by visual inspection) is time and labor-intensive. Moreover, cores only represent discrete locations and may not accurately represent the continuous conditions throughout the pavement section. Recent developments in non-destructive evaluation of in-service pavement conditions have increased the prospect of detecting stripping damage during the early stage of development and to allow for cost-effective maintenance activities to address the detected damage *[2]*.

Recent studies have shown that non-destructive devices such as Ground Penetrating Radar (GPR), Portable Seismic Property Analyzer (PSPA), Ultrasonic Tomography

(MIRA), and Infrared Thermography (IRT) may be able to detect moisture damage in pavements *[2]*. Yet, studies have highlighted the limitations of these devices and recommended further research and development *[51]*. The potential of these devices is discussed in the following sections with an emphasis on the current state of NDE practice in AC stripping detection.

Portable Seismic Property Analyzer. Seismic methods such as PSPA have shown their potential in detecting pavement distresses including moisture damage in asphalt pavements *[52]*. These methods are based on the transmission and detection of stress waves in a layered medium. Fourier transformed time records of the measured dispersion of the shear waves in the pavement allow prediction of the shear modulus of the profile and spectral analysis is performed to obtain phase information *[3]*. It is the combination of two NDE methods: Ultrasonic Surface Waves (USW) and Impact Echo (IE). PSPA is typically used in estimating the modulus of the surface layer and assessing the variation of the modulus with depth.

PSPA is a portable device that consists of a source package and two transducers, which enable the system to perform seismic tests in the field. The device can be operated using a computer that is connected to a hand-held transducer unit by a cable that transfers operational commands and measured the signal between the device and the computer as shown in Figure 13.

Most of the data acquisition tasks are performed automatically by the computer; however, a technician has to initiate the testing sequence in the computer. Four to six high frequency sources are activated. The dynamic range of the system is calibrated using the pre-recoding impacts of the sources by adjusting the gains of the amplifiers. The final three impacts from the three transducers are recorded as outputs, which are then averaged.

Figure 13. Portable seismic property analyzer *[52]*

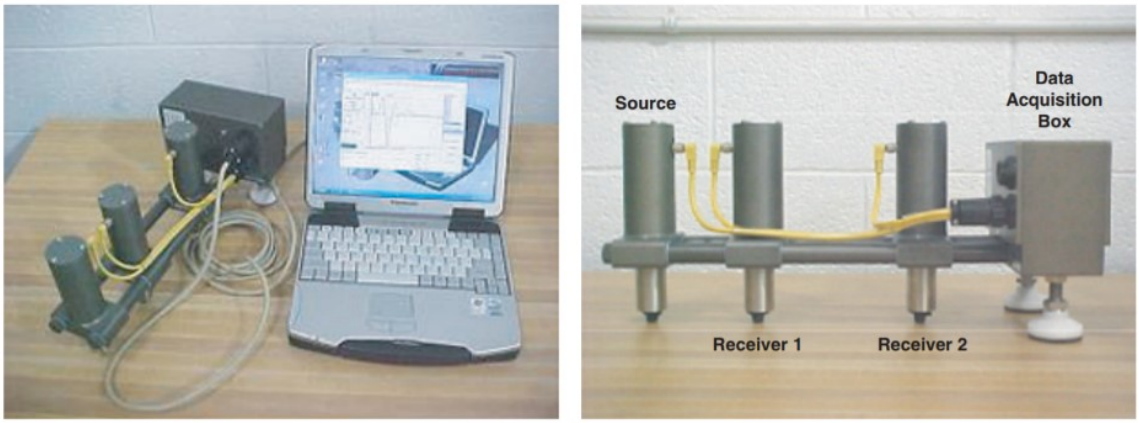

The analysis of PSPA measurements is based on calculating the stress propagation velocity in the material, which is related to its linear elastic modulus. The USW method estimates the modulus of the material without back calculation using the following equation:

$$E_{field} = 2\rho[(1.13 - 0.16\nu)V_R]^2(1 + \nu) \quad (3)$$

Where, $E_{field} =$ The modulus of the upper layer, $V_R =$ The velocity of surface waves, $\rho =$ mass density, and $\nu =$ Poisson's ratio.

The Impact Echo method estimates the thickness of the surface layer and can also be used to detect cracks, locate voids, defects, and delamination within a concrete structure. Impact echo detects the frequency of the standing wave reflecting from the bottom and the surface of the pavement layer and the thickness (h) of the layer using the following equation:

$$h = \frac{V_p}{2f} \quad (4)$$

Where, $f =$ resonant frequency calculated by converting the time record into the frequency domain. V_p is the compression wave velocity, which is determined from the following equation if the surface wave velocity (V_R) is known:

$$V_p = \frac{V_R}{0.13 - 0.16\nu}\sqrt{\frac{1-\nu}{0.5-\nu}} \quad (5)$$

The moduli obtained using the seismic methods are usually of low magnitude deformation and for high strain rates. On the other hand, repeated traffic loads cause high magnitude deformation. This difference is addressed using the master curve concept. Ferry proposed the following sigmoidal function that can be used to construct a master curve *[53]*:

$$\log(E^*) = \delta + \frac{\alpha}{1+e^{\beta+\gamma \log t_r}} \quad (6)$$

Where, E^* = dynamic modulus, t_r = loading period, δ = minimum value of dynamic modulus, α = span of E* values, and $\beta \; and \; \gamma$ = sigmoid function shape parameter.

Application of PSPA in Moisture Damage Detection. Celaya and Nazarian (2007) used PSPA with ground truth data to evaluate the capabilities of both USW and IE in detecting moisture damage in pavements *[52]*. USW was found to be superior to the IE method in identifying the severity and extent of the damage in terms of asphalt layer stiffness. For detection of stripping at shallow depths, the standard receiver spacing of 6 in. worked well, but for stripping in depths greater than first 10 in., longer receiver spacing was recommended. The study observed that the peak frequency of IE spectrum was not suitable for locating stripping in pavement layers as the peak frequencies for stripped and non-stripped layers were found to be similar. However, for the damaged areas, the amplitude was distributed over a wider range of frequencies, as shown in Figure 14.

Figure 14. IE amplitude spectra from sound and deteriorated locations

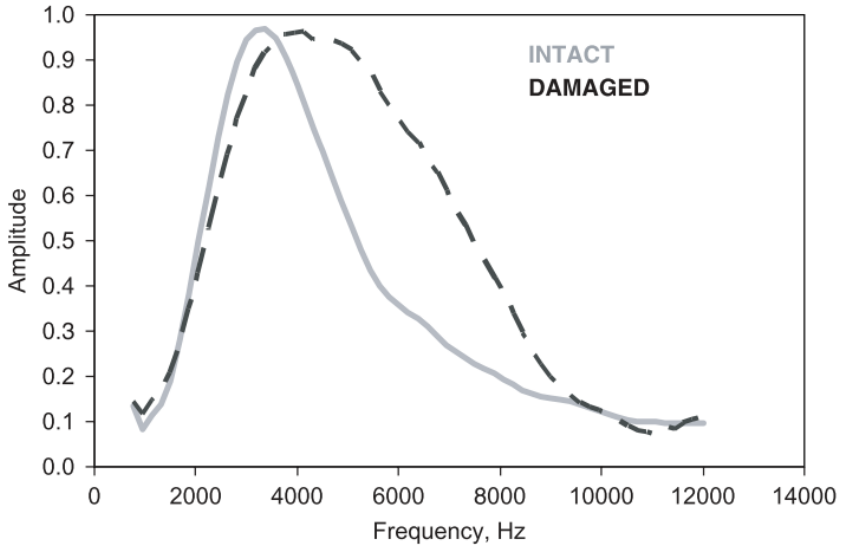

MIRA Tomography. The MIRA tomographer, as shown in Figure 15, is a state-of-the-art instrument, which is capable of producing three dimensional (3-D) representations (tomogram) of flaws that are present inside a concrete structure *[54, 55]*. It does not require surface preparation as the subsurface condition of concrete elements can be investigated using an array of dry point contact (DPC) "touch and go" transducers. The antenna is composed of an array of DPC transducers and it sends low-frequency shear waves into the structure. Unlike traditional ultrasonic techniques, which generally produce one pair of waves per measurement, MIRA allows for 45 transmitting and receiving pair measurements in each approximately 1-second scan, which can achieve high productivity *[56]*. The received data are then used to create a 2-D image of the reflecting interfaces inside the concrete element. A proprietary software is used to assemble the stacks of 2-D images into a 3-D model of the test specimen. The test results can be interpreted by manipulating the generated 3-D image *[55]*.

Figure 15. MIRA tomographer

MIRA has been found to be effective in the following applications *[54, 55, 56]*:

- Concrete thickness estimation up to 3 ft. deep with high accuracy;
- Accurate estimation of reinforcement depth;
- Detection of cracking in the PCC layer or de-bonding between PCC layers;

- Detection of concrete deterioration, dowel position, and spalling.

Ground Penetrating Radar. Ground Penetrating Radar (GPR) is a highly versatile NDE method that transmits short pulses of electromagnetic waves into the pavement and the reflections from the material boundaries and subsurface anomalies are identified by the receiving antenna mounted on a survey vehicle. As the vehicle can operate at regular traffic speed, it provides GPR an extra edge over other NDE techniques of pavement condition evaluation *[57, 58]*. GPR was found to be effective in a wide range of highway applications including but not limited to the estimation of pavement layer thickness, detection of subsurface moisture, density variations, voids, and underground utility locations *[[1]]*. GPR technique has widely been used in Finland, Sweden, Germany and Estonia for HMA construction quality control purposes *[[51], 59, 60]*. Although several DOTs use GPR for measuring layer thicknesses, identifying section breaks, and estimating trapped moisture, GPR is not commonly included in state specifications in HMA construction quality control activities *[[51]]*.

GPR systems are generally available in two main types. In a ground-coupled GPR system, the antennas are in contact with the ground and when the antennas are not in contact with the ground, it is referred to as an air-coupled GPR system. Ground-coupled GPR systems are capable of producing clearer data as it can get more energy in to the ground and more energy out of it. However, ground-coupled GPR system is limited by the interference between the direct-coupling and ground reflection, which affects the usefulness of the data at shallow depth. Air-coupled GPR provides a faster mean of data collection without damaging the antennas since these are usually mounted on a vehicle. In addition, the direct-coupling between the antennas is separated from the ground reflection, which provides better quality of the data at shallow depth. The SIR-30 is an advanced high-performance multi-channel radar control unit that offers advanced filters and display capabilities for real-time processing, including migration, surface positioning, signal floor tracking, and adaptive background removal, see Figure 16 *[61]*.

Figure 16. Layout of a GPR system

The equipment typically consists of a control unit, monitor, and two dipole bowtie (ground coupled) antennae operating at center frequencies of 900 MHz and 1.6 GHz. The setup can perform up to 16 scans per ft. at 10 mph, which results in a scan about every 1 in. The data are collected at the posted speed limit with a maximum of 55 mph, although the speed varies based on traffic and stops. A typical GPR acquisition setup is presented in Table 2.

Table 2. Typical GPR acquisition setup

Antennas		**GSSI ground coupled**	
Channel	**-**	1	2
Frequency	**[MHz]**	1600	900
Time window	**[ns]**	15	30
Samples/scan	**-**	256	256
Trace interval	**[scan/m]**	4	4
IIR (vertical high/low pass filter)	**[MHz]**	375/3000	225/1800

A survey encoder is used to connect the GPR device to a calibrated survey wheel to measure the distance. A Global Positioning System (GPS) device is also used to track the locations of the survey lines. The GPS data are typically picked at 0.01-mile intervals along the road segment. The moving mode employed allows a radar wave to be

transmitted, received, and recorded each time the antenna is moved a fixed distance across the pavement surface. The recorded signals are displayed as traces side-by-side to form a GPR time-distance record, or radargram, which shows how the reflections vary in the subsurface.

GPR transmits short pulses of electromagnetic waves into the ground. One-dimensional electromagnetic wave propagation theory is used to analyze the reflected signals of these pulses. Based on the material dielectric properties, surface electrical conductivity, and subsurface layers, the pulses are reflected back to the receiving antenna with different amplitudes and travel times.

The dielectric mismatch across the material interfaces results in transmission and reflection of energy at the interfaces. The reflected signals are transmitted to the receiving antenna and displayed as shown in Figure 17. The surface, base and subbase reflections are indicated by $A_0, A_1\ and\ A_2$ respectively. The two-way travel times between the surface, base, and subbase peaks are represented by $\Delta t_1\ and\ \Delta t_2$.

Figure 17. GPR working principle

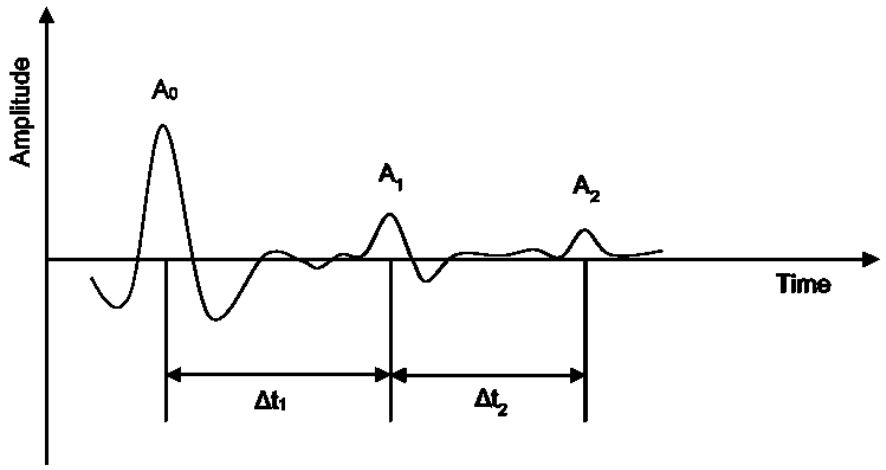

The velocity of the electromagnetic wave propagation through the nth layer is given by:

$$v_n = \frac{c}{\sqrt{\varepsilon_n}} \quad (7)$$

Where, v_n= GPR pulse velocity, c= The speed of light in vacuum, and ε_n = Dielectric constant of nth layer.

The thickness of a pavement layer can be estimated by:

$$d_n = \frac{v\Delta t_n}{2} = \frac{c\Delta t_n}{2\sqrt{\varepsilon_n}} \quad (8)$$

Where, d_n= The thickness of the nth layer, and Δt_n= Two-way travel time through n^{th} layer.

Equation (8) can be re-written as follows:

$$\varepsilon_n = \left(\frac{c \times \Delta t_n}{2d_n}\right)^2 \quad (9)$$

Using layer thicknesses obtained from extracted core samples, Equation (9) can be utilized to estimate the dielectric constants of the pavement layers. Based on previous studies, lower dielectric constants of the asphalt layer were associated with the presence of stripping after the water had drained out *[[2], [3]]*.

A wide range of software packages including RADAN, RGPR, Reflexw, GPRSIM, and GPRMax are available and are used to analyze GPR data. RADAN is the most common software that is used to process and analyze the radargrams from the GPR data files *[62]*. The software color codes each of the traces for a better visual interpretation of the scans. The raw data are subjected to surface position adjustment, time zero correction, infinite impulse response (IIR) and finite impulse response (FIR) filtering before reaching the interpretation stage. A band-pass filter is used to remove high and low-frequency noises from the scans.

The Interactive Interpolation module of the software can be used to semi-automatically locate and analyze features in the GPR scans by defining “picks.” RADAN defines a “pick” as a peak amplitude identified in a scan that corresponds to a layer. An illustration of interactive module is presented in Figure 18 where the top of HMA layer is identified with yellow picks while the HMA-based interface is identified with green picks. MS Excel can be used to convert the extracted data to dielectric values in conjunction with the data collected from the roadway cores.

Figure 18. Interactive interpolation of GPR data files using RADAN

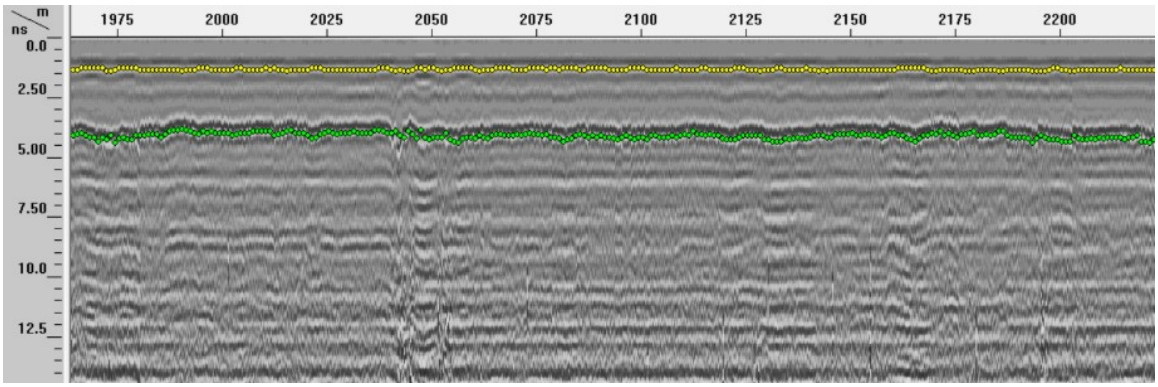

Al-Qadi and Lahouar used a GPR system to estimate pavement layer thicknesses and presented the limitations of the system using field tests. The results indicated GPR to be a reliable tool to estimate pavement thickness (see Figure 20). However, the accuracy of GPR was observed to decrease where at least one thin layer existed in the pavement structure. The authors recommended using signal processing techniques to minimize errors in pavements with thin layers *[57]*.

Figure 19. Comparison between GPR estimated thicknesses and design thicknesses for the HMA and base layers of Route 288 *[57]*

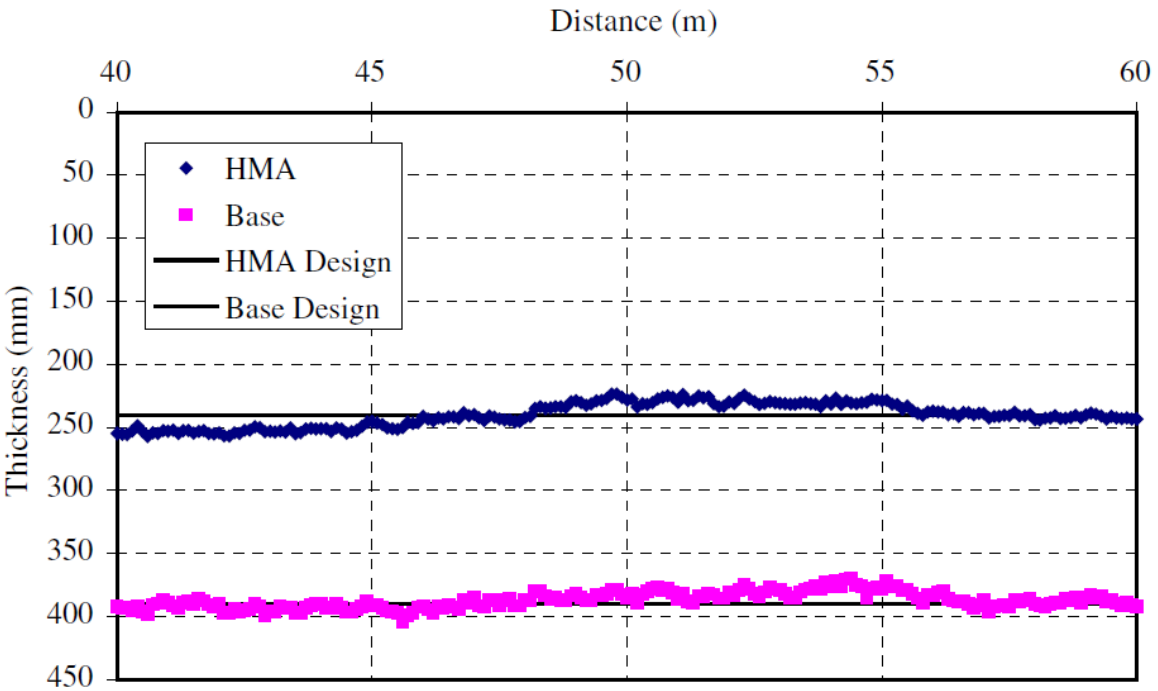

Application of GPR in Moisture Damage Detection. The change in air void contents in the pavement materials is usually an indication of pavement damage in flexible pavements *[63]*. However, detection of voids changes in pavement materials underneath the pavement surface can be a challenging task. GPR is an effective tool to detect voids in pavement materials caused by pavement distresses. Based on their results, Rmeilli and Scullion suggested that intermittent negative peaks in flexible pavements is indicative of stripping. However, researchers suggest that these peaks can also be generated from an internal layer with different dielectric properties. Thus, it is recommended to validate the GPR interpretation results with pavement cores *[[2]]*.

The Texas Department of Transportation investigated the reliability and accuracy of GPR to assess subsurface conditions of asphalt pavements including sections breaks based on pavement layer thicknesses and conditions, average asphalt layer thicknesses, and the severity and extent of pavement defects *[[2]]*. Scullion and Rmeili were able to detect stripping in asphalt layers using GPR where the deterioration was at a moderate to severe level. GPR data collected at 50 mph using the Pulse Radar Inc. antenna were first processed with color display feature of TTI's COLORMAP software. Figure 20 presents an illustration of the results collected to detect stripping damage. The pavement selected for the study was constructed initially as a concrete pavement (with a slab thickness of 8 in.) in 1960s and 1970s. Since then, the sections were rehabilitated with multiple layers of AC overlay. As shown in Figure 20, the red variable line at an approximate depth of 4 to 8 in. represents the top of the concrete layer. Figure 20(a) presents the pavement with the layers identified with no other significant reflections indicating a homogeneous pavement without subsurface deterioration. Figure 20(b) was interpreted as an asphalt pavement with moderate to severe levels of stripping at a depth of 3 in. underneath the surface. The interpretation of GPR results was validated with pavement cores. Figure 21 presents a comparison of the GPR trace with the conditions of a core.

Figure 20. A comparison between (a) a sound pavement structure and (b) a pavement with stripping *[2]*

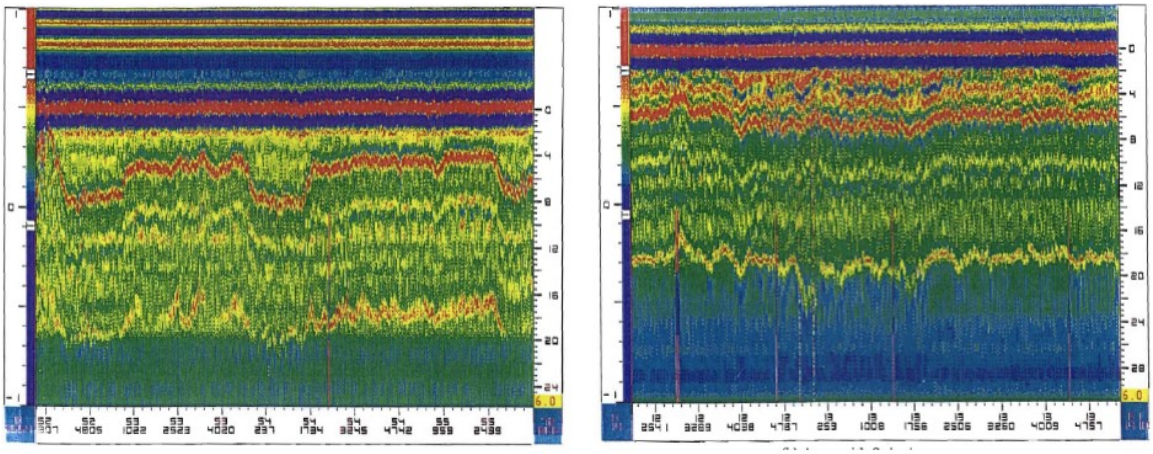

(a) (b)

It was reported that asphalt sections with stripping had higher moisture contents, higher air voids, or both; which resulted in an anomalous change in the dielectric constant of the stripped layers. It was also concluded that intermittent negative peaks within the surface layer in a GPR scan was typically an indication of the presence of stripping in the asphalt layer of the pavement as shown in Figure 21. As shown in this figure, GPR was successful in identifying pavements with moderate to severe deterioration as there has to be a distinct difference in the dielectric properties between the layers.

Figure 21. Intermittent negative peaks indicating stripping *[2]*

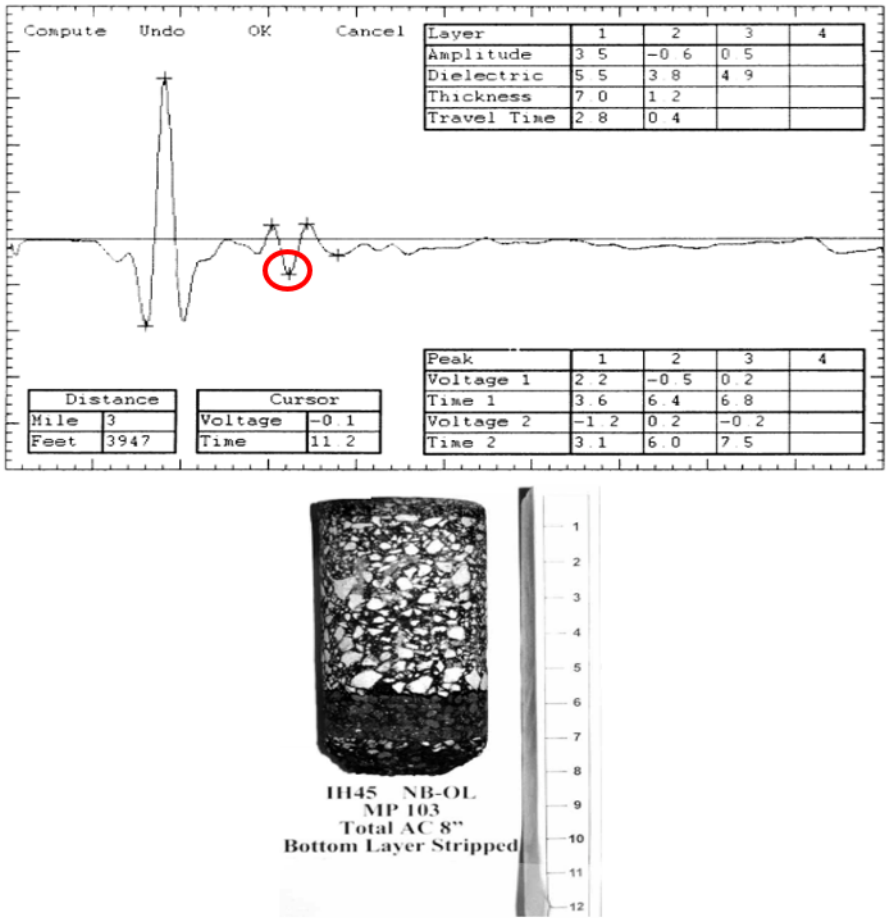

Cao et al. studied the capabilities and limitations of GPR in local road applications and pointed out that the effectiveness of a GPR survey is highly dependent upon the site conditions, the type of equipment used, and the skill of the personnel interpreting the results *[[1]]*. The study evaluated the GPR's potential to assess stripping based on the criterion that high oscillations in the surface amplitudes would indicate near surface stripping and strong internal reflection that varies with depth in GPR scans would indicate internal stripping. In wet environments, the study concluded that GPR scans along the asphalt bases were strongly bending downward and the dielectric values were significantly greater for the severely stripped sections as the voids were filled with water. Yet, no quantitative measure was introduced in the study to evaluate stripping using GPR.

Another study by Adcock et al. developed a sophisticated vehicle with a GPR antennas of 2.5 GHz and 900 MHz to study the variations in layer thickness, air void contents as well

as moisture penetration in U.S. airfield pavements *[58]*. The high-frequency antenna was used to assess the dielectric properties of the surface materials whereas the lower frequency antenna was used to estimate the subsurface layer thicknesses of the pavements. The system was initially developed to be fully automated, but the authors recommended some manual input to interpret the data more accurately. The study concluded that GPR can predict layer thicknesses with an accuracy of ±5%.

Hammons et al. developed an asphalt pavement survey protocol using GPR, IR, Seismic, and Falling Weight Deflectometer (FWD) to effectively detect stripping in in-service pavement *[64]*. The study introduced a Stripping Index (SI) to quantitatively evaluate the potential locations and extent of stripping. The stripping index was defined as:

$$SI = \frac{|A_2| - A_{2threshold} + A_{3threshold} - A_3}{5000} \quad (10)$$

Where, A_2, A_3 = the reflection amplitudes from the asphalt layers.

Each scan produced by GPR that represent 20 nanoseconds of round-trip travel of the wave was quantitatively represented as 256, 16-bit data samples. The stripping was likely to occur either if A_1 or A_2 is non-zero value or A_2 is greater than $A_{2threshold}$ or A_3 is less than $A_{3threshold}$. The threshold value for A_2 and A_3 were established to be 8,000 and 18,000 respectively. The authors plotted the stripping index against the core condition ratings and observed that a stripping threshold of 0.5 produces a good match between the SI and core condition. Figure 22 presents the plot of SI and core condition index for a section. The accuracy of GPR SI to identify stripping on flexible pavements was measured against visual core observations and was calculated to be 77%.

The SI ranged from 0 to 3, where 0 represented good conditions and 3 represented severe stripping. When the estimated SI values were compared with the actual core conditions, the study reported that GPR-predicted stripping had a 77% accuracy. The study further attempted to correlate stripping predictions from GPR with adjusted seismic and elastic modulus values, but no significant relationship was observed.

Figure 22. GPR stripping analysis, I-20 Lane 2, STA 820 to 970 *[64]*

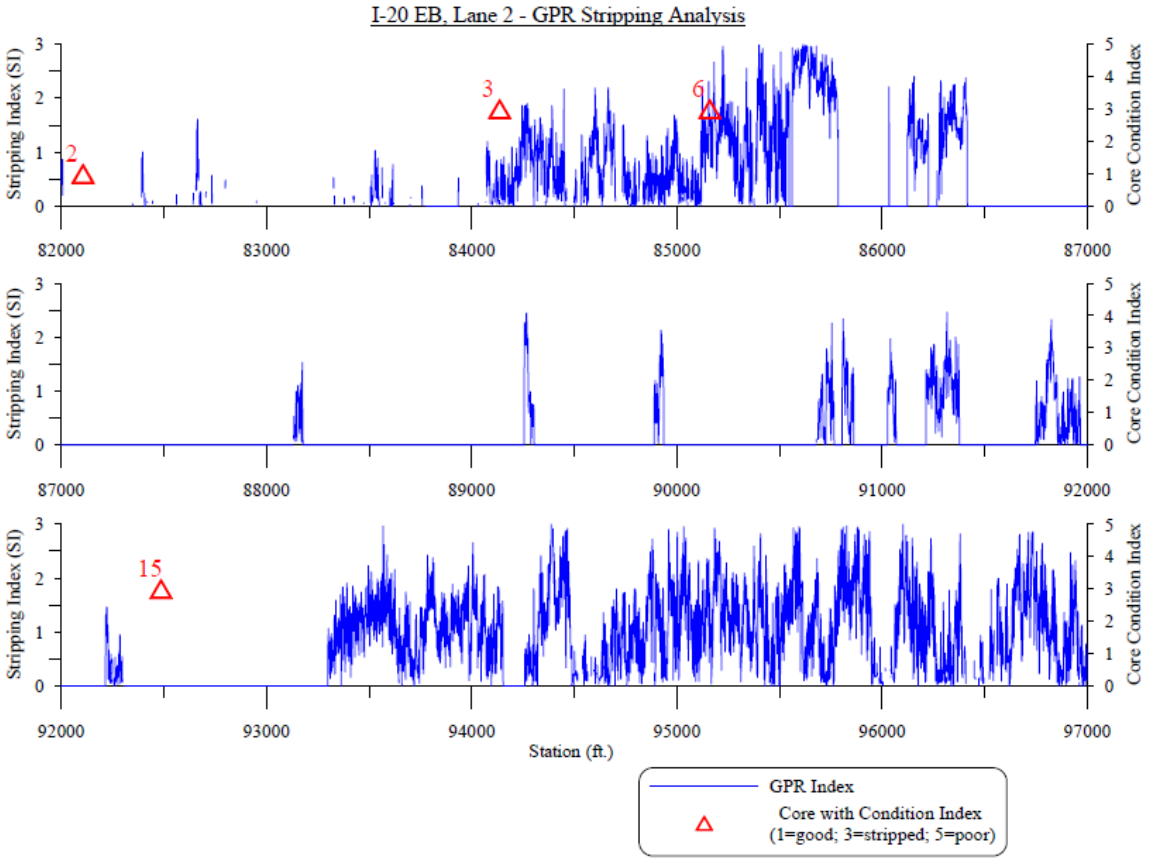

Hammons et al. introduced the uniformity index (UI) to identify potential locations that might have experienced damages related to moisture *[[3]]*. The uniformity index was defined as follows:

$$UI\ (x) = \frac{\overline{A}(x)}{\overline{A}\left(x \pm \frac{L}{2}\right)} \tag{11}$$

Where, $\overline{A}$= Average reflection amplitude at current location, x= Current station, and L= Normalization length.

As the presence of stripping is associated with strong reflections from the bottom of the HMA layer, the index showed changes in reflection activities by comparing values from neighboring locations. The estimated UI was used to map the potential locations for moisture damage as illustrated in Figure 23. The authors recommended to use shorter normalization length to identify local anomalies. The authors also suggested to use GPR

in combination with seismic technologies in order to improve accuracy in detecting stripping in hot-mix asphalt.

Figure 23. Uniformity index plot for I-75 project *[3]*

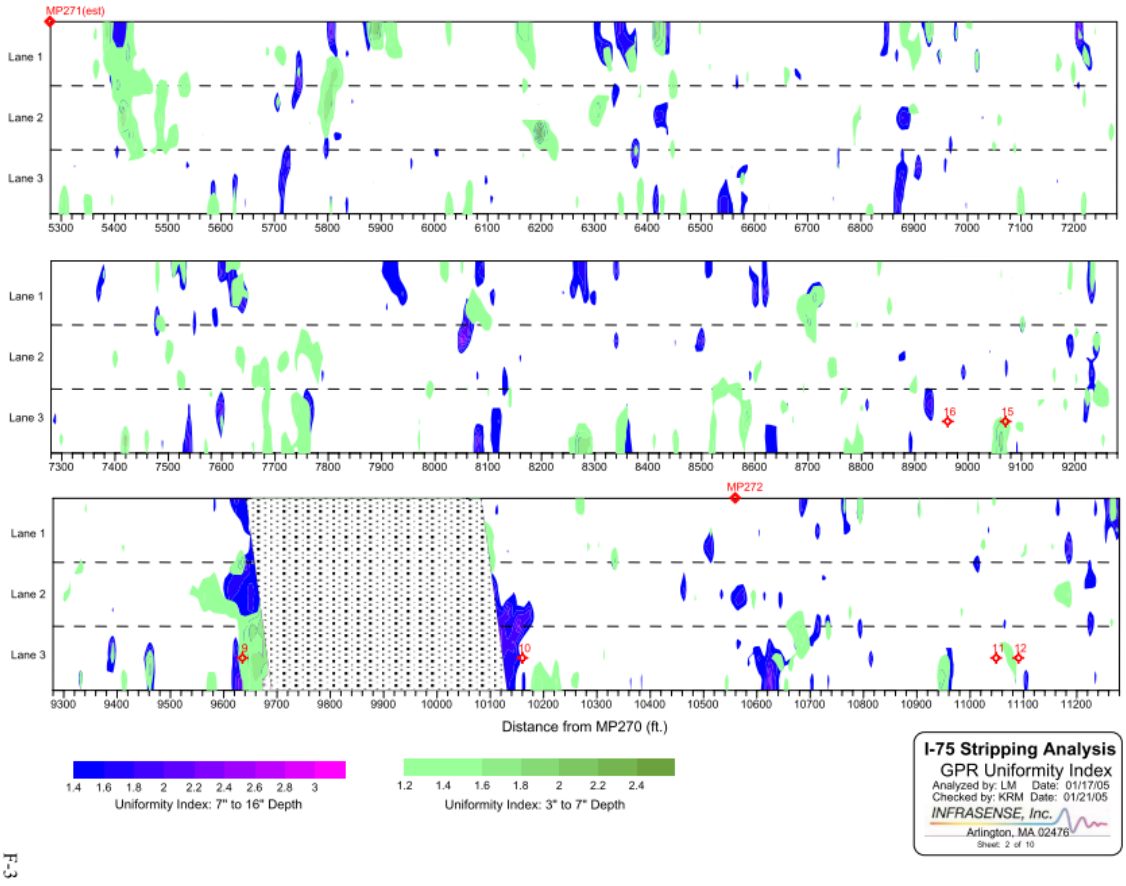

Khamzin et al. investigated full depth asphalt pavements using air launched GPR to differentiate between pavement layers, map the variable thicknesses of the pavement layers, assess pavement conditions, and develop optimum acquisition and processing parameters *[65]*. The GPR consisted of a GSSI SIR-30 system equipped with two high frequency 2 GHz air-launched antennae. The antennae were mounted on the front of the survey vehicle with the effective investigative depth of approximately 30 in. The amplitude and arrival time of GPR signals from the base of the pavement layers were analyzed to assess the roadway conditions. The lower reflection amplitudes were observed in the areas of layers' debonding indicating that the reflection amplitude depends primarily on the nature of the layer interface rather than the contrast in dielectric constants between the pavement layers. The authors also indicated that the change in

apparent thickness of the pavement layers could be indicative of material quality variations or presence of moisture. However, the actual changes in thicknesses or inhomogeneity of the material can also show the apparent change in layer thicknesses.

Falling Weight Deflectometer. FWD uses a circular plate to load the pavement structure and to measure surface deflections. A deflection basin can be obtained by measuring the deflection at various distances from the applied load, which can be useful in estimating pavement layer moduli. Stubstad reported that the shape of the deflection basin may be related to the bonded layer stiffness and that the underlying layers do not significantly affect the basin shape *[66]*. A study was conducted to identify moisture damage based on FWD estimated layer moduli and was cross-validated with the results from GPR and visual inspection of cores. The authors reported that no statistical difference was found between FWD estimated asphalt layer modulus of stripped and non-stripped cores. AC modulus obtained from FWD deflection basin was observed to be insensitive to moisture damage within a thin layer sandwiched between thick asphalt layers. To this end, no correlation was suggested between FWD predicted modulus and the presence of moisture damage *[[3]]*.

In summary, past studies reported that NDE devices such as GPR and PSPA have the potential to detect AC stripping; however, due to limitations in operation and measurement systems, these devices are yet to reach widespread implementation potential. Continuous and high-speed evaluation using TSDDs may greatly benefit transportation agencies by allowing early detection of AC stripping and the ability to address these distresses at the network level. As of yet, no agencies have been able to incorporate AC stripping damage as part of pavement condition evaluation, pavement management, and treatment selection.

Objective

The main objective of this study was to develop non-destructive field-testing methods to identify and detect moisture damage and to classify surface cracking in flexible pavements as top-down or bottom-up cracking. In addition, the effect of moisture damage on the performance and cost-effectiveness of asphalt concrete (AC) overlay and chip seal was evaluated. The study also developed a deep-learning model to predict pavement roughness conditions based on the analysis digital images of pavement surface.

Scope

To achieve the moisture detection objective, field data and roadway cores were used to evaluate the capabilities of GPR in detecting the presence, extent, and severity of stripping in in-place pavement sections. Based on the findings, a novel GPR-based indicator, known as the Accumulating In-layer Peaks (AIP), was introduced to detect stripping damage in asphalt pavements. Second, the deflection measurements of a Traffic Speed Deflection Device (TSDD), namely the Rolling Wheel Deflectometer (RWD), were evaluated to identify pavement sections that may suffer from stripping and moisture damage. Statistical and Artificial Neural Network (ANN) models that used RWD measured deflections, pavement characteristics, and performance data as inputs were developed to predict the probability of stripping damage in the tested sections. A logistic model that considers the linearity between predictor and response variables was also developed and validated with reasonable accuracy in estimating stripping probability.

To achieve the crack classification objective, machine learning models were developed to classify pavement cracks as top-down, bottom-up, and cement-treated reflective cracking based on pavement images and pavement and crack characteristics. In this task, an image-based CNN model was developed that analyzes pavement surface images. Furthermore, a one-step decision-making tool was developed using ANN to cross-validate the crack classification obtained from the imaged-based CNN model.

To assess the effect of AC stripping on the performance and cost-effectiveness of chip seal and overlays, the average deterioration rate (ADR), extension in pavement service life (ΔPSL), increase in average pavement condition (PI), and cost-effectiveness (CE) were determined for stripped and non-stripped sections.

To predict pavement roughness from collected surface images, machine learning models were developed in order to classify pavement sections into different roughness categories and to estimate IRI values using pavement surface images. In addition, the effectiveness of ANN and MNL regression models to categorize pavement sections into different roughness conditions was investigated.

Methodology

The research approach adopted in this study consisted of collecting and reviewing PMS, RWD, and GPR data collected by DOTD. The analysis consisted of identifying pavement segments that had moisture-induced damage as identified from extracted cores and the methods of repair used in these sections. In addition, PMS data were analyzed in order to attempt to identify top-down cracking without core extraction. Researchers also collaborated with LTRC staff to extract pavement cores from the field in order to validate the crack classification models.

Pavement Cracks Classification Using Machine Learning

To achieve this objectives of the study, the research tasks were conducted in two stages. In the first stage, a comprehensive literature review was conducted prior to undertaking the tasks in both phases in order to gain more insights into the subject. The pertinent literature on top-down cracking, Louisiana PMS, image-based crack identification methods, latest advancements in image-based crack detection techniques, and artificial neural network were reviewed. CNN and ANN models were then developed for identification and crack classification in flexible pavements.

In-service flexible pavement sections were selected for analysis based on the parameters identified for these sites. Images were acquired for in-service pavement sections exhibiting top-down, bottom-up, and CT reflective cracking. These images were further processed to include in the training, testing, and validation sets for the developed crack classification CNN models. At once, design input variables namely pavement age, AC thickness, annual average daily traffic (AADT), type of base, crack orientation, and crack location, were also collected to use in the training, testing, and validation sets of the ANN-based decision-making model. The research methodology is explained in detail in the following sections.

PMS Data Collection

The images for analysis of pavement cracks were obtained from the DOTD PMS inventory. The pavement network in Louisiana is surveyed every two years using the ARAN system, which acquires continuous high definition digital images of the pavement surface. The images for top-down cracking were collected from the PMS inventory based

on the field verification of these cracks with coring. The sections with potential top-down cracks were first identified based on the characteristics of these cracks as suggested in the literature before cores were extracted for verification. To collect the images with bottom-up fatigue and CT reflective cracks during the early development phase, sections with typical bottom-up alligator cracks (fatigue) and CT reflective cracks at specific locations were first identified using video surveys and were then projected back to previous year's survey for the same locations. Table 3 presents the total number of surface images collected for each crack pattern.

Table 3. Image data collection for each crack type

Crack Type	Number of Control Sections	Number of Images
Top-down cracking	9	162
Bottom-up cracking	10	66
CT reflective cracking	9	122

Pavement Sections Selection for Top-Down Cracking

Pavement sections with longitudinal cracks in the wheel path were selected as shown in Figure 24. Pavement design and the time of rehabilitation/construction were the main factors in selection of the pavement sections. Table 4 presents the pavement sections selected in the analysis.

Table 4. Pavement sections selected in the analysis

Control Section	District	Parish	Construction Date	Route
057-03	3	1	4/24/2015	LA 13
058-02	62	52	12/6/2012	LA 41
262-03	62	32	12/17/2013	LA 16
266-01	61	3	4/26/2013	LA 22
829-26	2	29	7/12/2013	LA 3235
857-63	3	57	5/28/2013	LA 82
015-05	58	30	10/15/2012	US 165
019-05	61	63	3/20/2012	US 61
030-04	62	59	11/1/2012	LA 21

Figure 24. Illustration of pavement section selection for top-down cracking from PMS data

Field Validation of the Sections for Top-Down Cracking

To validate the cracking propagation direction in the selected sections, pavement cores were obtained along the wheel path. The location coordinates of the sections with top-

down cracks were first identified from the project maps in PMS such that these locations corresponded to the pavement images locations obtained from PMS for image analysis. The cores were extracted at the tip of the longitudinal cracks such that the orientation and propagation of the cracks could be verified, see Figure 25. The drilled holes at the sites were carefully investigated to validate the top-down propagation of the cracks for the cores that fragmented during coring. As shown in the figure, the cracks started at the pavement surface and propagated downward through the AC layer.

Figure 25. Acquisition of field cores, (a) marking core extraction location, (b) coring the marked location, (c) careful extraction of core, (d) extracted pavement core

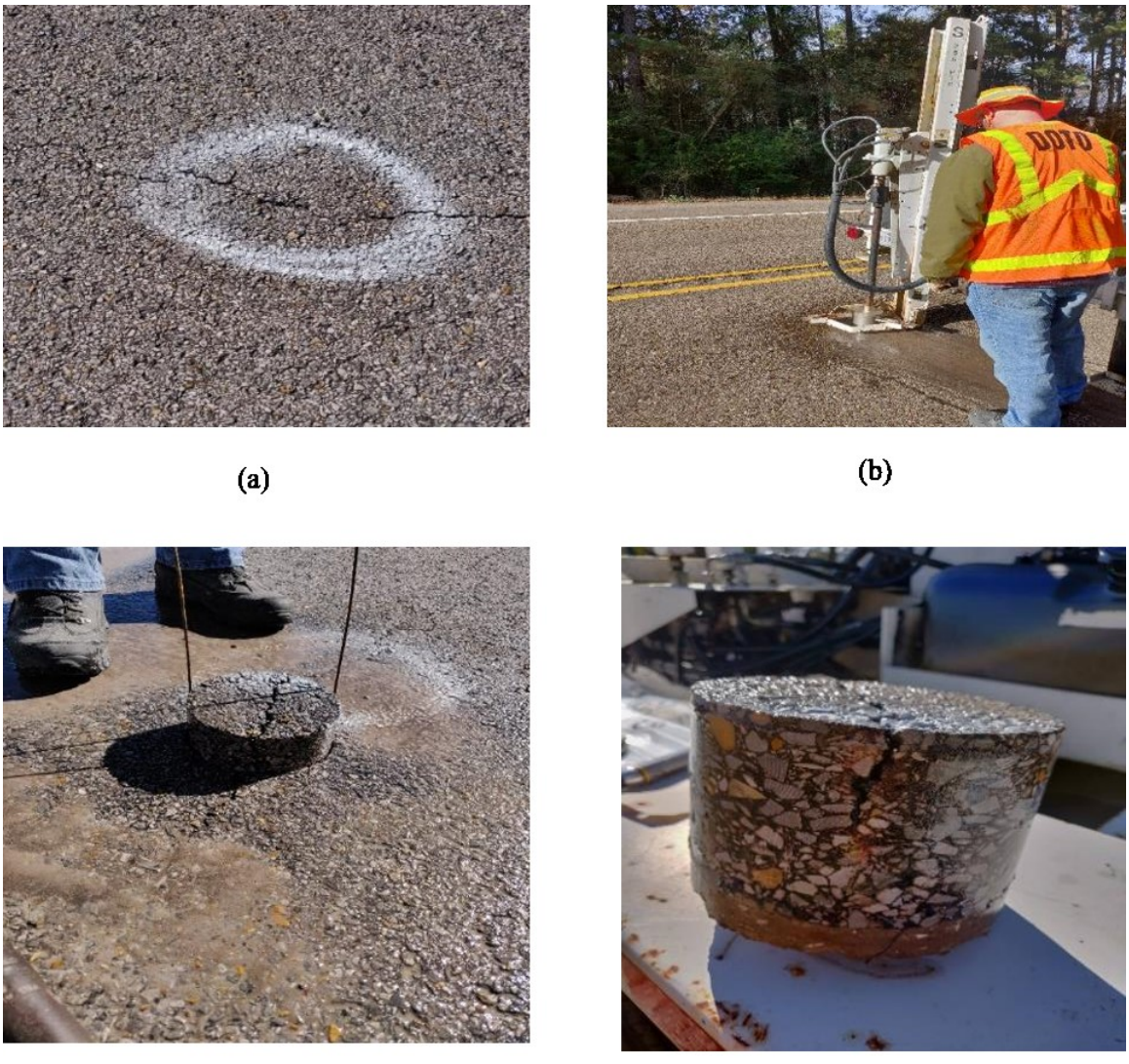

Field cores with longitudinal top-down cracking for two pavement sections are presented in Figure 26. It is evident from the field cores that the crack started at the top of the AC layer. Table 5 summarizes the information obtained from the cores for the six pavement sections. Based on field cores observation, the cracks were observed to extend up to a depth of 25 to 100 mm from the pavement surface. The top-down propagation of the cracks was also confirmed in the field with the drilled holes as some of the cores were fragmented during coring. Figure 27 presents an illustration of the fragmented cores and the corresponding drilled hole.

Figure 26. Cores showing longitudinal top-down cracks for control sections (a) 829-26, (b) 857-63

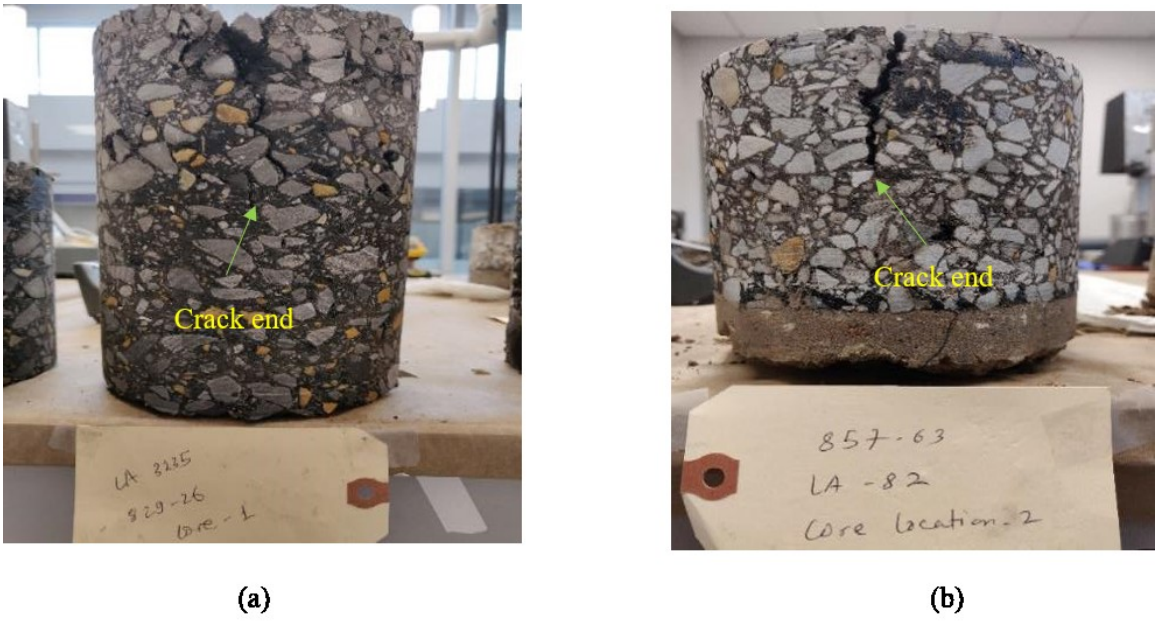

(a) (b)

Table 5. Summary of coring observations

Control Section/Route	AC Thickness (mm)	Crack Depth (mm)	Crack Width (mm)	Vertical Orientation
057-03 / LA 13	317.5	50	3	Top-down
058-02 / LA 41	203.2	25	3	Top-down
262-03 / LA 16	215.9	65	6	Top-down
266-01 / LA 22	355.6	50	4	Top-down
829-26 / LA 3235	203.2	95	3	Top-down
857-63 / LA 82	203.2	45	4	Top-down

Figure 27. Drilled hole and fragmented core

(a) (b)

Pavement Sections Selection for Bottom-Up and Cement Treated Reflective Cracking

The sections selected for bottom-up and cement-treated reflective cracking are presented in Table 6 and Table 7, respectively. Figure 28 and Figure 29 present the procedure used for the selection of bottom-up and cement treated reflective cracking images from PMS. As shown in Figure 28 and Figure 29, pavement sections with typical bottom-up and cement-treated reflective cracking were identified in 2016. The locations of the cracks on these sections were then projected back to previous years' surveys until the crack initiation phase was reached. The digital images for the year when the cracks initiated at the pavement surface were then used to develop the deep learning models.

Table 6. Pavement sections with bottom-up fatigue cracking

Control Section	District	Parish	Construction Date	Route
852-12	62	52	10/18/2001	LA 0434
034-03	8	43	10/28/2003	LA 0006
193-06	7	10	8/8/2007	LA 0014
262-02	62	32	N/A	LA 0016
273-03	62	32	8/2/1996	LA 0064
391-02	3	28	12/20/1996	LA 0098
053-01	8	40	7/11/1996	LA 0001
414-02	61	24	7/19/1991	LA 0030
828-03	3	28	7/19/1995	LA 723
034-04	8	35	7/17/2003	LA 0006

Table 7. Pavement sections with cement treated reflective cracking

Control Section	District	Parish	Construction Date	Route
014-06	8	40	5/8/2008	US 0165
015-02	8	40	6/4/2001	US 0165
048-01	4	9	8/25/2000	US 0079
054-05	7	27	7/18/2000	LA 0026
012-12	3	49	2/21/2013	US 0190
019-05	61	63	9/2/2003	US 0061
027-04	4	60	1/25/2006	US 0079
260-01	61	3	2001	LA 0042
273-03	62	32	1999	LA 0064

Figure 28. Pavement section selection for bottom-up fatigue cracking

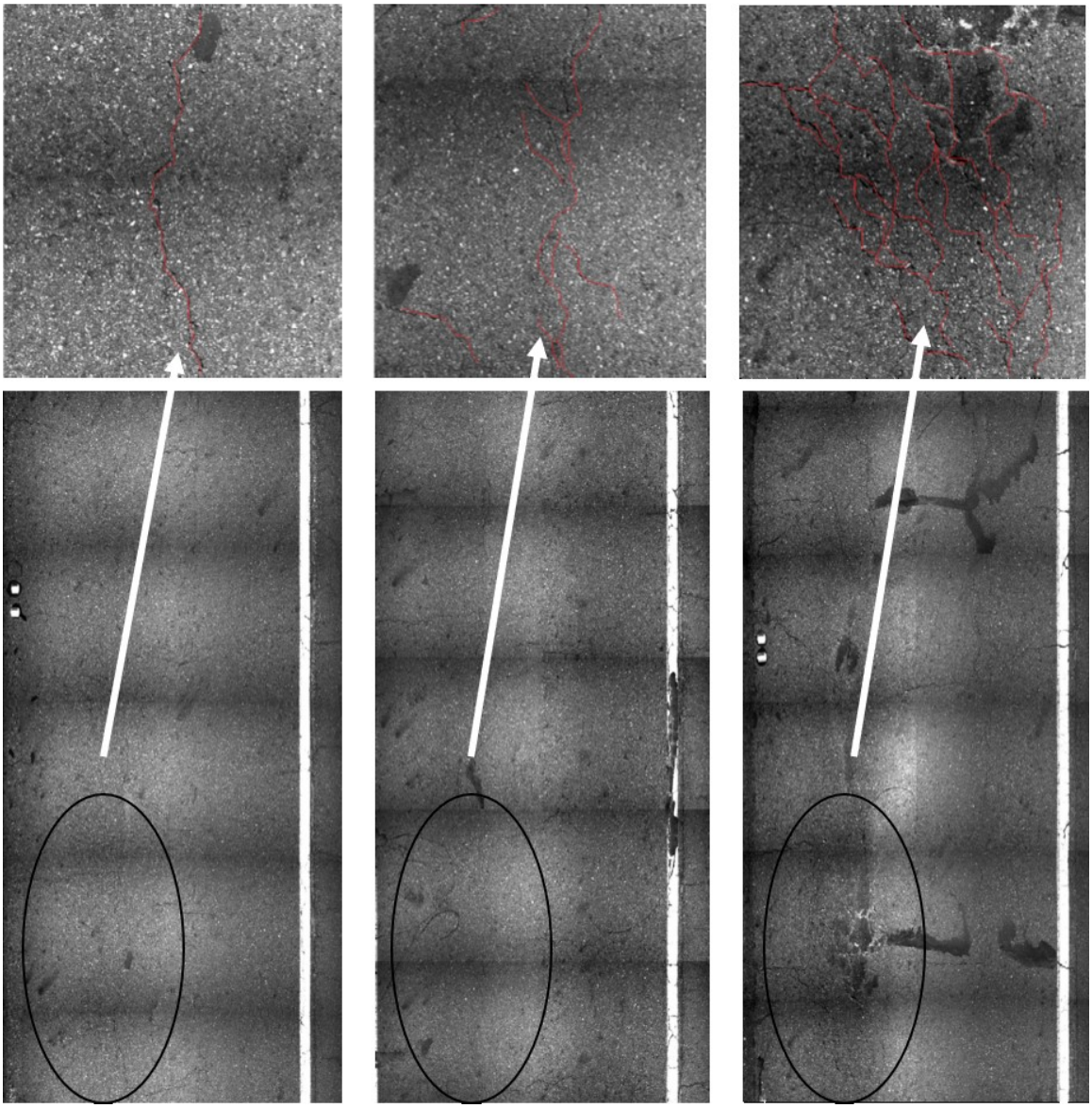

Figure 29. Pavement section selection for cement treated reflective cracking

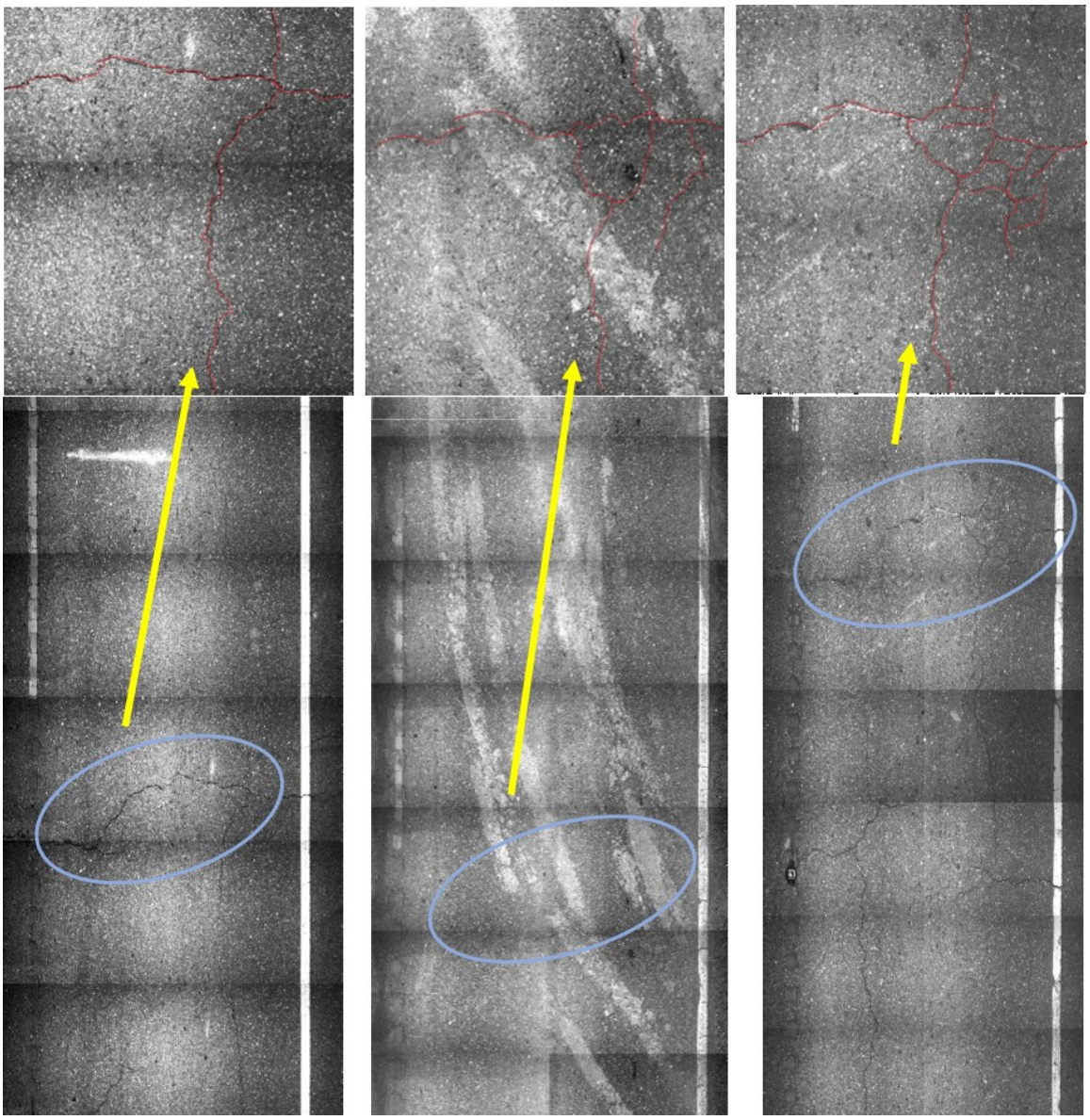

Image Pre-Processing

The objective of this step was to process the pavement images obtained from the DOTD PMS to enhance the cracks from the background and noise in order to use them in the training, testing, and validation data sets in CNN. The image pre-processing technique involved five major steps namely image acquisition, median filtering, morphological erosion, contrast enhancement, and background subtraction as illustrated in Figure 30.

The detailed description of the image acquisition and processing techniques is presented in the following sections.

Figure 30. Illustration of processed input images for (a) top-down cracking, (b) bottom-up cracking, and (c) CT reflective cracking

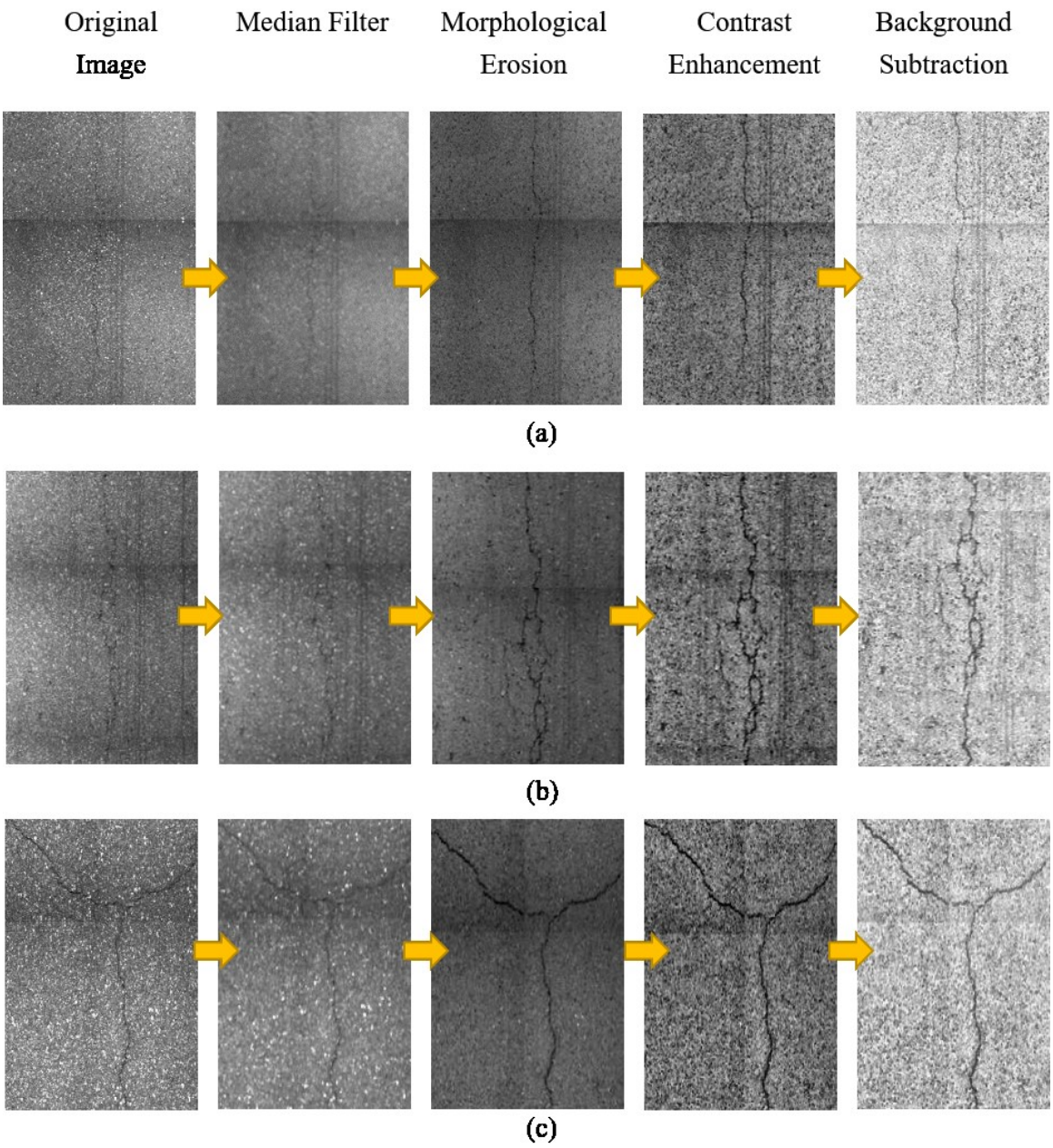

Image Acquisition. The objective of this step was to extract the pavement images from the DOTD PMS for the sections presented in Table 6 and Table 7 and at the locations for which the cracks were identified and were back-projected to the initiation phase.

Noise Reduction and Crack Enhancement. This step involves the visibility enhancement of particular features in the pavement images with the application of specific enhancement and mathematical operations for 2D images. The image pre-processing using different enhancement techniques intensifies cracks from random backgrounds that include pavement surface texture, roughness, patches, spots, stains, raveling, and road markings. The selection of appropriate filters is an important step in image pre-processing in order to remove excessive noise while preserving the edges of the objects of interest.

Crack Enhancement for 2D Images. The pavement noise reduction was achieved using a space-domain image filtering technique known as a Median Filter (MF). This nonlinear filtering technique has been widely used in the processing of pavement images as it has the advantage of removing background noise with low level of blurring compared to mean filtering and Gaussian filter. The results of an application of 3x3 MF are presented in Figure 30. The image pixels of the original pavement images were replaced with the median of its neighboring pixels while preserving the crack edges.

A morphological image processing technique known as gray scale erosion was applied for further noise reduction and crack enhancement. The erosion of image I and the structuring element S is defined as follows *[67]*:

$$I \ominus S = \min[I(x + x', y + y') - S(x', y') \mid (x', y') \in D_s \quad (12)$$

Where, Ds = the binary matrix, S = the domain of structuring element (which defines which neighboring pixels are included in the minimum function), and I(x, y) is assumed to be +∞ for (x, y).

The best possible contrast distribution of pixel values was achieved using local contrast enhancement. The image was then subjected to background subtraction, which removes gels and shadows from the smooth continuous background. Figure 30 illustrates the overall noise removal and image enhancement techniques employed for image data preparation of each crack type.

Crack Enhancement for 2D and 3D Images. A CNN-based crack classification tool was developed for a combination of both 2D and 3D images. A similar approach for median filtering, morphological erosion, and contrast enhancement as described in the previous section was applied for the combination of 2D and 3D images. However, before the application of aforementioned operations, the images were first subjected to intensity normalization, which removes the non-uniform background in the pavement images. The application of intensity normalization is illustrated in Figure 31. The pixel intensity in a pavement image can be represented by the following equation *[[23]]*:

$$S(p) = S_b(p) + S_c(p) + S_n(p) \quad (13)$$

Where, p = a pixel in a pavement image, S(p) = the intensity of the pixel, and $S_b(p)$, $S_c(p)$, and $S_n(p)$ = the background illumination signal, crack component signal, and signal due to noise.

The objective of this step is to arbitrarily normalize the background illumination signal into a constant intensity value. The non-uniform background removal method proposed by Ying and Salari was implemented with some modifications, which consisted of the following steps *[[23]]*:

- The image was partitioned into the rectangular windows of size 64*64.
- For each window, the mean (G_{mean}), minimum (G_{min}), and the maximum (G_{max}) of the gray level was calculated.
- An upper (l_u) and lower limit (l_l) of gray intensity pixel was defined for each window. The pixels outside these limits were considered as suspicious points for noise, cracks, and other variations. A limiting factor of 50% was chosen for our images. The limiting range was calculated using following equation.

$$l_u = G_{mean} + (G_{max} - G_{mean}) * 50\% \quad (14)$$

$$l_l = G_{mean} - (G_{max} - G_{mean}) * 50\% \quad (15)$$

- An updated mean value (G'(mean)) was calculated for each window, which represents the mean for each window without considering the noise and crack pixels.
- The background of each window was normalized by multiplying every point window with a amplitude correction factor f, which was calculated as f = S/G'(mean), where S is the target background value or the mean value of the original image.

Figure 31. Intensity normalization

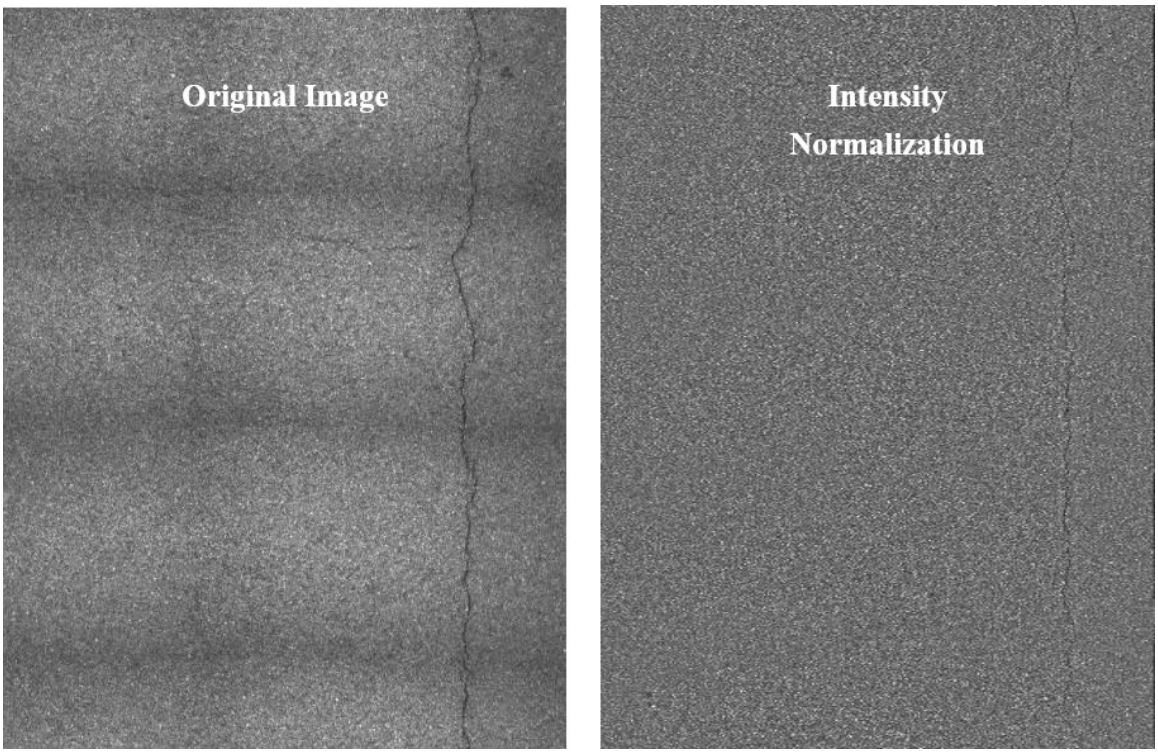

Convolutional Neural Networks Model

In this study, an image-based crack classification model was developed using deep learning techniques through transfer learning and domain adaptation approach. The procedure involved the use of a pre-trained CNN model known as AlexNet *[68]*, which was developed and trained based on a massive database containing millions of images as a feature generator for pavement images. The pre-trained classifier was trained with labelled pavement images to predict the crack types (i.e., top-down, bottom-up, or cement treated reflective cracking). The pavement cracks can be classified accordingly using a sliding window and a CNN classifier that was generated through the training process *[43]*. The developed model automatically generates the crack feature sets based on the input images to classify the cracks into the three categories (i.e., top-down, bottom-up, or cement treated reflective cracking).

AlexNet Architecture. The present study built a CNN model by modifying the AlexNet, which is a widely recognized pre-trained CNN model for image classification. The architecture of the modified CNN network is illustrated in Figure 32. Typical CNN models consist of convolutional layers, max pooling layers, and fully connected layers.

The modified network had five convolutional layers with three max-pooling layers and three fully connected layers as shown in Figure 32.

Figure 32. CNN's overall architecture *[43]*

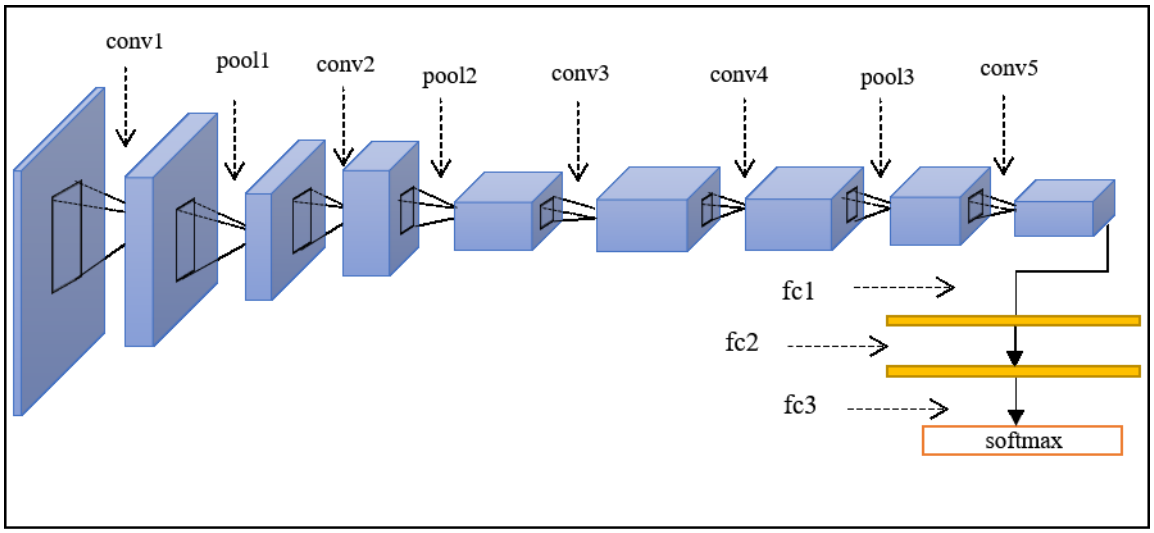

conv# = convolution, pool# = pooling, fc# = full connection

The CNN architecture also included other operations namely rectified linear units (ReLU), local response normalization (LRN), and dropout. The ReLU is used as activation function after each convolution layer and the first two fully connected layers; LRN is used before the first two pooling layers, and the dropout is used after first two fully-connected layers. The softmax layer, consisting of three units for classification of input data, was located at the end of the CNN's structure. The overall architecture consisted of 25 layers with 24 connections.

The objective function was optimized using stochastic gradient descent (SGD) algorithm with momentum and "on-line" or incremental training characteristic, which updates the network parameter after each input during the training process. Through an iterative procedure, SGD minimizes the loss function E(i) = D(D(i), F(W, Z(i))), which measures the deviation of the true output "D" for input "Z" from output generated from the CNN function F(W, Z) *[43]*. The SGD was used with the initial learning rate of 0.01 and the momentum, weight decay, and dropout rate were set to 0.9, 0.0001, and 0.5, respectively. The classifiers were trained for 8 epochs with a batch size of 25.

The input sets consisted of 162, 66, and 122 pavement images for top-down, bottom-up, and cement treated cracks, respectively. The patch size was set to 227 x 227 to save computing time before feeding the CNN with the training images. The first and second convolution layers convoluted the image matrix into 11 x 11 and 5 x 5 pixel-sizes, respectively, to obtain an improved noise suspension while other convolution layers were equipped with kernel of 3 x 3 and a stride of 1. The max pooling was performed in a filter size of 3 x 3 with a stride of 2. Table 8 presents the detailed specifications of the different layers of the CNN model.

Table 8. Detailed specifications of CNN model

Layer	Filter size	Stride	Padding	Activations
conv1	11*11	[4 4]	[0 0 0 0]	55*55*96
pool1	3*3	[2 2]	[0 0 0 0]	27*27*96
conv2	5*5	[1 1]	[2 2 2 2]	27*27*256
pool2	3*3	[2 2]	[0 0 0 0]	13*13*256
conv3	3*3	[1 1]	[1 1 1 1]	13*13*384
conv4	3*3	[1 1]	[1 1 1 1]	13*13*384
conv5	3*3	[1 1]	[1 1 1 1]	13*13*256
pool3	3*3	[2 2]	[0 0 0 0]	6*6*256
fc1	-	-	-	1*1*4096
fc2	-	-	-	1*1*4096
fc3	-	-	-	1*1*1000
Softmax	-	-	-	1*1*1000

ANN Decision-Making Tool

A decision-making tool was developed using ANN to serve as a secondary screening tool and to cross-validate the image-based classification results obtained from the CNN model. The tool used input variables related to pavement conditions and crack properties and was developed using ANN-based pattern recognition system. This was achieved by using a multilayered feed forward ANN with a hard-lim transfer function that presents the output as “0” or “1.” A scaled conjugate gradient back-propagation algorithm (trainscg) was used for the network optimization. The confusion matrices having two dimensions, one with the actual class of the input and the other with the predicted class, were used to express the accuracy of the system. Figure 33 presents a basic confusion matrix with

patterns P_1, P_2, and P_n. The N_{ij} represents the number of samples actually belonging to class P_i but classified by the ANN as class P_j *[69]*. The tool can be used separately or in conjunction with the CNN model to cross-validate the predicted crack type obtained from the image-based CNN model.

Figure 33. Confusion matrix for pattern recognition ANN *[69]*

		Predicted		
		P_1	… P_j …	P_n
Actual	P_1	N_{11}	N_{1j}	N_{1n}
	P_i	N_{i1}	… N_{ij} …	N_{in}
	P_n	N_{n1}	N_{nj}	N_{nn}

Network Inputs and ANN Structure. The input layer was fed with the simplest set of inputs corresponding to the images and that required no optimization analysis to be conducted. The input set consisted of six different variables—pavement age, base type, AADT, AC thickness, orientation of cracks, and location of cracks, which may be obtained from the DOTD PMS. Each input was divided into different classes and was assigned a numerical value. Figure 34 presents the classification and numerical values assigned to each input; the numbers in front of each class represent the assigned numerical value. Figure 35 presents the ANN structure. As shown in Figure 35, six ANN consisted of six neurons in the input layer to incorporate six different inputs and the target layer was comprised of three neurons to incorporate the corresponding prediction classes. The adequate correlations between the inputs and targets were established with a hidden layer consisting of 10 neurons by connecting each neuron in the input and target layers. An iterative process was used to select the number of neurons in the hidden layer such that the least number of hidden neurons are selected without affecting the network performance.

Figure 34. Input parameters selected in the ANN model

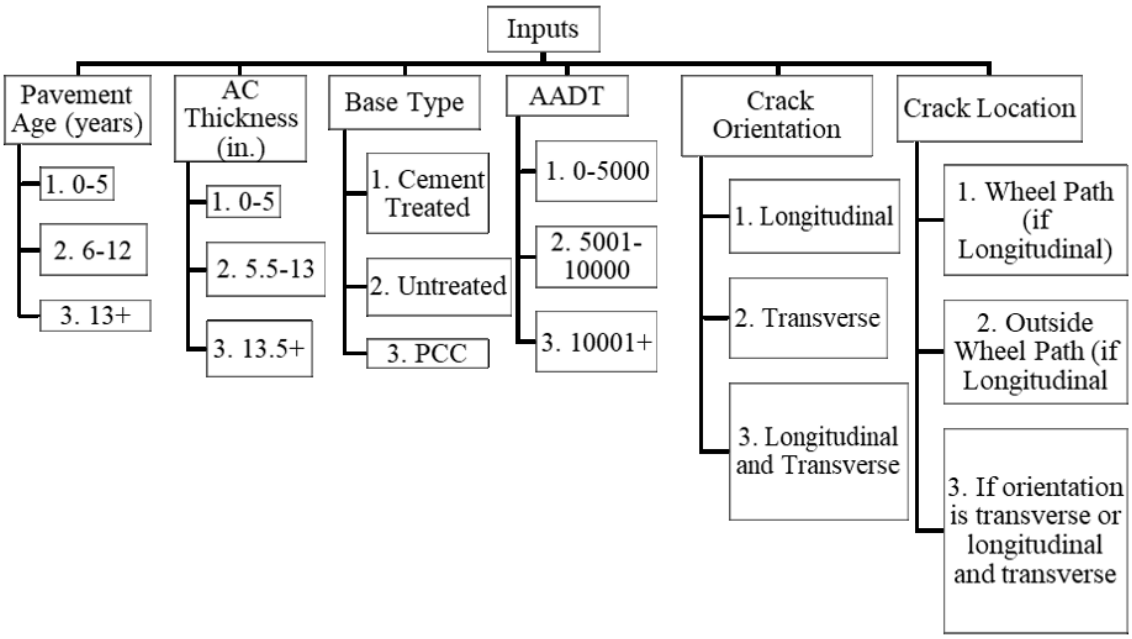

Figure 35. Structure of the ANN model

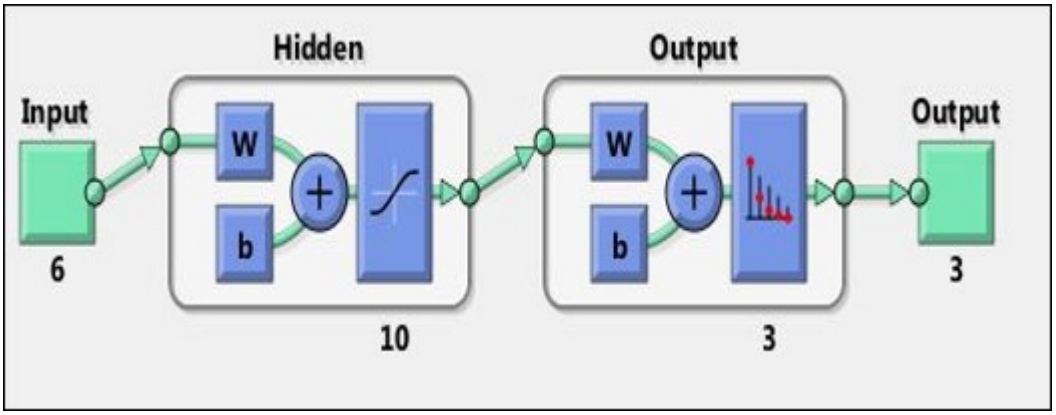

Asphalt Concrete Stripping Detection Using Deflection Measurements

A large TSDD dataset consisting of RWD measurements was used for developing and validating the AC stripping prediction models. The RWD testing program was conducted in District 05 of Louisiana as detailed elsewhere *[12]*. The testing was conducted in two phases: testing of 1,000 miles in the first phase and a detailed evaluation of RWD technology in 16 road sections (1.5-mile each) in the second phase. In each section, RWD measured deflections were considered at 0.1-mile intervals and were normalized to a

standard temperature of 20°C *[12]*. Core reports were collected for all the sections from the year of RWD testing in the wheel path. Core reports provided detailed pavement thicknesses information and detection of any distress including AC stripping in the underlying pavement layers as illustrated in Figure 36. The pavement segments that did not have any coring information available were excluded from the analysis. Thus, the total number of road segments used in this study were 192, out of which 67 pavement segments were diagnosed with stripping and the remaining pavements did not have any moisture-induced damage.

Figure 36. Cores inspection to identify AC stripping in the underlying layers

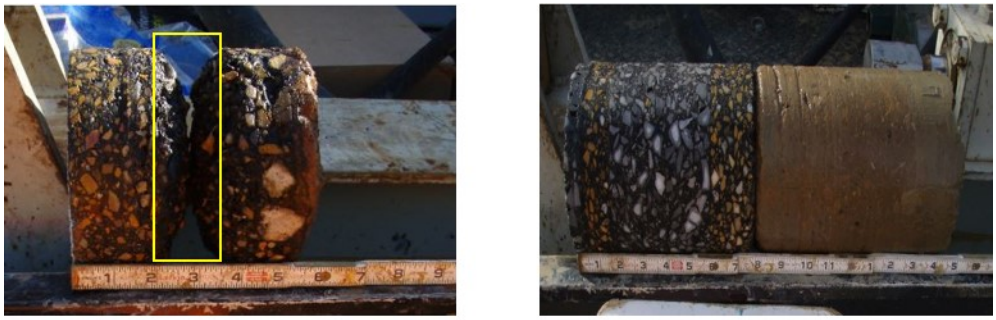

(a) Stripped cores (b) Non-stripped cores

A statistical regression model was developed to predict the Structural Number (SN) of in-service pavements at an interval of 0.1 mile based on RWD measurements as follows *[[12]]*:

$$SN_{RWD0.1} = -14.72 + 27.55 * \left(\frac{AC_{th}}{D_0}\right)^{0.04695} - 2.426 * \ln SD + 0.29 * \ln ADTPLN \quad (16)$$

Where, ACth = Asphalt concrete layer(s) thickness of the pavement structure (in.); D_0 = Avg. RWD deflection measured at an interval of 0.1 mile (mils.); SD = Standard deviation of the RWD deflection each 0.1 mile (mils.); and ADTPLN = Average Annual Daily Traffic per lane (vehicle/day).

As presented in Equation (17), the Structural Condition Index (SCI) was calculated based on the existing structural number predicted from RWD ($SN_{RWD0.1,}$ also referred as SN_{eff}) and AASHTO SN required for 10 years of design life (referred as SN_{req}) to describe pavement structural conditions as compared to the required structural capacity. The detail calculation procedure of the SCI can be found elsewhere *[[12]]*:

$$SCI = \frac{SN_{eff}}{SN_{req}} \quad (17)$$

where, SCI = Structural Condition Index; SN_{eff} = existing (estimated) Structural Number; and SN_{req} = required Structural Number for 10 years.

Initially, the SCI of stripped and non-stripped sections was compared in this study to examine any indication of stripping using TSDD measurements. The SCI of stripped and non-stripped road sections was calculated and was grouped into different pavement categories based on AC layer thickness (i.e., thick, medium, and thin) as shown in Figure 37. The comparison indicated that the SCI estimated from RWD measurements can differentiate between the stripped and non-stripped pavement segments as the average SCI was higher for non-stripped sections for all the pavement categories; see Figure 37(a). Furthermore, the SCI difference between stripped and non-stripped sections tended to increase with the increase in AC thickness, i.e., for thin pavements (4.5%), for medium pavements (8.6%), and for thick pavements (15.2%) as shown in Figure 37(b). This implies that the pavement structure characteristics may also be valuable alongside RWD measurements in identifying AC stripping. This may be due to thick pavements that include multiple AC layers, which may have been overlaid over time, and had a longer period for moisture damage to occur.

Figure 37. SCI comparison between stripped and non-stripped sections

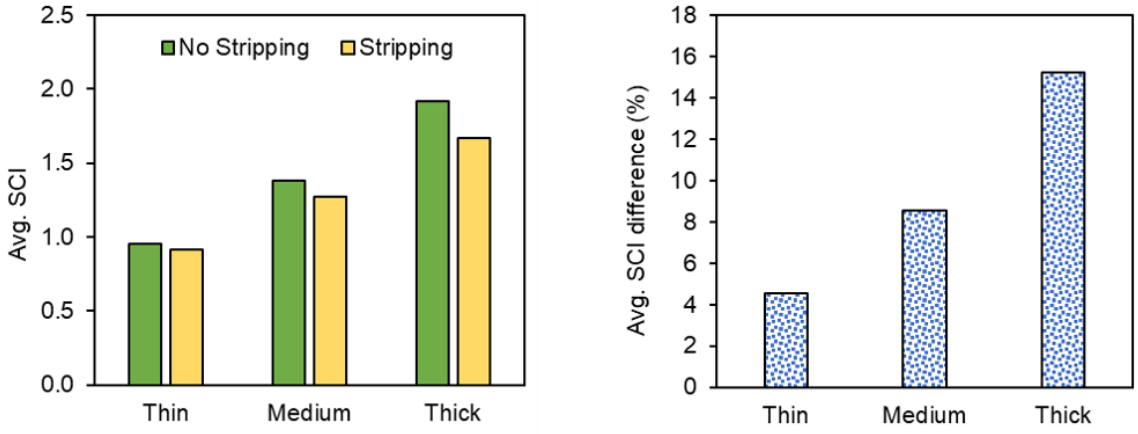

As core reports are the only real evidence of AC stripping within a road section, the available RWD measurements and pavement thicknesses were averaged over 1-mile segments such that the core location would be in the middle of the 1-mile segment. Such

an assumption was made considering the practicality related to core extraction by state agencies and would allow the measurements to reasonably reflect the stripped or unstripped conditions within a road section. Since the objective was to identify stripped sections using RWD measurements and available pavement information in the Louisiana PMS, various variables were evaluated to model the probability of moisture damage in in-service pavements in the preliminary stage. These variables were evaluated based on statistical measures and engineering judgment to decide whether to include them in the developed models. The statistical models considered to predict the probabilities of AC stripping or to identify moisture damage are presented in the following sections.

Logistic Regression Model

Logistic regression is a popular statistical method in medical studies broadly used for modeling a dichotomous outcome based on variables that may influence the outcome. Usually, logistic regression is suitable for explaining and testing hypotheses about the relationship between a categorical response variable based on continuous or categorical predictor variables *[70]*. The objective in the present study was to identify if a pavement is diagnosed with stripping damage or not, based on RWD-measured deflections and pavement structure information; this setting favored the incorporation of logistic regression over conventional linear regression models. Linear regression assumes linearity and continuity between the predictor (independent variables) and outcome variable (dependent variable), which would be invalid in the present study as the response variable is binary. In the present analysis, a value of 1 was assigned if the pavement was diagnosed with stripping damage and a value of 0 was assigned for non-stripped pavement segments.

The principal concept of logistic regression is to define the relationship between the outcome and predictor variables in terms of the natural logarithm of a likelihood ratio. Unlike linear regression, logistic regression estimates the probability of an outcome that would assist in classifying the response variable. A simple logistic regression model has the following form *[71]*:

$$\text{logit}\,(Y) = \text{natural}\log(\text{odds}) = \ln\left(\frac{P}{1-P}\right) = \alpha + \beta X \qquad (18)$$

Where, P = the probability of an event of interest, α = presented as the Y-intercept, and β = regression coefficient of the predictor variable X.

A logistic regression model was developed in the present study to predict the presence of stripping in the underlying pavement layers. To develop the logistic model, RWD-measured surface deflections, asphalt layer and base layer thicknesses, traffic data, and surface condition data (i.e., fatigue cracking, random cracking, surface roughness, and rutting) were considered as initial predictor variables. Different combinations of these variables were tested with different functions through an iterative process to obtain the most accurate model that may be used in predicting the outcome (i.e., stripping damage in pavement). For model development, 70% of the dataset was used and the remaining 30% was used for validation. The logistic model development was conducted in SAS 9.4 software. Equation (19) presents the developed logistic model:

$$\mathrm{Ln}\left(\frac{\mathrm{P}}{1-\mathrm{P}}\right) = 0.6281 + 0.000418 * (\mathrm{D}_0 * \mathrm{D}_0\mathrm{STD}) + 0.1563 * (\mathrm{ACth}) + 0.3063 * (\mathrm{TreatedBase}) - 0.02658 * (\mathrm{RTI}) \quad (19)$$

Where, P = Probability of stripping, D_0 = Avg. RWD deflection measured at an interval of 0.1 mile (mils.), D_0STD = Standard deviation of the RWD deflection at 1-mile interval (mils.); ACth = Asphalt concrete layer(s) thickness (in.), TreatedBase = whether the base is treated or not, (if treated=1, not treated =0), and RTI = Rutting index is defined as follows:

RTI =MIN [100, 100-((R_Avg*(10/0.125))-10)] (20)

Where, RTI = Rutting index (from 0 to 100); and R_Avg. = Average rut depth (in.).

Generalized Additive Models (GAM)

Generalized Additive Model (GAM) is a powerful technique that extends a linear model by integrating non-linear functions for each of the variables and captures the non-linear relationship between the dependent and predictor variables *[72]*. Compared to linear models, GAM is more flexible and does not require a functional form. However, it is hard to interpret due to its instability due to the complex dimensionality. For the general case, each term is computed in low dimensions to avoid complexity. The generalized additive models for the classification response can be written as:

$$\log\left(\frac{\mathrm{p(x)}}{1-\mathrm{p(x)}}\right) = \beta_0 + \mathrm{f}_1(\mathrm{X}_1) + \mathrm{f}_2(\mathrm{X}_2) + \cdots + \mathrm{f}_\mathrm{p}(\mathrm{X}_\mathrm{p}) \quad (21)$$

Where, f_j's = arbitrary functions estimated from the data.

The functions $f_1, \ldots, f_p$ can be polynomials, natural splines, smoothing splines, local regressions. Two common techniques in GAM are the loess smoother and the smoothing splines, which were considered in this study.

The loess smoother (locally estimated scatterplot smoothing) performs based on local fitting *[73]* and the weights are dependent on how far the distance is from those points. The closer the points, the more weighted they get. The weighted least squares for fitting the regression is as follows:

$$u_j = \frac{|z_j - z|}{\max|z_j - z|} \tag{22}$$

Where, u_j is between 0 and 1.

The Loess smoother technique is flexible to ease the parametric model's limitation to non-linear form. In addition, it suggests that the model is not mathematically proven; therefore, complicated models can be extended from the loess smoother. However, it does not perform well with a comparably small dataset, especially if it is based on empirical information to fit in the nearest points of the scatterplot.

The smoothing splines is another method in the GAM model. Spline is the collection of the knots in a piecewise polynomial *[74]*. The knot makes the discontinuity of the pieces join smoothly. The degree of the splines requires the m-1 derivatives to be continuous. The spline of degree m is defined as follows:

$$S(x) = \sum_{j=0}^{m} \beta_j X^j + \sum_{j=1}^{k} \lambda_j (x - \xi_j)_+^m \tag{23}$$

Where, λ = a smoothing parameter.

In the present study, the smoothing functions (i.e., loess smoother and smoothing splines) were combined to develop the best GAM model using an iterative process. There was 70% of the data used for training the model and the remaining 30% data were used for model validation. Smoothing functions were assigned such that they yield significant effect on the predictor variable while training the GAM model; yet, some other variables were added as they improved the prediction accuracy in the validation phase in terms of misclassification rate. The modeling and training of GAM were performed using software R, version 3.6.1.

ANN-based Pattern Recognition System

An ANN-based pattern recognition system was developed to adequately describe the complex relationship between the predictor variables and the binary response variable indicating the probability of stripping. A multilayered feed-forward neural network was selected with a logistic sigmoidal activation function (logsig) that produces output between 0 and 1. The ANN consisted of five layers (i.e., one input layer, two hidden layers, one probabilistic layer, and a target layer) as shown in Figure 38.

Figure 38. Neural network architecture

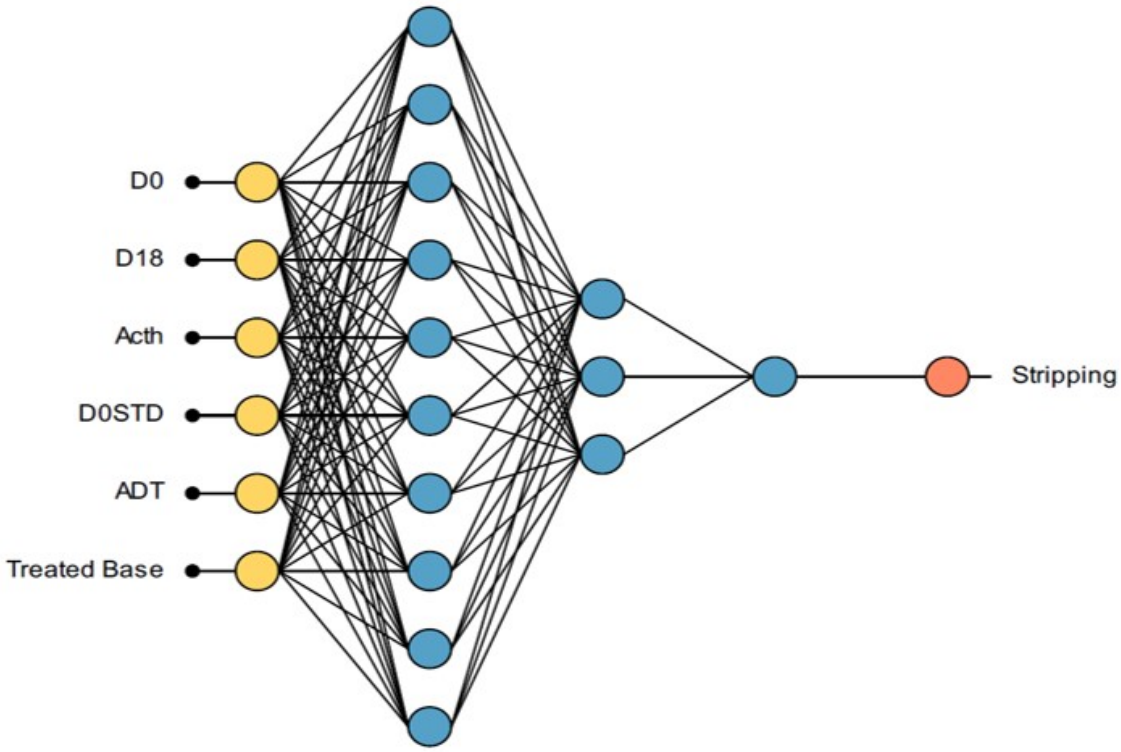

ANN Structure. The set of inputs were incorporated into the system such as it produces the highest classification accuracy. The input layer consisted of six neurons of input variables, which were subjected to a scaling method called "StandardDeviation" that normalizes the inputs. The input layer was fed with center deflection (D_0), deflection at 18 in. distance from center deflection (D_{18}), asphalt layer thickness (ACth), standard deviation of RWD measurements within 1-mile (D_0STD), annual daily traffic (ADT), and if a base is treated or not noted as Treated Base (1=if treated, 0=if not treated). The neural network had two hidden layers of 10 and 3 neurons, respectively, as shown in Figure 38.

A minimum number of hidden layers were selected through an iterative process that would not affect the network performance. The selection of the number of neurons within each hidden layer was conducted using an incremental order algorithm that increases the number of neuron with each iteration. The fourth layer of the neural network was a probabilistic layer that allows the outputs to be converted to probabilities (i.e., values between 0 and 1); it was followed by the target layer. The target layer consisted of two classes (i.e., 1=stripping, 0=no stripping).

Training Strategy. The neural network was trained using the Quasi-Newton method that uses gradient information to compute inverse Hessian at each iteration. The network error was calculated using a weighted squared error method that is useful for unbalanced class of dataset, which is the case with the dataset used in the study. A regularization method called "neural parameters norm" was applied to the network to reduce its complexity. About 70% of data were used for training, 15% of data were used for testing, and 15% data were used for validating the network.

Classification Tree. To assist in the identification of stripped sections, a classification tree was developed based on the given dataset. A classification tree uses a recursive binary splitting algorithm to grow a decision tree. This kind of decision tree is simple and convenient for the use of state agencies. It is assumed that decision trees closely reflect the human nature of decision-making unlike other regression and classification approaches. Furthermore, it has the capability of handling qualitative predictor variables without replacing them with a dummy variable *[75]*.

Unlike regression, the residual sum of squares (RSS) is not used for binary class splits; a classification tree approach rather uses classification-error-rate to grow the best decision-based tree. When an observation is assigned to a most occurring class, the classification error rate refers to the fraction of the observations that did not belong to the most occurring class. This study developed a classification tree such that the classification-error-rate is minimized for the given dataset; this analysis was conducted with iterative trials of the predictor variables.

Moisture Damage Detection using Ground Penetrating Radar

Simulation Study using gprMax. As an electromagnetic phenomenon, the transmission of GPR signals can be described by the well-known Maxwell's equations. The Finite-Difference Time-Domain (FDTD) method discretizes both the time and space continua

for numerical solution of Maxwell's equations. In this study, an FDTD-based open source program, gprMax *[76]*, was used to simulate the propagation of GPR signal in stripped pavement sections.

A 2D pavement model with stripping within the AC layer was constructed to simulate the pavement section with moisture damage (Figure 39). The pavement structure consisted of 101.6-mm thick AC layer, 203.2-mm thick base layer, and 101.6-mm long void section, where all the materials were assumed to be non-conductive and non-magnetic. Simulations were conducted by constructing voids in the middle and at the bottom of the AC layer for five void thicknesses (2 mm, 4 mm, 6 mm, 8 mm, and 10 mm). A perfectly matched layer (PML) boundary (as shown in Figure 39) is a type of absorbing boundary condition (ABC) that absorbs the wave and limits the computational space. The dielectric constants of AC, base, and air voids were assumed to be 5, 9, and 1, respectively. The transmitter (Tx) and Receiver (Rx) were placed 8 in. above the pavement surface. In order to simulate the GPR pulse used in field testing, the Ricker wavelet with center frequency of 1.6 Hz was used as the excitation source. The spatial resolutions in the vertical and horizontal direction were 2 mm. Equation (24) was used to calculate the time step (Δt) of each iteration as follows:

$$\Delta t \leq \frac{1}{c\sqrt{\frac{1}{(\Delta x)^2}+\frac{1}{(\Delta y)^2}}} \tag{24}$$

Where, Δx and Δy are the spatial resolution in the horizontal and vertical directions, respectively, and c is the speed of light in vacuum.

Figure 39. gprMax model of stripped asphalt pavement

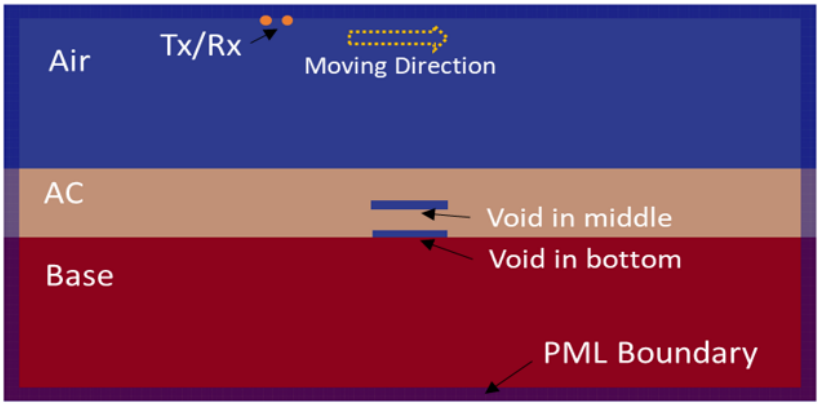

Figure 40 presents the A-scan results of the simulated GPR signal. The curves represent the reflection of the electromagnetic wave from the transmitter to the receiver. A negative peak was observed between two intermittent positive peaks when the EM waves were transmitted from a material with low dielectric constant to a material with high dielectric constant. In contrast, a positive peak appeared between two intermittent negative peaks when the EM waves were transmitted from a material with high dielectric constant to a material with low dielectric constant. In a regular non-stripped pavement, two positive peaks were observed in the reflected signal, where the first peak represents the reflected wave of air-AC interface and the second reflected peak represents the wave from the interface between AC and the base layers.

Theoretically, the strength of the reflected wave from the interface between the void and the base layer should be stronger than the reflection from the interface between the AC and base layer as the difference in dielectric constants between the void and the base layer is higher. However, the pavement with a 2-mm thick void showed lower reflection strength than the non-stripped pavement as indicated by the simulation results. This can be attributed to the overlapping of the signals from the two interfaces as they passed through the thin void layer. For the simulated pavement with a void at the bottom of the AC layer and a void thickness greater than 2 mm, a negative peak appeared between the two positive peaks, which represent the reflection from the interface between the void and AC layer. The strength of the second positive peak increased with the increase in void thickness due to the overlapping of the two reflections, see Figure 40.

For the simulated pavement section with a void in the middle of the AC layer, a positive peak appeared between the reflections from the surface and the interface between AC and base layers; the strength of the positive peak increased with the increase in void thickness; see Figure 40. It is noted that the strength of the reflected wave from the interface between AC and base layers decreased compared to the non-stripped pavement. This is due to the loss in energy of the EM wave as it passes through the void layer.

Figure 40. A-scan results of simulated GPR signal for (a) a void at bottom of the AC layer and (b) a void in middle of the AC layer

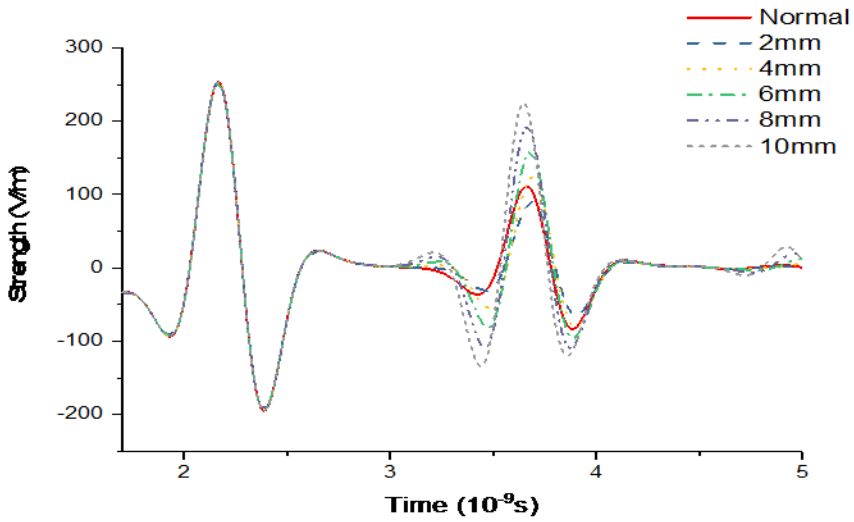

(a)

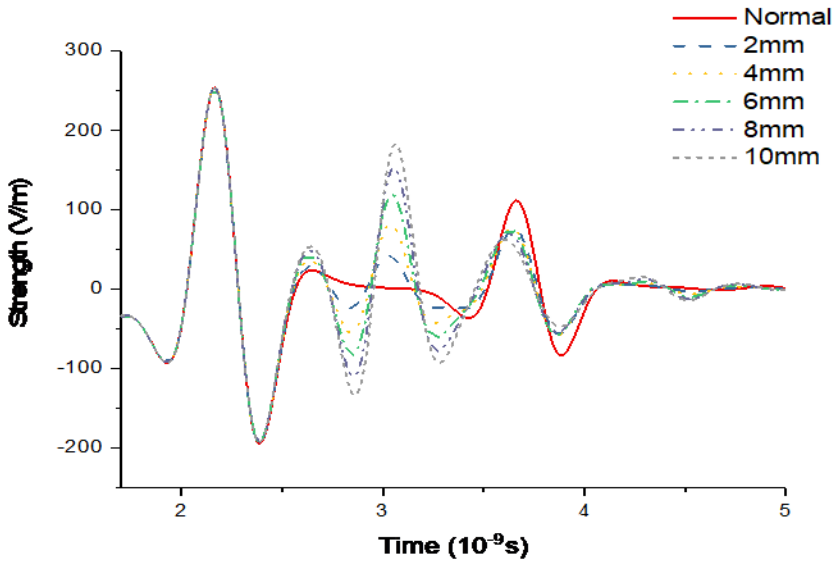

(b)

Figure 41 presents the results of the B-scan for the simulated pavement section with a 10-mm thick void and with stripping damage in the middle of the section. The x-axis represents the length of the road segment in the traffic direction. The deeper red zone in the interface between the AC and base layers (Figure 41 [a]) and the hyperbolic contour

within the AC layer (Figure 41 [b]) represent the moisture damaged area. For a normal non-stripped pavement, the first and second positive peaks (red belt in figure) are reflected from the surface and the interface between AC and base layers, respectively.

Figure 41. B-scan results of simulated GPR signal for (a) void at bottom of the AC layer, (b) void in middle of the AC layer

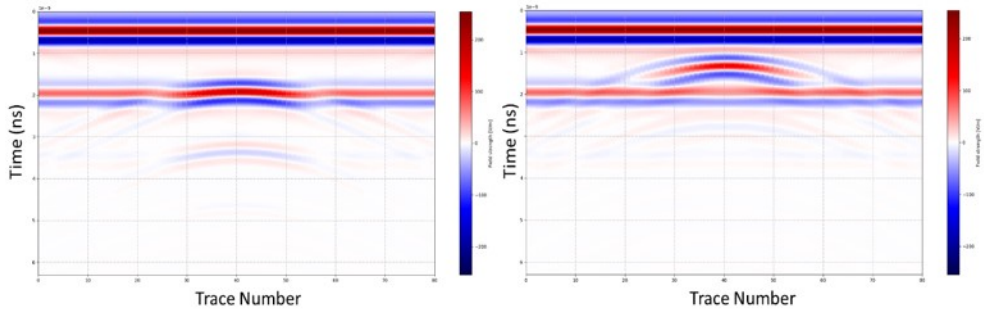

(a) (b)

Development of GPR Stripping Detection Approach

Field Testing Program. To evaluate GPR capabilities in detecting stripping damage in flexible pavements, a field-testing program was undertaken. Field data used in this study included cores samples and GPR scans collected by DOTD. GPR surveys were conducted on the entire length of the control sections in Louisiana. A GPR system manufactured by Geophysical Survey Systems, Inc. (GSSI) was utilized in the testing program to perform these surveys. Figure 42 shows the GPR testing setup. The equipment consisted of a control unit, monitor, and two dipole bowtie (ground and air-coupled) antennae operating at center frequencies of 900 MHz and 1.6 GHz. The setup can perform up to 16 scans per feet at 10 mph, which results in a scan at about every 1 inch. The data were collected at the posted speed with a maximum speed of 55 mph, although the speed varied based on traffic and vehicle stops. The GPR acquisition setup and configuration are summarized in Table 9.

Figure 42. Description of the GPR testing setup

Table 9. GPR acquisition setup

Antennas		GSSI Ground coupled	
Channel	-	1	2
Frequency	[MHz]	1600	900
Time window	[ns]	15	30
Samples/scan	-	256	256
Trace interval	[scan/m]	4	4
IIR (vertical high/low pass filter)	[MHz]	375/3000	225/1800

A survey encoder was used to connect the GPR device to a calibrated survey wheel that measures the traveling distance. A Global Positioning System (GPS) device was also used to track the locations of the survey lines. The GPS data were collected at 0.01-mile intervals along the road segment. The moving mode employed in this study allowed a radar wave to be transmitted, received, and recorded each time the antenna is moved a fixed distance across the pavement surface. The recorded signals are displayed as traces side-by-side to form a GPR time-distance record, or radargram, which shows how the reflections vary in the subsurface with distance.

DOTD also performed pavement coring for most of the road segments. At least one core sample was extracted from each road segment to verify pavement thicknesses and to identify any material deterioration below the pavement surface as well as bonding conditions. The core thicknesses were measured in accordance with ASTM D3549. In this study, core samples were visually inspected to determine whether stripping damage

was detected in each core location. The GPR data were analyzed and averaged at 0.003-mile nearest to the location of cores. Each core location included about 12 GPR scans.

Data Processing. The raw data were processed for surface position adjustment, time zero correction, and Infinite Impulse Response (IIR) and Finite Impulse Response (FIR) filtering before further analysis. A band-pass filter was used to remove high and low-frequency noises from the scans. The RADAN software was used to process and analyze the radargrams from the GPR data. Figure 43 shows a typical signal interpretation of B-scan results. When thousands of collected traces are stacked side by side, color-coded images help the users identify target features in the scan. The interactive interpolation module of the software offers query feature to acquire the location, time, and strength of peaks on the wave curve, then export the collected data for further processing.

Figure 43. Interactive interpretation of GPR data

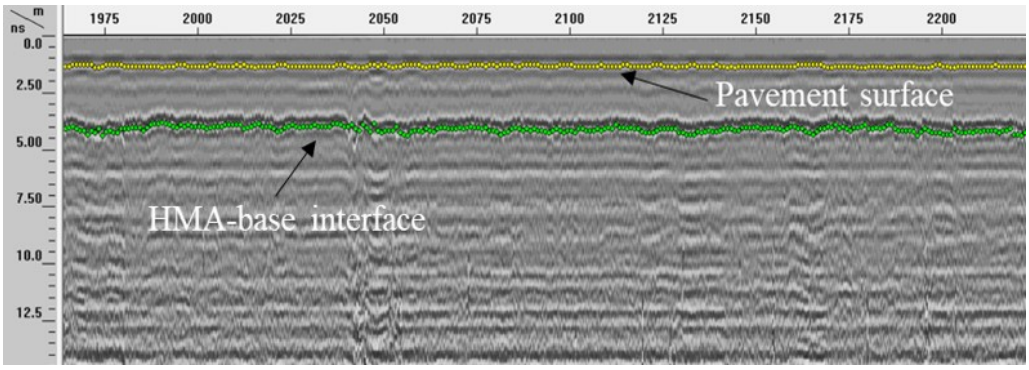

Example of GPR Data Analysis. As described earlier, the GPR data were processed for the core locations based on distance correlation. The pattern of GPR traces was studied and compared with the condition of the extracted cores at that location. Figure 44 presents the GPR traces at the stripped and non-stripped core locations for a control section located in Bienville parish in Louisiana. The pavement structure consisted of an AC layer, a PCC base layer, and a subgrade. The time range of the GPR traces covered the reflected waves from the pavement surface to the interface between the AC and base layers. The colored data points in the GPR trace represent the interfaces between the layers or the rebars in case of the reinforced concrete layer. As shown in the figure, in the non-stripped location, there were three positive peaks from top to bottom that correlated with the surface and layer interfaces. In the stripped section, intermittent positive peaks can be observed between the layer interfaces, which indicate loss of integrity within the AC layer.

Figure 44. Comparison of GPR traces for stripped and non-stripped sections and visual inspection of each core, (a) stripped section, (b) non-stripped section

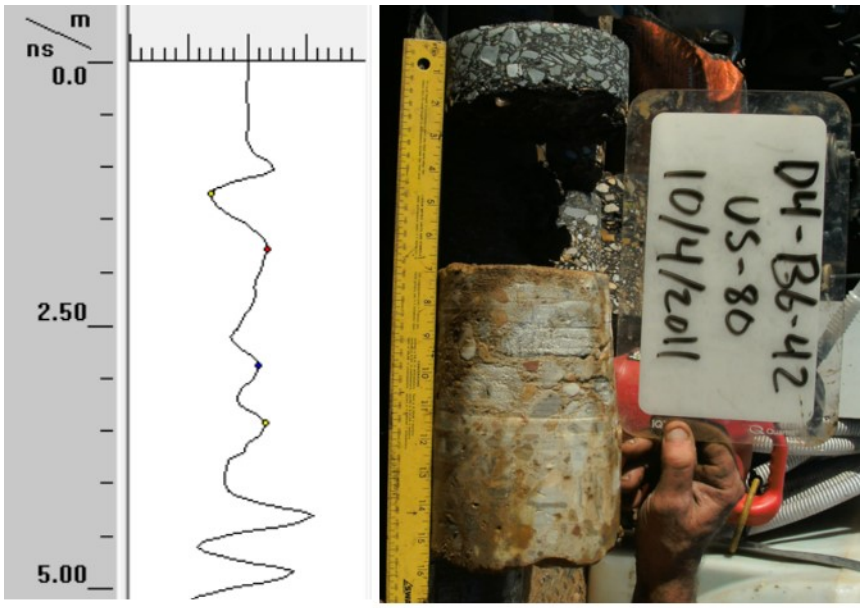

(a)

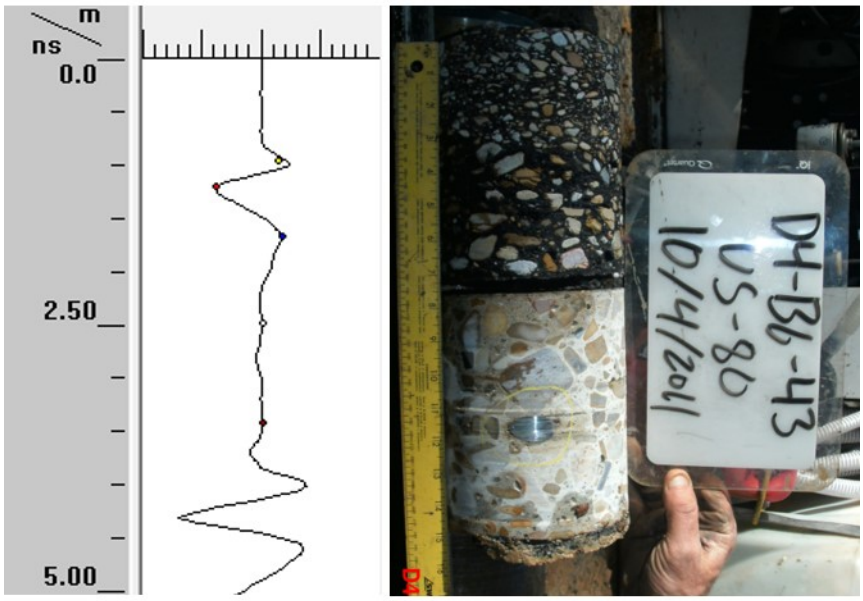

(b)

Accumulating In-Layer Peaks. As demonstrated in the previous section, AC stripping damage was found to be associated with the intermediate peaks of waves within the AC layer in the GPR trace. Based on this observation, a novel indicator, known as the Accumulating In-layer Peaks (AIP), was defined to evaluate the stripping potential in

asphalt pavements (Equation 25). As shown Equation (25), AIP is the ratio of the sum of in-layer positive amplitudes to the amplitude of surface reflection. Compared to the dielectric constant indicator that has been extensively used in previous studies, the AIP reflects the loss of integrity of the AC layer, which is associated with stripping damage. The AIP is also able to quantitatively evaluate the stripping damage. A greater value of AIP indicates a greater potential for AC stripping damage.

$$AIP = \sum_{i=1}^{n} A_i \Big/ A_0 \tag{25}$$

Where, A_i is the amplitude of positive peaks within the AC layer, and A_0 is the amplitude of peak reflected from the surface.

Pavement Sections Selection and AIP Computation. The Louisiana PMS was used to identify the pavement control sections related to the ARAN file names (GPR file with .DZT extension used in the analysis) using the district, parish, route, and direction information in the original GPR data file. The pavement control sections and DZT files were first sub-grouped based on the location such that each related group set are on the same parish, route, and direction. The DZT files were then considered for the analysis only if:

- The number of control sections in a route were the same as the number of DZT files for that route, and
- The difference between the length of the control section and length of the DZT file did not exceed 0.2 mile.

The interactive interpolation tool in the RADAN software was used to trace the surface, in layer peaks, and the interface between asphalt and base layer as shown in Figure 45. While a wide range of color combinations are available in the software, a color combination of red and blue (Color Table of 25 and Color XForm of 1 in the software) was used in the analysis where red indicates a strong positive reflection and blue indicates a strong negative reflection.

Figure 45. GPR traces of surface, in-layer noises, and asphalt-base interface for control section 112-07-1 (LA0174, Red River Parish)

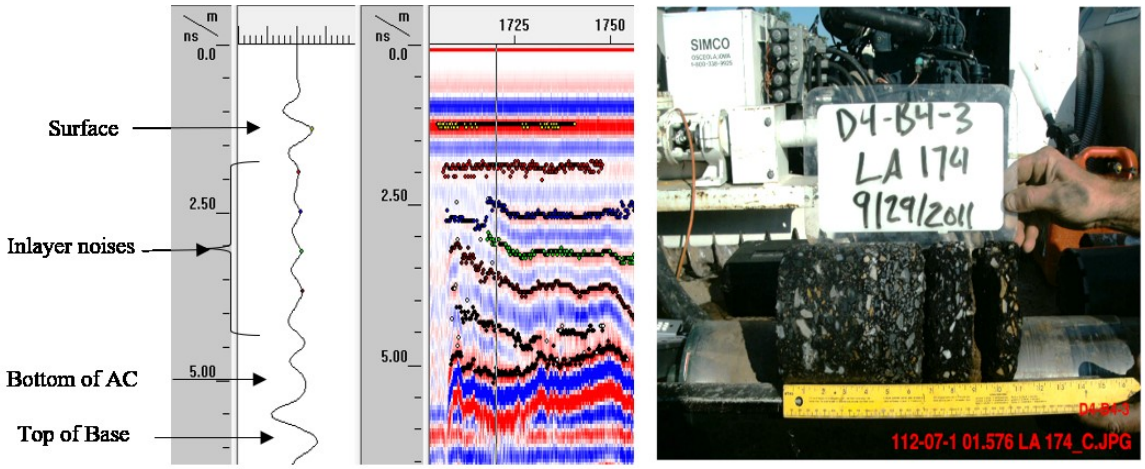

The location of the core in the GPR scan was identified using the control section log mile (CSLM) information in the core report. The CSLM was multiplied by 1000 and was added to the beginning of the GPR scan for the sections cored in the primary direction while the thousandth of the CSLM was subtracted from the end of the GPR scan for the sections cored in the secondary direction to accurately locate the core location. Layer traces were then color-coded using the EZ tracker picking tool in the software for enhanced visual interpretation of the scans. The resulting layer file was exported to Microsoft Excel to compute the amplitudes of the traced layers. The amplitudes of the surface and in layer peaks were averaged at 0.003-mile nearest to the location of cores. The AIP was then computed using Equation (25). Figure 46 presents examples of GPR traces for stripped and non-stripped cores.

Figure 46. GPR traces for stripped sections (a) 065-07-1, (b) 256-03-1, and non-stripped sections (c) 001-06-1, and (d) 010-02-1

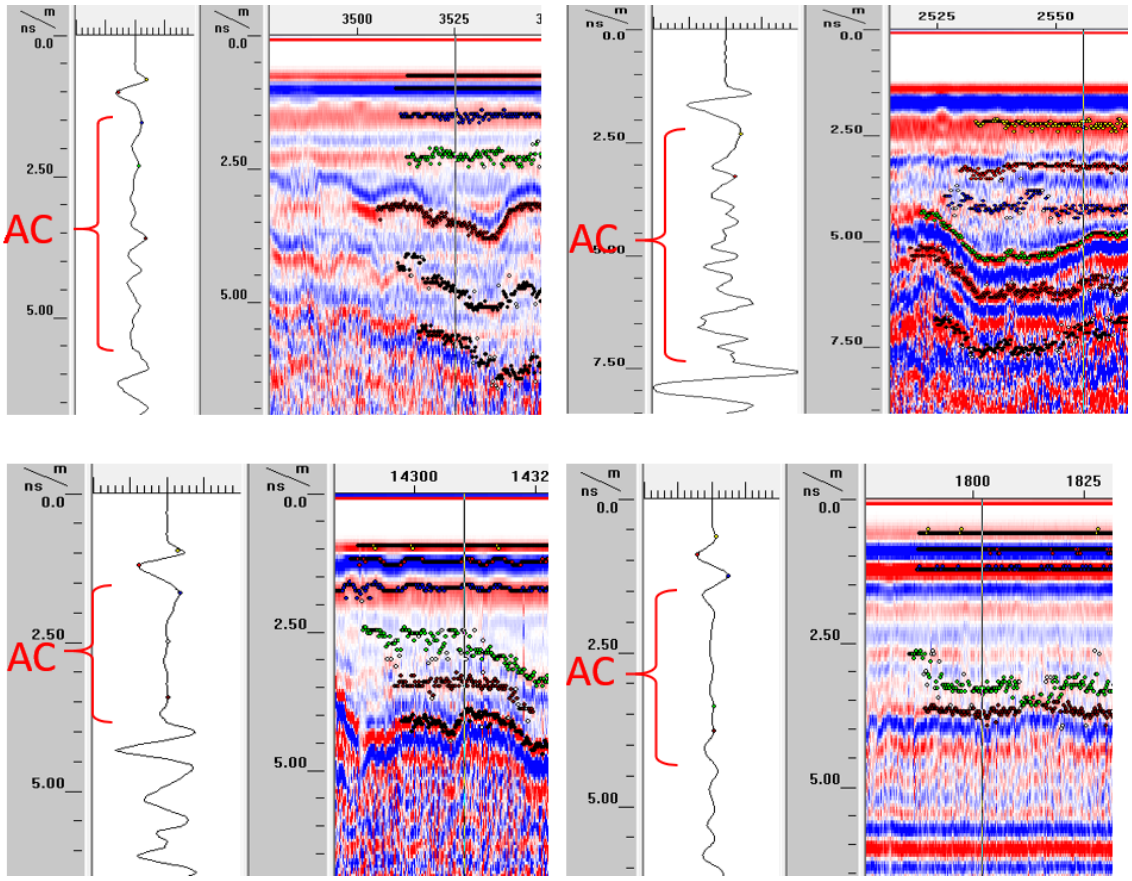

As shown in Figure 46, the stripped sections contained relatively higher levels of layer noises compared to the non-stripped sections. Figure 47 presents an illustration of amplitudes computation for a stripped pavement section (112-07-1). An AIP of 1.48 was calculated for the section presented in Figure 47.

Figure 47. Amplitude of surface and in-layer noises for control section 112-07-1

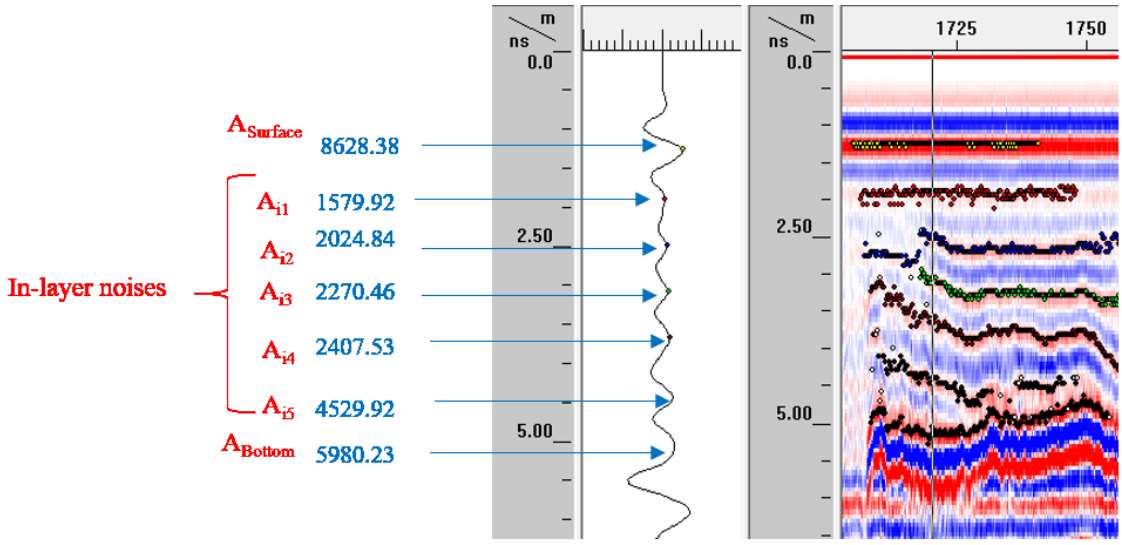

Control Section 112-07-1, LA0174, Red River Parish

Effect of Moisture Damage on the Performance and Cost-Effectiveness of Chip Seal and Overlay

Figure 48 illustrates the general outlines of the research methodology for this task. Chip sealed and AC overlay road sections were identified from the DOTD PMS. For these sections, core reports were then reviewed and analyzed to identify the occurrence of moisture-induced damage in the underlying AC layers before applying chip seal or an AC overlay. Distress and roughness data were then obtained from the PMS and Pavement Condition Index (PCI) values were calculated. Performance curves, which were fitted to the PMS data, were then used to calculate four field performance indicators, which were the average deterioration rate (ADR), extension in pavement service life (ΔPSL), average condition increase over the treatment service life (PI), and cost-effectiveness (CE). The last step consisted of conducting a statistical analysis to evaluate the effects of moisture-induced damage on the long-term pavement performance and cost-effectiveness of chip seal and AC overlays.

Figure 48. General outlines of the research methodology

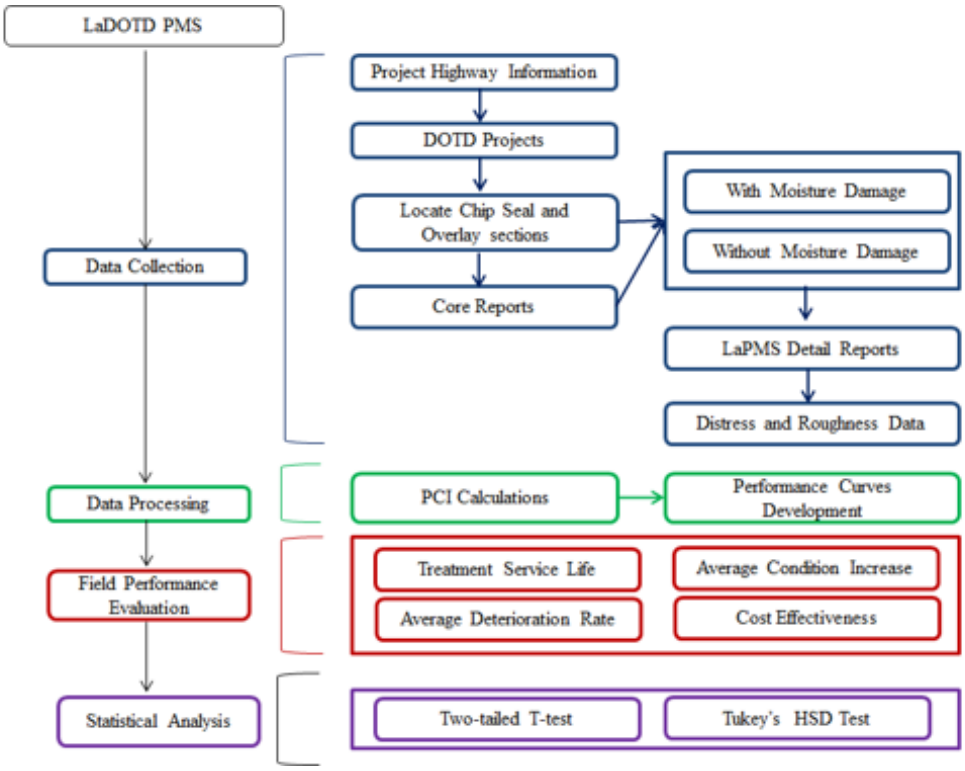

Data Collection

Data from approximately 496 miles of Louisiana roads were used in the present analysis. For chip seal sections, data from 228 miles were used in the analysis. Based on core reports, 160 miles were identified as non-stripped chip-sealed sections while the remaining 68 miles were classified as stripped sections (i.e., with moisture damage) (see Figure 49). Similarly, among 268 miles of AC overlay sections, 117 miles were stripped sections and about 151 miles were non-stripped sections. Distress and roughness data were obtained from the DOTD PMS inventory. As previously noted, pavement condition measurements are regularly conducted in Louisiana biennially using the Automatic Road Analyzer (ARAN) vehicle, which provides a continuous evaluation of the road network. DOTD PMS reports the collected data for each 0.1 of a mile. Data for each log-mile were used to calculate PCI values, which in turn were used to calculate the different performance indicators selected in the analysis.

Figure 49. Examples of core data extracted by DOTD

(a) Non-stripped pavement (b) Stripped pavement

Data Processing

The condition of the existing pavement sections was evaluated based on the PCI since it accurately reflects pavement surface conditions over time. In addition, many agencies throughout the United States and Canada use it to monitor the performance of the road sections and their level of service *[77]*. In Louisiana, PCI is typically calculated as a function of different DOTD indices as presented in Equation (26) *[78]*. Based on the calculated PCI, a regression curve describing pavement performance before and after the treatment was fitted for each pavement section, as illustrated in Figure 50.

$$\mathrm{PCI} = \mathrm{MAX}\{\mathrm{MIN}(\mathrm{RCI}, \mathrm{ALCR}, \mathrm{PTCH}, \mathrm{RFI}, \mathrm{RTI}) \times \mathrm{AVG}(\mathrm{RCI}, \mathrm{ALCR}, \mathrm{PTCH}, \mathrm{RFI}, \mathrm{RTI}) - 0.85\ \mathrm{SD}(\mathrm{RCI}, \mathrm{ALCR}, \mathrm{PTCH}, \mathrm{RFI}, \mathrm{RTI}) \quad (26)$$

Where, RCI = the random cracks index; ALCR = alligator cracking index; PTCH = patch index; RFI = roughness index; RTI = rutting index; and SD = standard deviation.

Figure 50. Modeling of pavement performance from PMS data

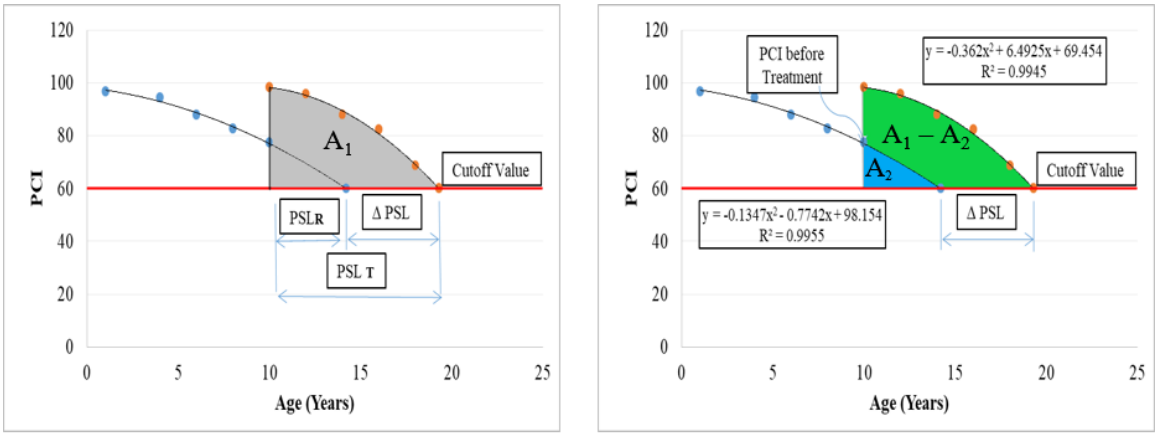

(a) Extension in pavement service life

(b) Cost-effectiveness

Performance Indicators

The present study selected four performance indicators to compare the long-term performance of stripped and non-stripped sections after the application of chip seals and AC overlays. These indicators are classified into two categories: benefits-only approaches and benefit-cost approaches. The benefit-only approach included the average deterioration rate (ADR), the extension in pavement service life (ΔPSL), and the average increase in pavement condition (PI %). Treatment cost-effectiveness (CE %) was used as a benefit-cost indicator in the current analysis. A description of these indicators is provided in the following sections.

Average Deterioration Rate. The ADR was compared for the stripped and non-stripped pavement sections. The deterioration rate between two successive survey cycles was calculated using Equation (27). ADR was then calculated based on Equation (28).

$$DRi+1\ (\%) = \frac{PCI_i - PCI_{i+1}}{Y_{i+1} - Y_i} * 100 \quad (27)$$

Where, DR_i = the deterioration rate (%) in the year of (i+1) years of the treatment age, PCI_i = PCI value at the year of (i) after applying the treatment, PCI_{i+1} = PCI value at the year of (i+1) after applying the treatment, Y_i = treatment age at PCI value of PCI $_I$, and Y_{i+1} = treatment age at PCI value of PCI $_{i+1}$.

$$ADR\ (\%) = \frac{\sum_{i=1}^{n} DR_i}{n} \quad (28)$$

where, n = the number of surveys.

Extension in Pavement Service Life (ΔPSL). Pavement service life (PSL) is defined as the age at which a given pavement condition (i.e., PCI or IRI) reaches a selected threshold value *[79]*. Based on this definition, PSL can be calculated by extrapolating the pavement performance curve to a point at which pavement conditions reach a pre-determined threshold. ΔPSL calculation involved numerous steps. First, performance curves were fitted between PCI values and pavement age (years) (see Figure 50). As shown in Figure 50(a), the remaining PSL (PSL_R) of the pavement before the treatment was calculated by extrapolating the performance curve before the treatment to the selected threshold value. Similarly, the treatment PSL (PSL_T) was computed by extrapolating the performance curve after the treatment until it reached the threshold value. Finally, ΔPSL was calculated by subtracting PSL_R from PSL_T considering a PCI threshold value of 60 as suggested by DOTD PMS *[80]*.

Average Condition Increase (PI %). In the present analysis, the increase in average pavement condition over chip seal or AC overlay service life relative to the condition of the road before the treatment (PCI^-) was used to evaluate the effect of moisture damage on chip seal and AC overlay performance. Equation (29) was used to calculate PI *[81, 82]*. It can be noted from Equation (29), the higher the PI value, the better the long-term performance of a treatment is.

$$PI\ (\%) = \frac{PCI_{avg} - PCI^-}{PCI^-} * 100 \quad (29)$$

$$PCI_{avg} = \frac{\sum_{i=1}^{n} 0.5*(PCI_i + PCI_{i+1})*\Delta Y}{Y_n - Y_1} \quad (30)$$

Where, PCI_{avg} = average PCI value over the treatment service life, PCI_i = PCI value at the time of I, ΔY = the period between i and i+1, Y_1 = the year when chip seals or AC overlays were placed, Y_n = the last measurement year, and PCI^- = PCI value before treatment.

Cost-Effectiveness. Cost-Effectiveness (CE) analysis typically compares the relative efficiency of several alternatives from a budgetary perspective to help decision-makers select the optimum alternative. However, in the current study, CE analysis was used to evaluate the effect of moisture-induced damage on the cost efficiency of chip seal and AC overlay treatments. The CE of a treatment strategy for a road section was calculated using Equation (31):

$$CE\ (\%) = \frac{A_1 - A_2}{\text{Unit Cost (\$)}} * 100 \quad (31)$$

Where, A_1 = an area that represents the benefits of a given treatment (see Figure 50(a)) until reaching a cutoff value; A_2 = an area that represents the remaining benefits of the existing pavement (see Figure 50(b)) until reaching the same cutoff value; A_1-A_2 = an area, which indicates the net benefits of treatment application; see Figure 50(b); and Unit Cost ($) = unit cost of the treatment, which was obtained from DOTD database.

Data Analysis Strategy

Figure 51 presents the data analysis strategy adopted in the study. For chip seal and AC overlay sections, traffic volume and pre-treatment conditions (PCI^-) were used to classify the road sections into groups. In terms of traffic volume, pavement sections were categorized into two groups as sections with low traffic levels (ADT <1,100 vpd) and medium traffic levels (1,100 <ADT < 5,300 vpd) (see Figure 51(a)). In addition, pre-treatment conditions (PCI^- values) were used to classify pavement sections as sections with PCI^-< 80 and PCI^- > 80, as shown in Figure 51(b). Pavement sections in each group were then categorized into two different sub-groups based on the presence of moisture damage before treatment (i.e., stripped and non-stripped sections). The performances of the road sections were then compared statistically for the defined subsets to assess the statistical significance of moisture-induced damage on the observed field performance. It is worth noting that for AC overlays, the majority of the road sections had pre-treatment conditions (PCI^-) ranging from 65 to 70, which hindered the feasibility to assess the effect of this factor on the performance of the AC overlays. Therefore, the effects of moisture-induced damage on AC overlays were evaluated only for different traffic levels.

Figure 51. Analysis procedure for chip-sealed and AC overlay sections

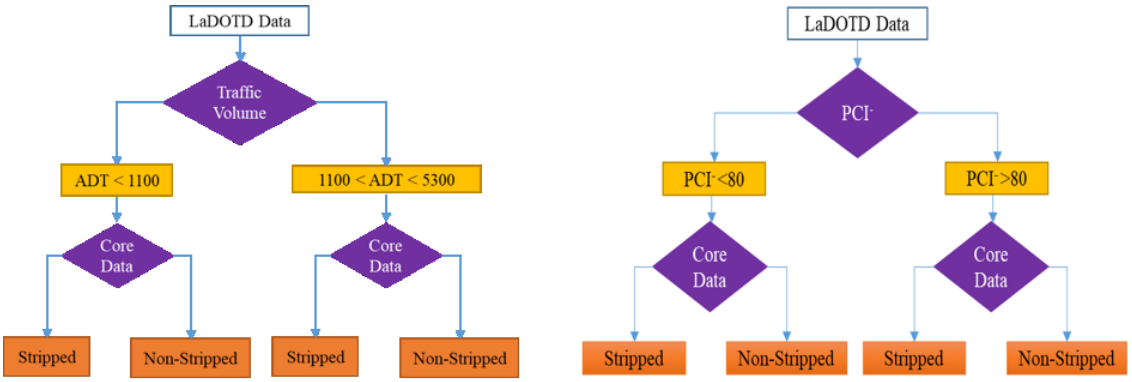

(a) Analysis based on traffic volume (b) Analysis based on pre-treatment conditions

Prediction of Pavement Roughness Conditions Using Surface Images

Figure 52 demonstrates the general outlines of the research methodology for this task. In-service pavement sections were selected from the DOTD PMS databases. For this task, digital images and quantitative distress data were extracted. On one hand, 3D pavement images were acquired from the iVision application available in the DOTD PMS inventory. The images from the different sections were then labeled based on their IRI values as "VG," "G," "F," and "P" sections, as shown in Table 10. The labeled images were then utilized to train and to validate a pre-existing CNN model for pavement roughness evaluation. On the other hand, the surface quantitative distress data were extracted from the PMS and the DOTD indices were calculated. Sections were clustered into different groups based on their roughness conditions (see Table 10). The effectiveness of an ANN-based and a MNL-based models to classify the sections into different pavement roughness conditions using only DOTD indices as independent variables was investigated.

Table 10. IRI threshold for different IRI categories *[11]*

IRI Rating		IRI Range (in./mile)
1	Very Good (VG)	<90
2	Good (G)	90-180
3	Fair (F)	180-258
4	Poor (P)	>258

Figure 52. The general outlines of the research methodology

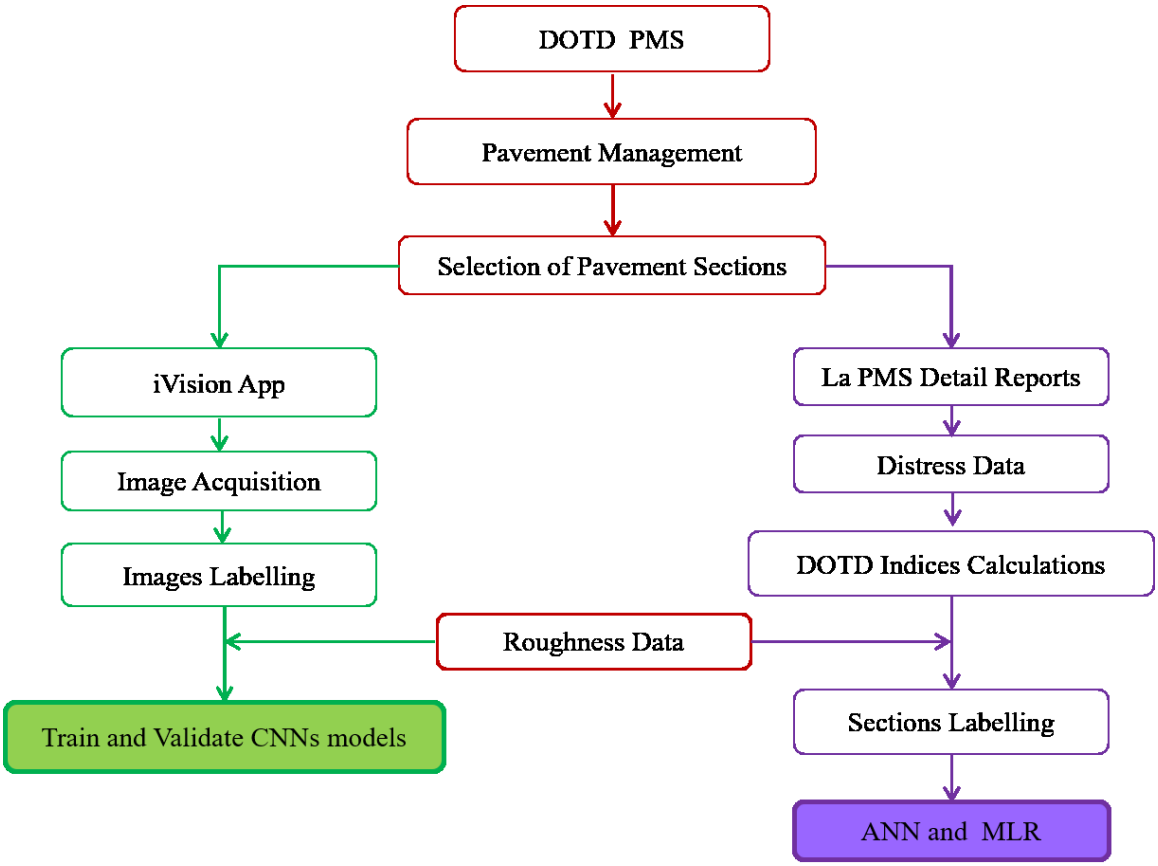

Data Collection and Categorization

As previously noted, pavement sections in Louisiana are surveyed every two years using the ARAN system, which collects high definition pavement images for continuous assessment of the road network. In this assessment, pavement sections are divided into segments with a length of 0.10 mile. For each 0.10 mile, ARAN captures twenty-five 3D images meaning that each image covers 0.004 mile of the road length, which provides a detailed assessment of pavement surface conditions. The DOTD PMS was used to extract 850 3D pavement images and their corresponding IRI values for 34 road sections. The pavement sections were selected to cover a wide range of traffic levels and different pavement surface conditions. As presented in Table 11, the IRI values of the selected pavement sections ranged from 50 in./mile to 342 in./mile to cover all roughness conditions. With respect to the quantitative data, 1,142 measurements were extracted from 114 miles of Louisiana roads and were used to develop the ANN and MNL models. These data included roughness and distress condition data.

Table 11. Images data description for the development of the CNN model

Group	No. of sections	Average IRI value for each section (in./mile)	ADT[1]		No. of images
			Min.	Max.	
VG	8	50, 58, 62, 65, 74, 75, 80, and 88	1,440	14,000	200
G	7	96, 104, 119, 126, 136, 144, and 158	860	15,100	175
F	11	181, 186, 192, 199, 207, 212, 220, 228, 236, 244, and 256	860	12,900	275
P	8	261, 267, 277, 285, 293, 302, 322, and 342	570	16,800	200
Total	34				850

[1] ADT: Average Daily Traffic

DOTD Indices

For the ANN-based and MNL-based models, DOTD indices were the main inputs used in the developed models. Distress data extracted from the DOTD PMS inventory were used to calculate the rut index (RTI), random cracking index (RCI), alligator cracking index (ALCR), and patching index (PTCH) using Equations (32), (33), (34), and (35), respectively *[83]*.

RTI = Min (100,100-((R_AVG*(10/0.125))-10)) (32)

Where, R_AVG = average rutting (in.).

RCI = Min (100, Max (0, 100-RCI_L DEDUCT - RCI_M DEDUCT- RCI _H DEDUCT)) (33)

Where, RCI_L DEDUCT, RCI_M DEDUCT, and RCI _H DEDUCT = the deduct points due to low, medium, and high severity random cracks.

ALCR = Min (100, Max (0, 100-ALCR_LDEDUCT-ALCR_MDEDUCT -ALCR_HDEDUCT)) (34)

Where, ALCR_LDEDUCT, ALCR_MDEDUCT, and ALCR_HDEDUCT = the deduct points due to low, medium, and high severity fatigue cracks.

PTCH = Min (100, Max (0, 100-PTCH_L DEDUCT-PTCH_M DEDUCT -PTCH_H DEDUCT)) (35)

Where, PTCH_L DEDUCT, PTCH_M DEDUCT, and PTCH_H DEDUCT = the deduct points due to low, medium, and high severity patching.

CNN Classification Model

The present analysis developed a CNN model to classify road sections into different roughness categories and to estimate the IRI values for road sections based on 3D pavement images. A pre-existing CNN model known as AlexNet was used in the analysis *[84]*. AlexNet was developed based on a massive database containing 1.2 million images. AlexNet was selected since it was expected to be effective in capturing both surface distresses and other irregularities that affect pavement roughness. Therefore, accurate predictions of pavement roughness may be achieved. Figure 53 presents the architecture of the AlexNet model.

Figure 53. AlexNet architecture

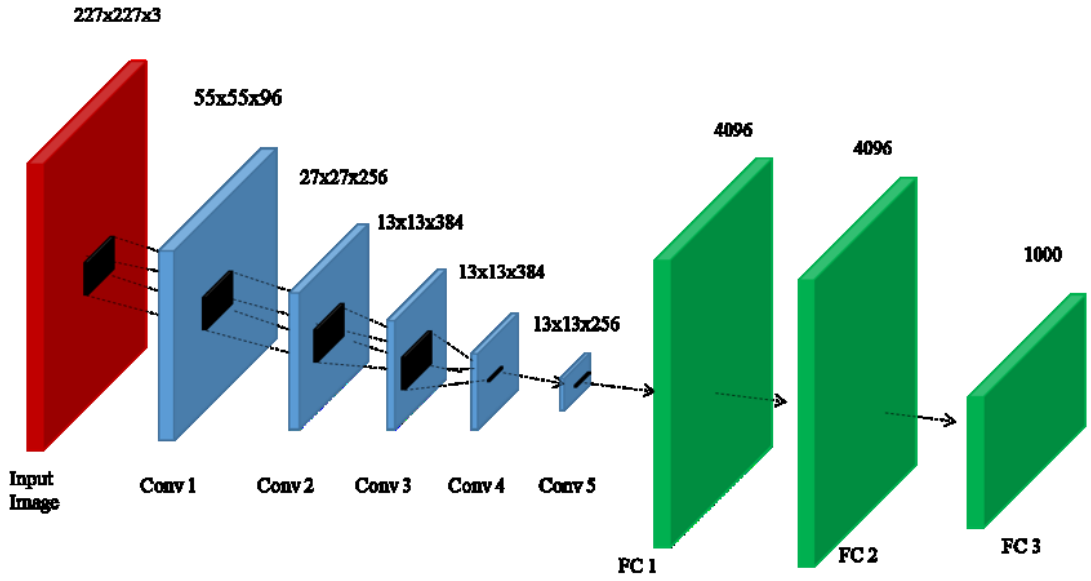

AlexNet Architecture. As shown in Figure 53, the adopted AlexNet architecture consisted of eight layers, five convolutional layers, and three fully connected layers. The last fully connected layer is connected to a softmax layer for the final classification. The first convolutional layer scans the input patch (224x224) with kernels of size 11x11 and a stride of 4x4. The second convolutional layer applies a 5x5 filter and the remaining convolutional layers were equipped with a kernel of 3x3 and a stride of one. The max

pooling was performed in a filter size of 3x3 with a stride of two. Finally, the fully connected layer consists of 4,096 neurons. The CNN use the rectified linear units (ReLU) as activation function after each convolution layer and fully connected layer instead of the traditional sigmoid function. The training time of CNN with ReLUs is six times faster than the CNN with the sigmoidal activation functions *[85]*. The data processing, CNN training, testing, and validation were performed in MATLAB 2018b platform in a computer with Intel Core i5-8265U CPU and 8GB of RAM.

ANN-Based Pattern Recognition Model

Pattern recognition is one of the most promising applications of artificial intelligence. Pattern recognition is the scientific discipline that uses prior knowledge or statistical information to build a classification tool that helps in the classification of objects into different categories *[86]*. Speech recognition, fingerprint identification, handwriting recognition, and seismic analysis are the general applications of pattern recognition. In the field of transportation, pattern recognition was utilized in different applications. For instance, Elbagalati et al. developed a pattern recognition system to select the optimum maintenance and rehabilitation decisions at the network-level *[87]*.

ANN Architecture for Pattern Recognition. Pattern recognition can be applied by using a multilayered feed-forward ANN with a Hard-Lim transfer function. The Hard-Lim function returns an output of zero or one. The final output would be “1” if specific thresholds were achieved; otherwise, the final output would be “0.” In the present study, an ANN-based pattern-recognition classification tool was developed to classify the pavement sections into different roughness groups. The ANN consisted of three layers: a four-neuron input layer, a twenty–neuron hidden layer, and a four-neuron output layer as shown in Figure 54(a).

Inputs and Target Variables. As shown in Figure 54(b), the input set consisted of four DOTD indices, which are related to pavement surface conditions; namely, RTI, RCI, ALCR, and PTCH. On the other hand, the roughness category, as presented in Table 10, was the final output. A twenty-neuron hidden layer was used to establish adequate correlations between the inputs and target outputs.

Figure 54. (a) Scheme of the components of the ANN model and (b) ANN's inputs and outputs

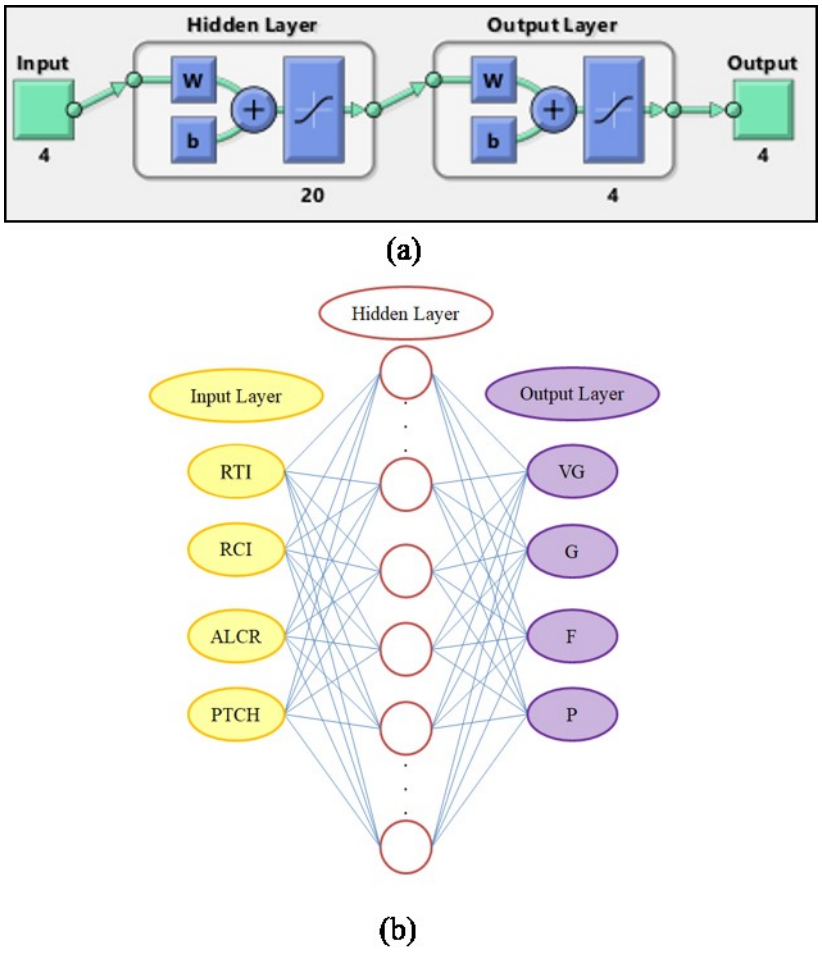

Logistic Regression Classification Model

Logistic regression is one of the most powerful tools that has been used in biological sciences since the beginning of the twentieth century *[88, 89]*. Logistic regression is a predictive analysis that can be only conducted when the dependent variables (outputs or target) are categorical or dichotomous. Logistic regression can be used to describe and test the relationship between the dependent variables and each independent variable (predictor) *[88, 89]*. However, the focus of the logistic regression is the classification of the individuals (observations) into different groups *[89]*. In the present application, either the output can be a binary (binomial) logistic regression or a multinomial logistic regression based on the number of dependent variables.

Binary Logistic Models. Logistic regression defines the relationship between the dependent and independent variables in terms of the natural logarithm of a likelihood ratio. Mathematically, binary logistic regression estimates a multiple linear regression function as defined by Equation (36):

$$\text{Logit (PA)} = \text{Ln}\left(\frac{P_A}{1-P_A}\right) = \text{Ln}\left(\frac{P_A}{P_B}\right) = \alpha + \beta_1 X_1 + \beta_2 X_2 + \beta_3 X_3 + \cdots + \beta_n X_n \quad (36)$$

Where, P_A = the probability of an observation to be assigned to the category "A," α = the Y-intercept, and β_n = regression coefficients of the predictor variables X_n.

Multinomial Logistic Models. The MNL was used to develop models, which are capable of classifying the observations into more than two categories (i.e., A, B, and C) *[90, 91]*. Equations (37) and (38) present the mathematical representation of the MNL for a multiple linear regression function. It is worth noting that category C was selected as the reference to calculate the probabilities of A and B.

$$\text{Ln}\left(\frac{P_A}{P_C}\right) = \alpha_1 + \beta_{11} X_1 + \beta_{12} X_2 + \beta_{13} X_3 + \cdots + \beta_{1n} X_n \quad (37)$$

$$\text{Ln}\left(\frac{P_B}{P_C}\right) = \alpha_2 + \beta_{21} X_1 + \beta_{22} X_2 + \beta_{23} X_3 + \cdots + \beta_{2n} X_n \quad (38)$$

The current analysis developed a MNL model to classify the pavement sections with different characteristics (RTI, RCI, ALCR, and PTCH) as the independent variables into different groups of roughness conditions as the dependent variable. Statistical Package for Social Sciences (SPSS) software was used to develop the logistic model by producing $\alpha_i$and β_{ij} in Equations (37 and 38), to assess the significance of each predictor to the dependent variables, and to evaluate the classification ability of the developed models.

Discussion of Results

Pavement Cracks Classification Using Machine Learning

CNN Network Performance

The data processing, CNN training, testing, and validation were performed in MATLAB 2019a platform in a computer with Intel Core i5-4590S microprocessor and 8GB of RAM. A data set consisting of 200 2D pavement images of size about 2500 x 4000 and 150 3D images of size about 1030 x 1610 were collected from the DOTD PMS database. These images were pre-processed using an automated preprocessing tool according to the aforementioned image processing techniques. The data were then divided into 60% for training, 15% for testing, and 25% for validation. The accuracy of the model was expressed in form of confusion matrices, which present the actual and predicted crack types in terms of numbers and percentages.

The developed CNN model was trained, tested, and validated for two data sets: a data set consisting of 2D images only and a data set consisting of both 2D and 3D images. Figure 55 presents the accuracy of CNN model for the raw pavement images. As shown in Figure 55, the model achieved an accuracy of 61.7% and 73.4% on the testing and validation phases, respectively. The low model accuracy for raw images is due to different factors such as pavement noise, background illumination, pavement marking, spots and stains including cracking patterns. The pavement images in the two data sets were then processed according to the aforementioned image processing techniques. For the data set consisting of 2D images only, the developed network achieved an overall accuracy of 88.9% and 86.7% in the testing and validation phases, respectively. Figure 56 presents the confusion matrices in the testing and validation phases. Similarly, for the data set consisting of a combination of 2D and 3D images, the developed model achieved an overall accuracy of 93.8%, and 91% respectively as illustrated in Figure 57.

Figure 55. Confusion matrices for raw pavement images for (a) testing, (b) validation for CNN model

(a)

(b)

Figure 56. Confusion matrices for 2D images for (a) testing, (b) validation for CNN model

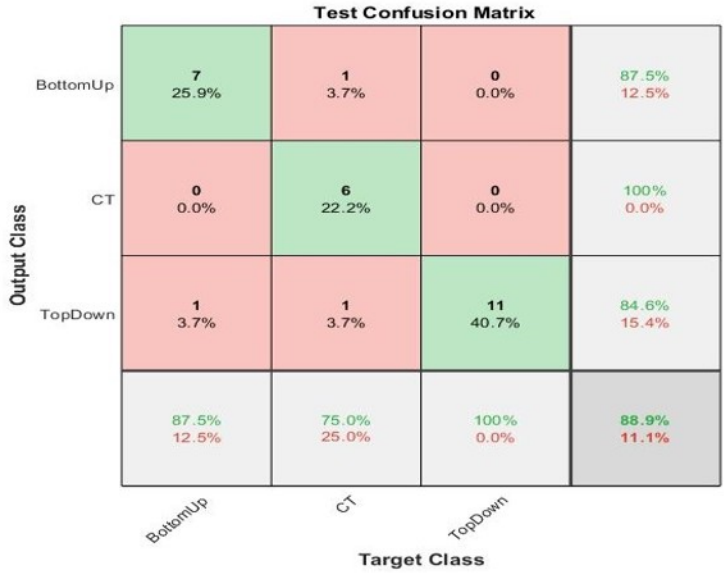

(a)

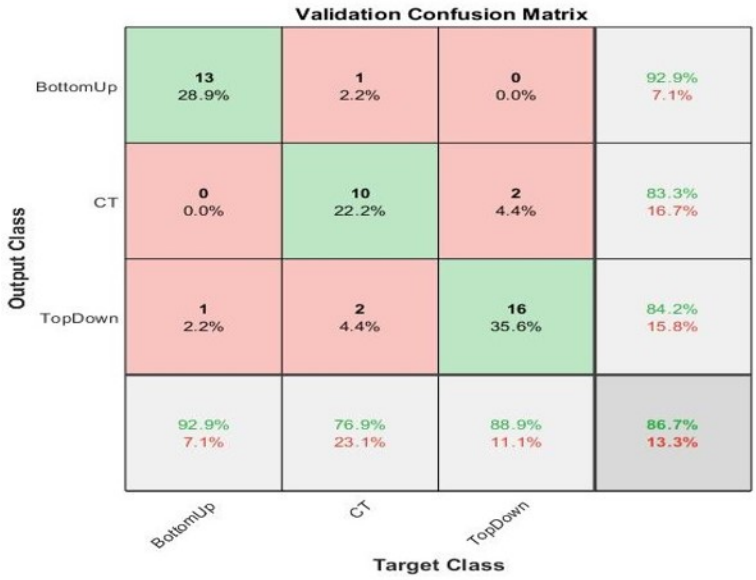

(b)

Figure 57. Confusion matrices for 2D and 3D images for (a) testing, (b) validation for CNN model

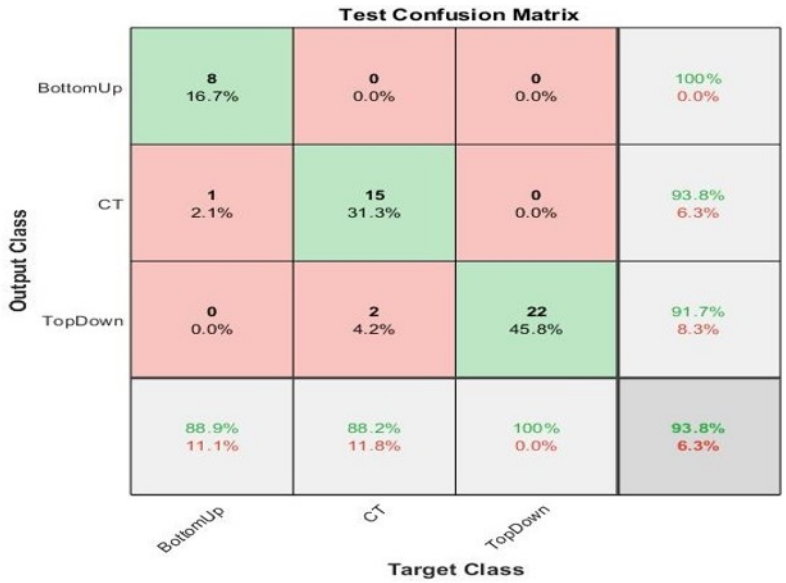

(a)

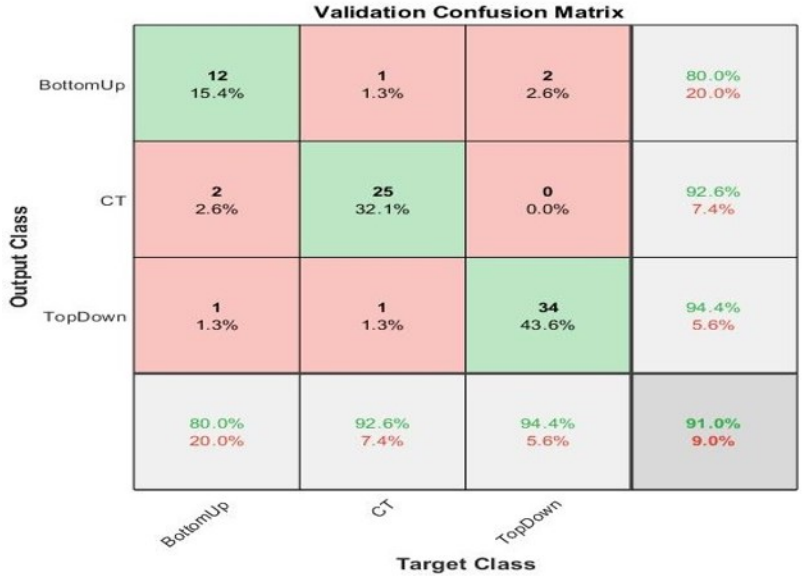

(b)

The dropout layers after the first two fully connected layers reduced the data overfitting by preventing complex co-adaptations during network training. The dropout layer randomly ignores some hidden and visible neurons during training and prevents the co-dependency amongst the neurons. However, the dropout layer requires additional computational expense for model training. In order to enhance the convergence and

calculation speed, the ReLU layers were connected to the convolutional and fully-connected layers. The ReLU layers implements the activation function and determines the output of the neural network. The output of ReLU layers was generalized using the LRN, which implements the lateral inhibition in order to reduce the capacity of a neuron that impedes the activity of its neighbors.

ANN Training and Performance

A computational tool available in MATLAB 2019a was used to process all the data and to develop the ANN decision-making tool. The input data corresponding to 150 pavement images used in the ANN model were collected from the Louisiana PMS. The data were then divided into 70%, 15%, and 15% for training, validation, and testing, respectively. Data overfitting was avoided by halting the training process when the validation set error stopped decreasing. The testing data were used to provide independent measure of the network performance as it had no effect on the training. Figure 58 presents the confusion matrices for training, validation, testing, and overall step for the pattern recognition system. As shown in the figure, the ANN tool achieved an accuracy of 91.3% in the testing and validation sets. The confusion matrices showed an overall prediction accuracy of 92% indicating the effectiveness of the ANN model to predict the correct crack types in the evaluation process.

The generalization ability of the overall network was enhanced and overfitting was avoided by halting the training as there was no observed decrease in the validation set error as shown in Figure 59. The matrices present N_{ij} with corresponding percentage, precision of every decision, and overall accuracy. The testing data set was used to provide an independent measure of the network performance. The network training time was found to be 4.2 seconds.

Figure 58. Confusion matrices for the pattern recognition system for training, validation, and testing for ANN model

Where, 1 = bottom up cracking, 2 = cement treated reflective cracking, and 3 = top down cracking

Figure 59. ANN model performance

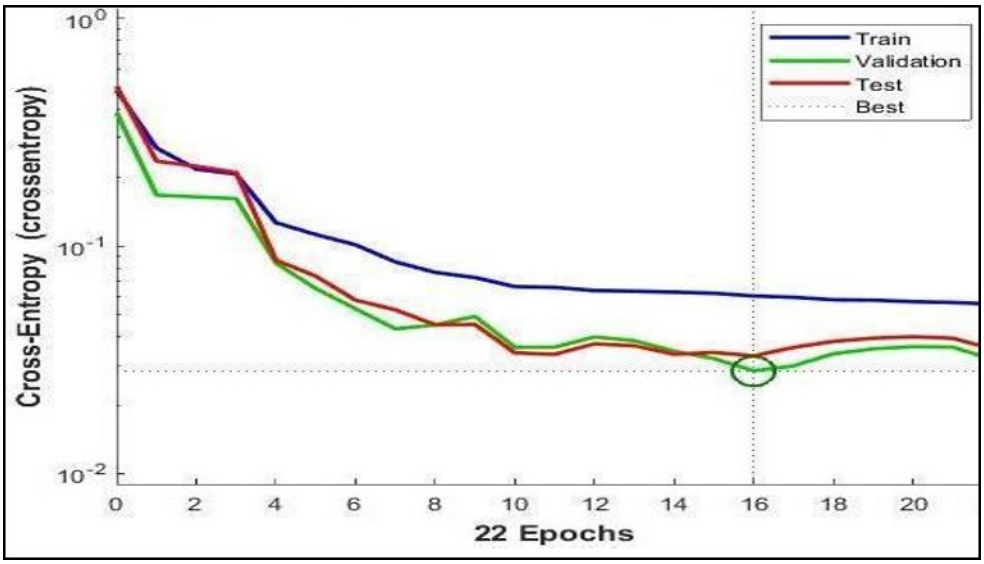

Forward Calculations

The trained and validated CNN and ANN models were used to perform forward calculations and to predict the crack type with an independent set of images and variables. The CNN and ANN models can be saved as a MATLAB file once the desired accuracy is achieved in the training and validation phases, which can then be used to perform forward calculations for crack classification. The data set consisted of 12 images with top-down cracking, 11 images with bottom-up cracking, and 8 images with cement-treated reflective cracking and their respective pavement and crack characteristics and was used to assess the accuracy of the developed models. Table 12 presents the results of the forward calculations.

Table 12. Forward calculation results

Crack Type	Number of Test Images	Correctly Predicted by CNN	Correctly Predicted by ANN	Correctly Predicted by both CNN and ANN
Top-down	12	11 (91.7%)	12 (100%)	11 (91.7%)
Bottom-up	11	10 (90.9%)	10 (90.9%)	10 (90.9%)
CT reflective	8	7 (87.5%)	8 (100%)	7 (87.5%)
Total	31	28 (90.3%)	30 (96.7 %)	28 (90.3%)

As shown in Table 12, both CNN and ANN models achieved a satisfactory accuracy in crack classification. The CNN and ANN models in MATLAB were subsequently incorporated into a user-friendly computer program, which can be used by PMS engineers without advanced knowledge of machine-learning techniques. Based on the results of forward calculations, the following observations are made:

- The CNN model accurately predicted the crack types for all images with distinct cracks. However, for images with poor background illumination, excessive shadows, spots and stains, and containing blurry cracks, the crack classification from the CNN model should be validated with the predicted crack type from the ANN-based model.
- The prediction accuracy of top-down cracks for both models was higher compared to bottom-up and CT reflective cracks; this can be attributed mainly to three distinct characteristics of top-down cracks (crack orientation, crack location, and pavement age). Compared to the ANN model, the CNN model more accurately predicted the crack types for pavements that developed top-down cracks at later stages in their service life.
- Bottom-up cracking usually appears in the surface during the later stages of pavement service life. However, for the pavements with relatively small AC thickness and high traffic volume, the bottom-up cracks were observed to resemble top-down cracking. In this case, the models' accuracy was slightly inferior to other cases.
- The CT reflective cracks usually initiate as transverse and longitudinal cracks in the pavement with cement-treated base or subgrade and can appear during the early or later stages of pavement service life. CT cracks that appeared only as longitudinal crack in the wheel path were mistakenly classified as top-down or bottom-up cracking by the CNN model. Therefore, the crack classification from the CNN model should be cross-checked with the predicted crack type from the ANN-based model.

ANN and CNN Applications

The commercial MATLAB, which provides a design toolbox (MATLAB App designer) to develop standalone windows-based and MATLAB-based applications, was used in this study. The required dependencies for the developed applications were compiled using the MATLAB compiler, which also generates the installation file for the end users. The ANN and CNN applications were developed in MATLAB 2019a platform in a computer with Intel Core i5-4590S microprocessor and 8GB of RAM. The procedure to formulate the applications is explained in this section.

Create Input and Output Components. The input and output components were created by using app designer component library that provides sliders, push buttons, drop down lists, numeric edit fields, and axes (to present figures) components, which can be easily dragged and dropped into the canvas. These components allow the user to define the inputs and the application to present the results.

Create a Callback Function. The user interface (UI) components created in the first step were then assigned with specific functions known as callbacks, which are executed when the user interacts with the UI components. The application stores the user inputs once the user interacts with the UI components. The ANN code to classify pavement cracks into three classes was incorporated using the callback function created for the "Results" push button component. The neural network is first trained when the user clicks the "Results" push button. Then, the classification results for the respective inputs defined by the user are displayed in the "Table" component as shown in Figure 60.

Create Standalone Application. The standalone application was created using MATLAB Complier, which generates an installation file and incorporates both the standalone application and all the required dependencies. The end users can access the application after installing the installer generated by the compiler without the need of MATLAB in their computer. Figure 60(a) presents the interface developed to classify the pavement cracks using the ANN model. The results of ANN classification are displayed in the table with assigned class and net error with a description in yellow colored boxes.

Create MATLAB-Based Application. An application that presents both CNN and ANN results was also created using the MATLAB compiler by adding a section with "CNN Result" as presented in Figure 60(b). The CNN classification algorithm was incorporated along with the image processing algorithm in the "Open Image" push button such that the application processes the image and presents the result of CNN classification for the given image at once. However, this application requires the users to install a licensed version of MATLAB on their computer.

Figure 60. (a) ANN interface for crack classification, (b) CNN and ANN application for crack classification

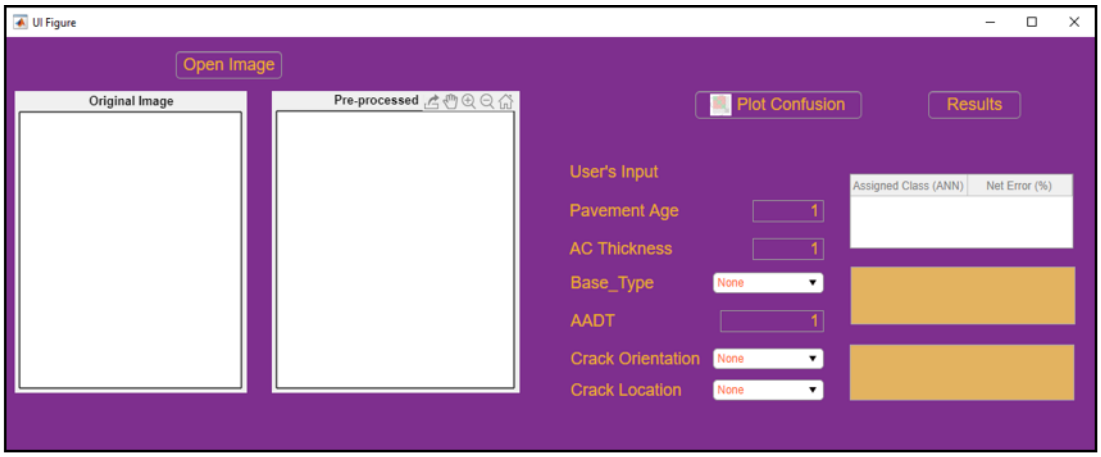

(a)

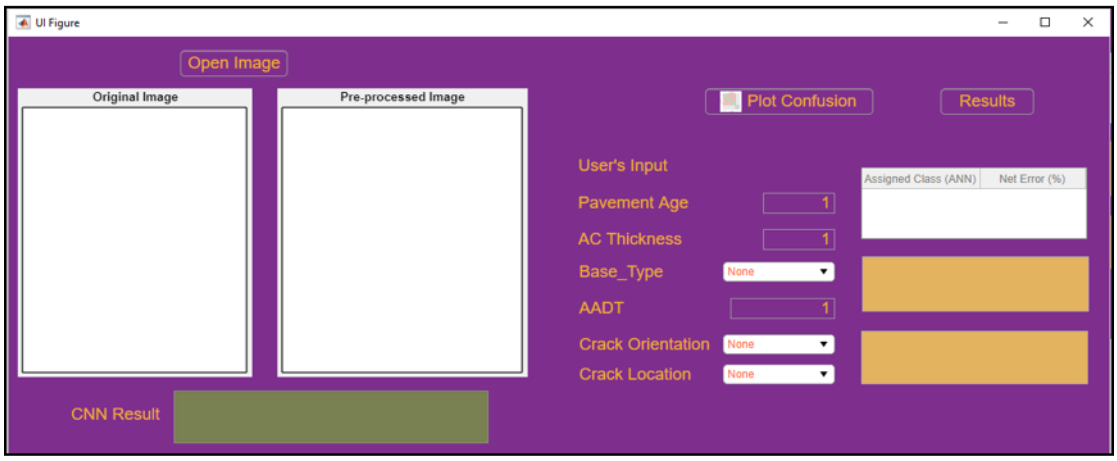

(b)

Steps to use the ANN and CNN applications. The use of the developed ANN and CNN applications consists of four main steps as detailed in this section.

- Step 1: Open Image

The "Open Image" push button allows the user to browse and open the digital pavement image on their computer for image processing as shown in Figure 61(a).

- Step 2: Image Processing

Once the user opens the digital image, the application processes the raw pavement image such that the orientation and location of cracks can be identified and used as input for the ANN model. The image processing algorithms including intensity normalization, median filtering, morphological erosion, and contrast enhancement are incorporated in the "Open Image" push button automatically. Hence, once the user opens the image using the push button, the application automatically processes the image. Figure 61(b and c) illustrates the image processing procedure in the application.

- Step 3: Enter Inputs for ANN Classification

The application requires the users to collect the pavement image with crack and six different inputs for the selected pavement section including pavement age, AC thickness, base type, ADT, crack orientation, and crack location. Numeric edit field components were created for pavement age, AC thickness, and ADT, which allows the user to enter the respective values. The user then defines the base type, crack orientation, and crack location using the drop-down menu. The base type drop-down menu allows the user to select between cement-treated base, untreated base, and PCC. The crack orientation allows the user to select between longitudinal, transverse, and both longitudinal and transverse. The crack location drop-down menu allows the user to select wheel path or outside wheel path for longitudinal crack and any location for transverse or transverse and longitudinal crack.

- Step 4: Results

The ANN classification code is incorporated in the "Results" push button in the interface. The corresponding class of the analyzed pavement crack can be obtained with one click of the button. The result of the classification is displayed in terms of number as "1," "2," or "3" where 1 indicates bottom-up, 2 indicates cement-treated reflective, and 3 indicates top-down cracking. The net error is also displayed along with the assigned class, which indicates the chance that a crack with given properties belong to other classes than classified. In case of the MATLAB-based application, the result of the CNN classification is displayed in "CNN Result" component once the users open the image.

Figure 61. (a) Open pavement image, (b) loading image, (c) processed image

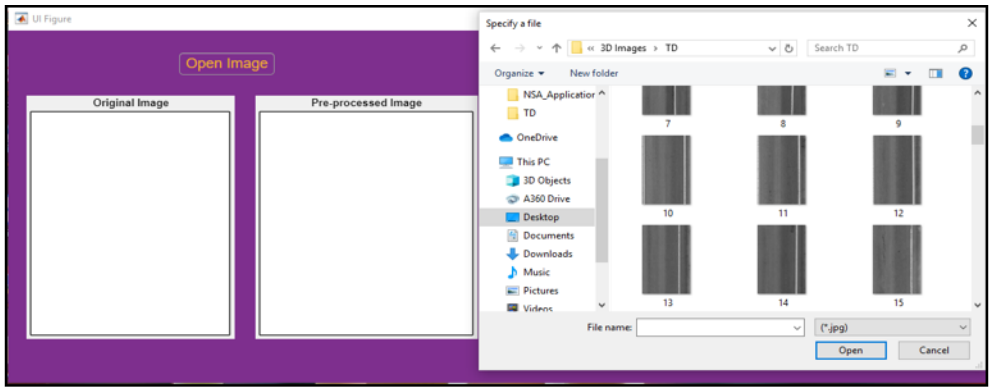

(a)

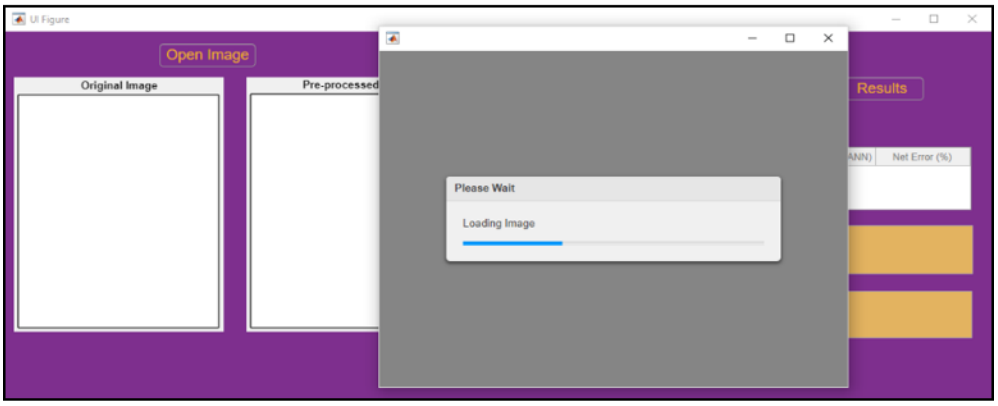

(b)

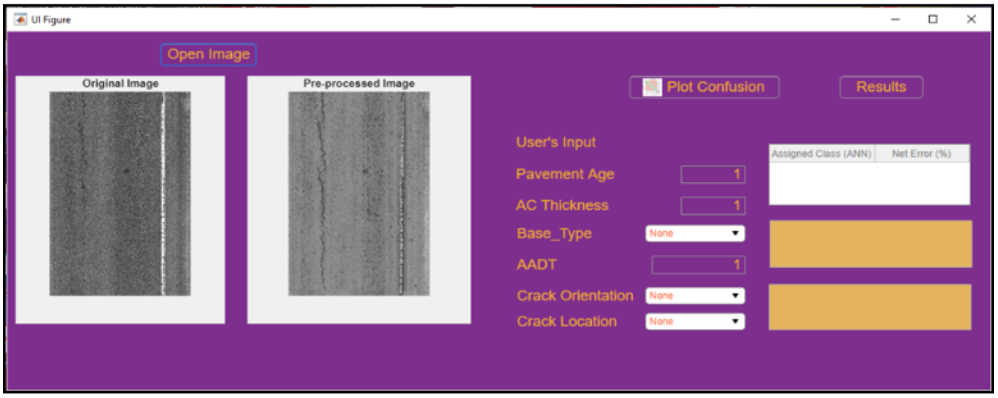

(c)

Case Studies. This section presents the application of the CNN and ANN models along with the Windows application to a number of field sections in order to classify the surface cracks as either top-down, bottom-up, or cement-treated reflection cracking.

Section 058-02. The pavement section is located on St. Tammany Parish (Parish 52) of Hammond district (District 62). The section had a length of 7.51 miles and the pavement structure consisted of 8-in. AC and a 6-in. stabilized granular base over a 5-in. clay subbase and clayey subgrade. An asphalt concrete overlay was applied within the pavement preservation program for a sub section with begin log mile of 0 and end log mile of 7.51. The final inspection date of the project was 12/6/2012. The section carries an ADT of 4,700. Top-down cracking initiated on the pavement section in 2016, which was validated with field coring. The longitudinal cracks appeared in the wheel path as shown in the preprocessed image. Figure 62(a) presents the results of CNN and ANN classification. As shown in the figure, both CNN and ANN successfully classified the pavement cracking as top-down cracking.

Section 262-03. The pavement section is located on Livingston Parish (Parish 32) of Hammond district (District 62). The section had a length of 6.41 miles and the pavement structure consisted of 8.5-in. AC and a 5.5-in. base over a clay subgrade. A cold planning, patching, and AC overlay were applied in a sub-section with a begin log mile of 0 and an end log mile of 6.41. The final inspection date of the project was 12/17/2013. The section carries an ADT of 15,000. Top-down cracking initiated on the pavement section in 2016, which was validated with field coring. Figure 62(b) presents the results of CNN and ANN classification. The longitudinal cracks appeared in the wheel path as shown in the processed image. As shown in the figure, both CNN and ANN successfully classified the pavement cracking as top-down cracking.

Section 011-04. The pavement section is located on Caddo Parish (Parish 09) of Bossier City district (District 04). The section had a length of 14.13 miles and the pavement structure consisted of 8-in. AC and a 6.75-in. red sand with gravel base over a clayey subgrade. An AC overlay was applied within the pavement preservation program for a sub-section with a begin log mile of 0 and an end log mile of 5.02. The final inspection date of the project was 10/5/2005. The section carries an ADT of 1,000. The section developed pavement surface cracking in 2014. Figure 64(c) presents the results of CNN and ANN classification. The cracks were not clearly visible in the preprocessed image due to excessive noise in the original image. The zoomed-in preprocessed picture showed longitudinal cracks in the wheel path. As shown in the figure, both CNN and ANN classified the pavement cracking as bottom-up cracking.

Section 857-63. The pavement section is located on Vermilion Parish (Parish 57) of Lafayette district (District 03). The section had a length of 10.79 miles and the pavement structure consisted of 3.5-in. AC and 9.5-in. cement stabilized sand clay gravel base over

a clay subgrade. A base stabilization and AC overlay were applied for a sub-section with a begin log mile of 0.65 and an end log mile of 10.85. The final inspection date of the project was 5/28/2013. The section carries an ADT of 2,300. Top-down cracking initiated in the pavement section in 2015, which was validated with field coring. The longitudinal cracks appeared on the wheel path as shown in the processed image. Figure 62(d) presents the results of CNN and ANN classification. As shown in the figure, both CNN and ANN successfully classified the pavement cracking as top-down cracking.

Section 003-10. The pavement section is located on Acadia parish (Parish 01) of Lafayette district (District 03). The section had a length of 11.367 miles and the pavement structure consisted of 6-in. AC and a 7.5-in. Portland Cement Concrete (PCC) base over a clay subgrade. An AC overlay was applied in a sub-section with a begin log mile of 6.28 and an end log mile of 11.377. The final inspection date of the project was 8/13/2012. The section carries an ADT of 6,700. The section developed pavement surface cracks in 2016. Figure 62(e) presents the results of CNN and ANN classification. As shown in the figure, both CNN and ANN classified surface cracking as cement-treated reflective cracking.

Section 014-06. The pavement section is located on Rapides Parish (Parish 40) of Alexandria district (District 08). The section had a length of 13.21 miles and the pavement structure consisted of 9-in. AC and an 8.5-in. cement stabilized sand shell base over 9-in. PCC and a clayey subgrade. A cold planning and AC overlay were applied in a sub-section with a begin log mile of 3.44 and an end log mile of 10.75. The final inspection date of the project was 5/8/2008. The section carries an ADT of 7,800. Cement-treated reflective cracking initiated on the pavement section in 2016. Figure 62(f) presents the results of CNN and ANN classification. As shown in the figure, CNN successfully classified the pavement cracking as cement treated cracking while ANN mistakenly classified the cracking as bottom-up cracking. As discussed earlier, this can be attributed to ANN models' limitations to classify longitudinal cracking in the wheel path as cement-treated reflective cracking.

Figure 62. CNN and ANN classification results for sections (a) 058-02, (b) 262-03, (c) 011-04, (d) 857-63, (e) 003-10, (f) 014-06

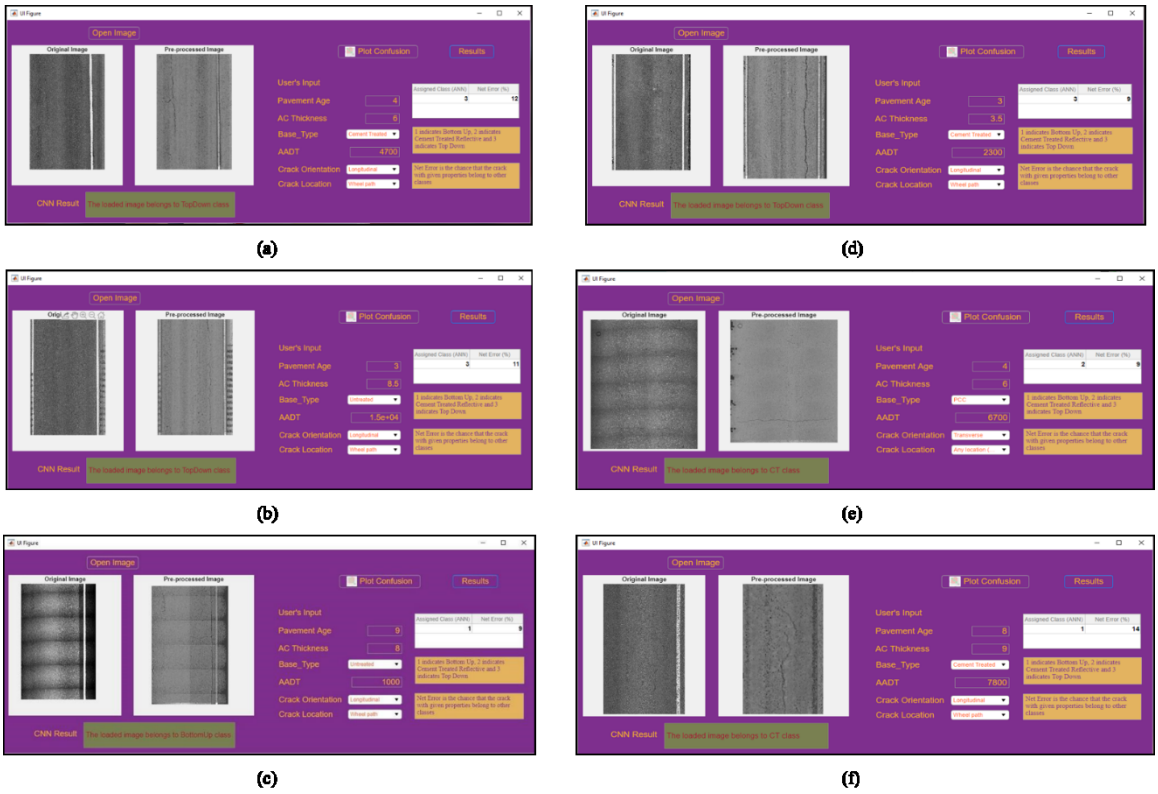

Asphalt Concrete Stripping Detection Using Deflection Measurements

Evaluation and Validation of the Logistic Regression Model

The soundness of the logistic model was assessed through significance test of the individual predictor variables with respect to the dependent variable, overall model performance evaluation, and goodness of fit statistics.

Statistical Significance of the Predictor Variables. In logistic regression, statistical significance of the predictors with respect to the dependent variable is assessed by the Wald Chi-Square ($\chi 2$) unlike conventional linear regression models, which may be assessed using conventional t-tests. Similar to linear regression, if the P-value of the predictor is less than 0.05, the predictor is considered statistically significant on the dependent variable. As shown in Table 13, the predictor variables used in the model showed significance with a P-value less than 0.05 except for the Rutting Index (RTI). However, the RTI variable was still included as it yielded a P-value close to 0.05 and it

improved the model's prediction to a certain extent. The RWD measured parameters used in the model (i.e., center deflection (D_0) and the standard deviation of D_0 measurements within 1 mile denoted as D_0STD), were statistically insignificant individually. Yet, the interaction term between these two variables (D_0* D_0STD) was significant in predicting the outcome of AC stripping.

Table 13. Logistic regression model evaluation

Predictor Variables	Estimate, β	Standard Error	Wald Chi-Square (χ^2)	DF	Pr > χ^2
Intercept	0.6281	1.5757	0.1589	1	0.6902
D_0* D_0STD	0.000418	0.000210	3.9726	1	0.0462
AC_{th}	0.1563	0.0463	11.3754	1	0.0007
TreatedBase	0.3063	0.1362	5.0602	1	0.0245
RTI	-0.02658	0.0158	2.8087	1	0.0938
Test			**χ^2**	**DF**	**Pr > χ^2**
Overall Model Evaluation					
Likelihood ratio test			34.5968	4	<0.0001
Score test			30.9908	4	<0.0001
Wald test			28.3533	4	<0.0001
Goodness of fit test					
Hosmer & Lemeshow			7.1499	8	0.5205
Deviance			138.6151	130	0.2864
Pearson			125.4202	130	0.5971
c*-statistic = *0.792					

Overall Model Performance. Overall, logistic model performance can be assessed by three statistical tests: the likelihood ratio test, the score test, and the Wald test. The significance value (P-value) for these tests is expected to be less than 0.05 if the overall model is a better predictor with the presence of the predictor variables than the intercept only model. The intercept only model, also known as the null model, can be rejected over the full model that includes the predictor variables with a P-value less than 0.05 based on the aforementioned model performance tests. For the present model, the tests suggest that the model with predicted variables was more effective than the null model as shown in Table 13.

Goodness-of-Fit Test. The goodness of fit test determines if the model's prediction is statistically acceptable against the actual outcome of the event. To test the goodness of fit, three statistical measures were considered; namely, the Hosmer & Lemeshow test,

Deviance, and the Pearson test *[71]*. If these tests are significant in terms of P-value (<0.05), then the proposed model needs to be rejected, while insignificant value suggests that the model's prediction is statistically acceptable. As shown in Table 13, all the goodness of fit parameters yielded an insignificant value supporting the acceptance of the developed model.

Validation of Model's Prediction. As previously mentioned, the logistic model predicts the logit (natural log) of the probability of an event based on the predictor variables. The natural log of the odds can be converted to the probability scale. The proposed model was developed to predict the probability of stripping in the pavement; therefore, higher probabilities would indicate the presence of stripping whereas lower probabilities are associated with no stripping. As shown in Table 13, c-statistic of 0.792 was calculated from the proposed model indicating that 79.2% of the pair of pavement sections had higher probabilities for stripped sections than for non-stripped section. A c-statistic of 1.0 would indicate that the predicted probability was higher for stripped sections than non-stripped sections for each pair of possible pavement sections.

The predicted probabilities are summarized in Figure 63, where it shows the change of probability estimation with the predictor variables. Two plots are illustrated for the categorical variable TreatedBase (0=if no treatment conducted on the base layer, 1=if the base is treated). Higher probability of stripping was noted with the increase in the AC layer thickness and the interaction term D_0* D_0STD (referred in the figure as DDSTD). This variation reveals that stripping is more likely to occur in pavements with higher surface deflection and higher variation in the deflection measurements obtained from RWD. This variation may also be concluded from the sign (+ve or -ve) of the regression coefficients presented in Equation (19). It can also be observed from Figure 63 that for the treated base segments, the probability of stripping was lower compared to the segments with untreated base. Furthermore, the negative sign of the regression coefficient for RTI suggest that with higher rutting index representing better rutting performance, the probability of stripping was lower. Hence, the model's characteristics agreed with engineering principles.

Figure 63. Predicted probability variation with the independent variables

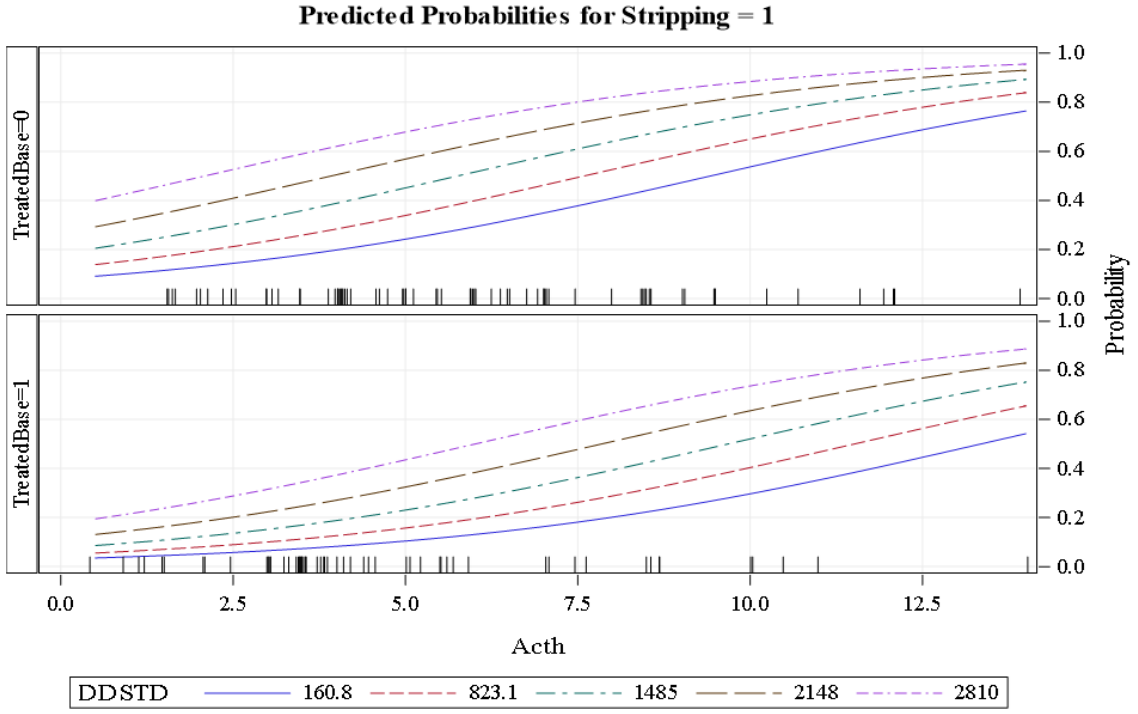

Further evaluation was conducted using the classification table obtained from the model's prediction at the different probability levels. This table can be effective in identifying the probability level that needs to be used to differentiate between stripping and non-stripped sections. As shown in Table 14, the sensitivity of the logistic model indicates the percentage of time the predicted probabilities are correct for a positive outcome. If a probability level of 0.35 were used to separate the stripped and non-stripped sections, about 82.6% of the time, the model would predict the stripped sections correctly whereas the specificity of 55.0% of the model means that about 55% of the time, the model would identify the non-stripped sections correctly. A false-positive rate of 44.9% at a probability level 0.35 means that about 44.9% of the time, the model identified AC stripping in pavement with a probability of 0.35 or greater even though they were not stripped; whereas a false-negative rate of 21% indicates that the probability for stripped sections were predicted lower than 0.35 about 21% of the time. Although the overall correctly predicted probabilities were 72.5% for all the sections at a probability level of 0.5, the probability level 0.35 would yield optimal results in terms of sensitivity and specificity; a higher percentage of sensitivity for the model is desirable so that AC stripping can be captured for the maximum number of sections.

Table 14. Classification based on predicted probability levels

Classification: Model Development Phase					
Probability Levels	**Percentages**				
	Correct	**Sensitivity**	**Specificity**	**False POS**	**False NEG**
0.1	54.1	97.8	31.5	57.5	3.4
0.2	62.2	91.3	47.2	52.8	8.7
0.3	68.9	78.3	64.0	47.1	14.9
0.35	*64.4*	*82.6*	*55.0*	*44.9*	*21.0*
0.4	68.9	60.9	73.0	46.2	21.7
0.5	72.5	50.0	83.1	39.5	23.7
0.6	68.9	30.4	88.8	41.7	28.8
0.7	68.1	17.4	94.4	38.5	31.1
0.8	65.9	2.2	98.9	50.0	33.8
0.9	65.9	0.0	100.0	-	34.1
1.0	65.9	0.0	100.0	-	34.1
Classification: Model Validation Phase					
0.3	56.1	76.1	44.4	55.5	0.23
0.35	*63.1*	*76.1*	*55.5*	*44.4*	*23.8*
0.4	66.6	*57.1*	72.2	27.7	42.8
0.5	70.1	47.6	83.3	16.6	52.3

The model was applied to an independent dataset; about 30% of the total data points were used for validation purpose. Although the prediction accuracy for the validation dataset decreased as compared to the development phase, at a sensitivity of 76.1% and a false-negative rate of 23.8% at probability level 0.35, the model performance in predicting the stripping within a pavement is reasonable given that logistic model only considers linear parametric effects of the predictor variables. A generalized additive model was developed in order to investigate the non-linear parametric effects and is presented in the following section.

Generalized Additive Models

As shown in Table 15, the smoothing function was assigned on the predictor such that they are statistically significant except ACth (asphalt concrete layer thickness). As shown in Figure 64(d), ACth is linearly related in estimating stripping probability; therefore, no smoothing function was used and the degree of freedom (DF) was 1.0 with statistical significance depicting a P-value less than 0.05. The splines of the center deflection (D_0)

and Rutting index (RTI) showed significant non-parametric effect in predicting the probability of stripping with a DF of 3.0 for both the variables. The non-parametric effect of D_{18} (deflection at 18 in. distance from D_0) and D_0STD was observed to be insignificant with the loess smoother; yet, they were integrated in the model as they improved the model's prediction accuracy in the validation phase and were found significant in the logistic model. The negative slope between D_0 and D_{18} referred as Slope, i.e., $(D_{18}-D_0)/18$, and Log of ADT (Annual Daily Traffic) were also observed to be statistically significant. The proposed GAM model had the following form:

$$\log\left(\frac{P}{1-P}\right) = \beta_0 + s(D_0) + lo(D_{18}) + lo(Slope) + ACth + lo(D_0STD) + s(RTI) + lo(logADT) \quad (39)$$

Where, P = the probability of stripping.

Table 15. Evaluation of the generalized additive model (GAM)

Predictor variables	Type of smoothing function used	DF	Significance		
			F-value for Parametric eff.	Chi-Square (χ^2) for Non-parametric eff.	Pr
D_0	Smoothing splines	3.0	-	20.9699	0.0001069
D_{18}	Loess smoother	2.9	-	4.1192	0.2292714
Slope	Loess smoother	2.8	-	11.4792	0.0074054
ACth	NA	1.0	8.9272	-	0.0034760
D_0STD	Loess smoother	2.8	-	3.6696	0.2721296
RTI	Smoothing splines	3.0	-	8.5108	0.0365380
lo(ADT)	Loess smoother	1.0	15.1501	-	0.0001719

The GAM model is more valuable when presented graphically with parametric or non-parametric effect of each predictor variable. The non-linear effect of each variable is evident in Figure 64 except ACth. When the GAM model was applied to the validation dataset, the misclassification rate was found to be 0.25 meaning that, the model correctly predicted 75% of the time whether the pavement was diagnosed with stripping or not.

Figure 64. Component plot of each predictor variable (as defined in Table 15)

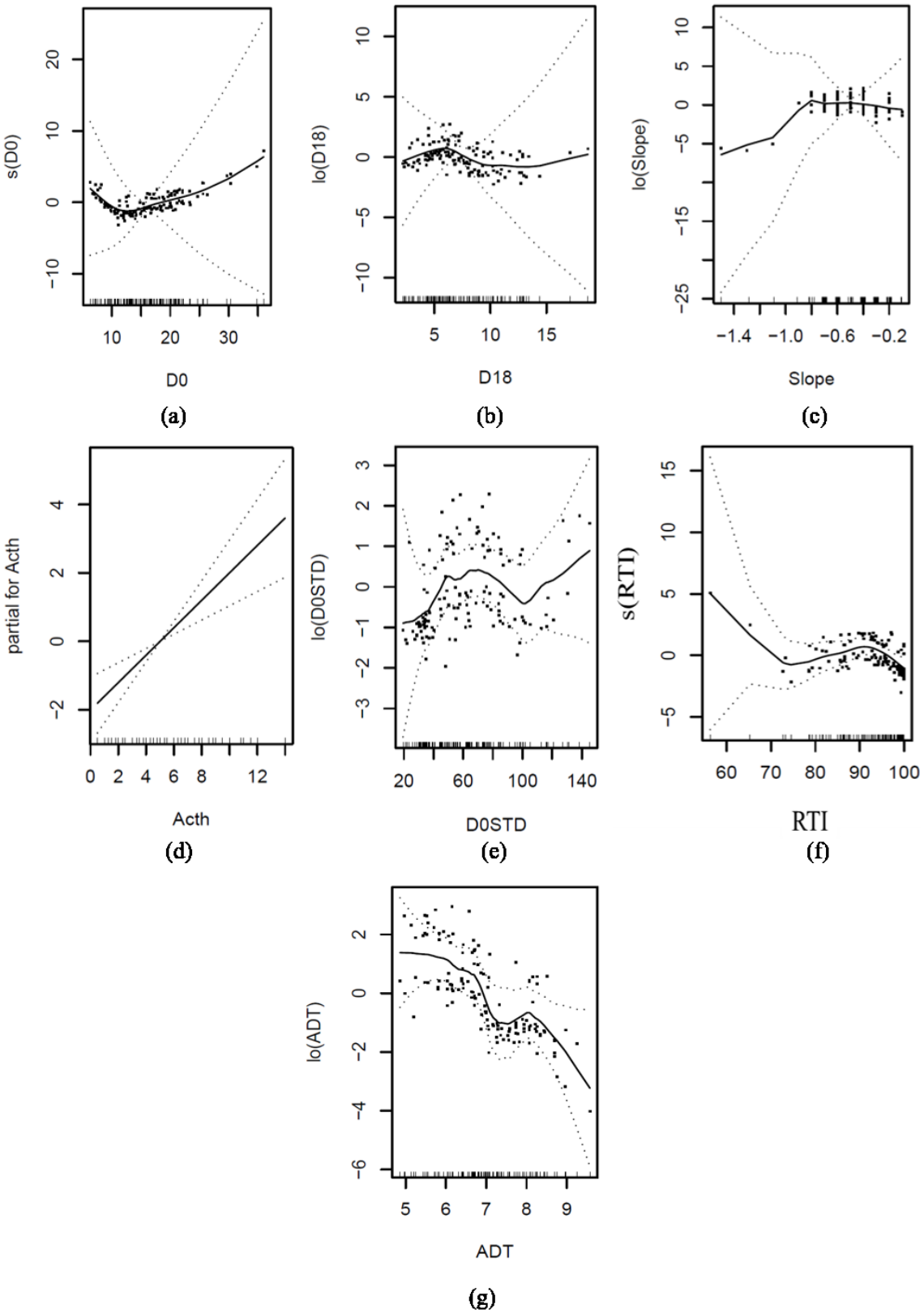

ANN-Based Pattern Recognition System

The ANN network performance was evaluated based on how well it performed in the validation phase. The proposed neural network could successfully classify stripped and non-stripped pavements with a 78% accuracy in the validation phase. The area under the curve was obtained to be 0.77 from the ROC (Receiver Operating Characteristics) plot shown in Figure 65; this is a graphical representation of how well the network can differentiate between the two classes, which are obtained from false-positive rate in the x-axis and true-positive rate in the y-axis. The neural network classified the validation dataset with a sensitivity of 70%, a specificity of 83.3%, a false-positive rate of 16.6%, and a false-negative rate of 30%.

Figure 65. Receiver operating characteristics (ROC) plot

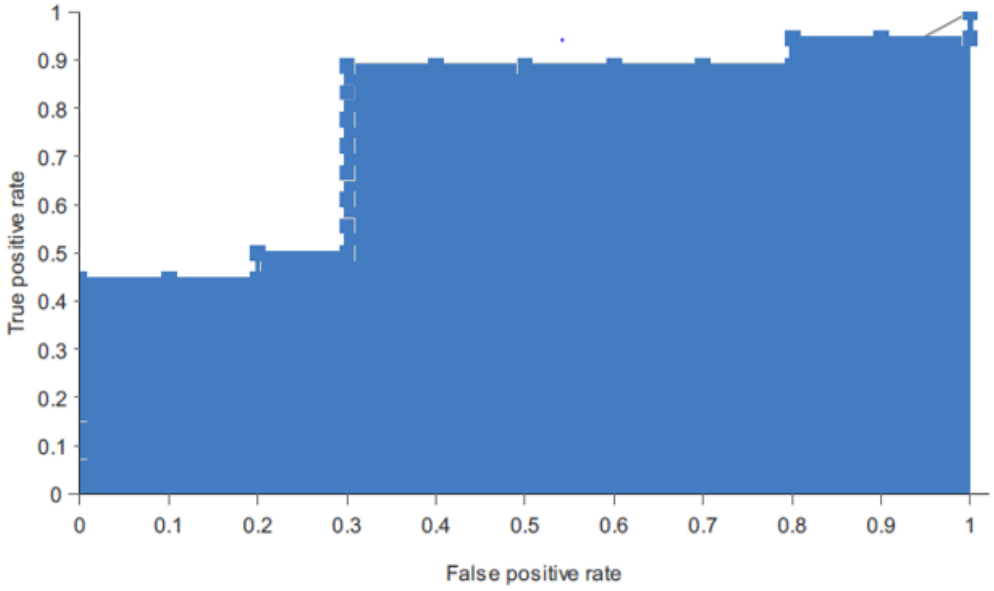

In summary, the neural network performed well with a greater accuracy than the logistic model or generalized additive model (GAM) presented in the study. Yet, the logistic model has better sensitivity than the neural network, which is desired as the goal was set to identify stripped sections. Furthermore, the GAM model had a special feature over the ANN-based model that the non-linear relationship between the predictor variables and dependent variable could be interpreted from the graphical representations. Therefore, the ANN tool would be useful in cross-validating the results from the logistic and GAM models.

Classification Tree. The proposed classification tree had 15 terminal nodes with 6 predictor variables as shown in Figure 66. At a particular node of a tree, the left-hand branch belongs to the criterion mentioned (i.e., ACth <4.65 in.), and the right-hand branch belongs to its contrasting criterion (i.e., ACth ≥ 4.65 in.). The decision "Yes" indicates the pavement is stripping-affected and "No" indicates otherwise. The units of the variables used are ACth in inches, Slope refers to the negative slope between D_0 (mils) and D_{18} (mils), and a value of 0 for TreatedBase means the base is not treated (TreatedBase=1, if treated). The illustrated classification tree achieved a classification error rate of 0.13 indicating that 87% of the cases could be successfully explained through this tree to identify if a pavement was diagnosed with AC stripping or not. It is evident in Figure 66 that ACth, Slope, and D_0 are the most important predictors for the presence of stripping as they reside on top of the tree as well as frequently appear in the process of classification. This tree would conveniently assist agencies in identifying the stripped sections using RWD measurements.

Figure 66. Classification tree to identify stripped pavement sections

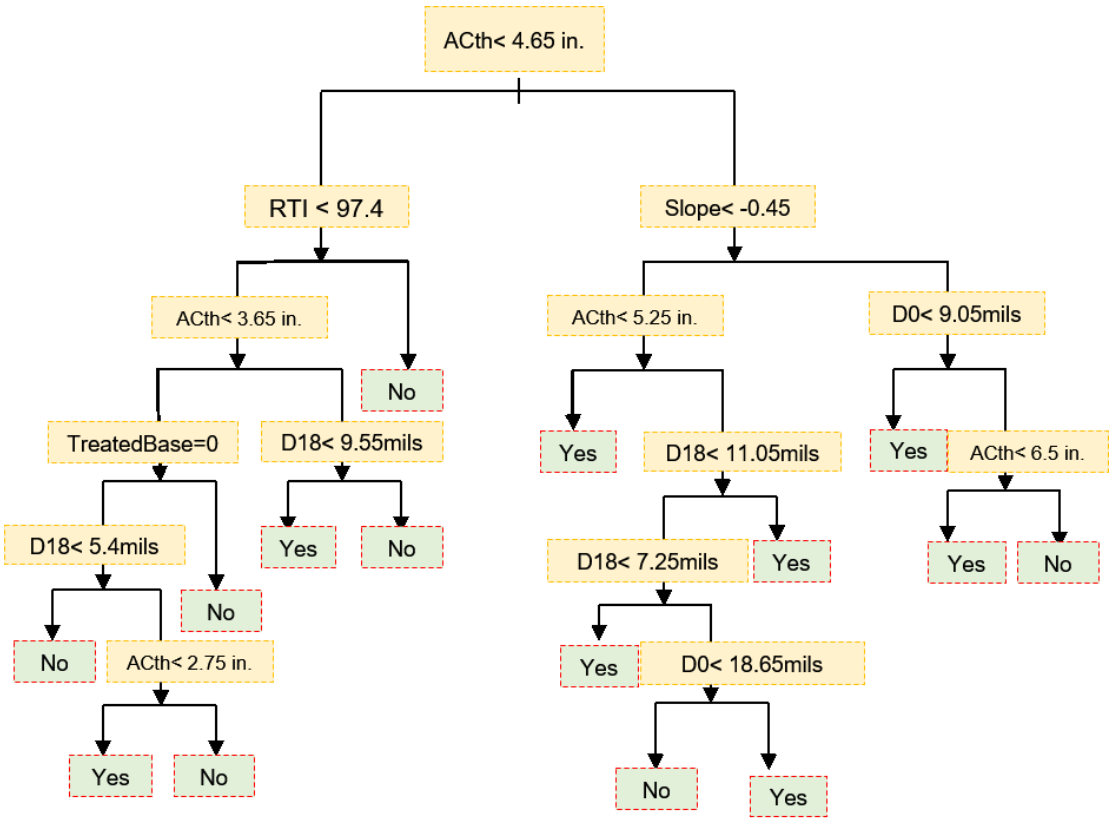

**Yes= Stripping; No= No Stripping*

Figure 67 presents the results of stripping detection using the AIP indicator for 156 non-stripped and 46 stripped pavement sections. The x-axis represents the section number in each data set. As shown in Figure 67, contrasting values of AIP were observed for stripped and non-stripped sections; the average AIP values for the stripped and non-stripped sections were 1.622 and 0.358, respectively. Because of the existence of noisy signal, the AIP value of most non-stripped sections were non-zero but low. The AIP values of stripped sections varied over a large range but most of the values were larger than 0.9. The 95% confidence intervals for the non-stripped sections were 0.358 ± 0.05 and were 1.622 ± 0.29 for the stripped sections.

Figure 67. AIP results for stripped and non-stripped sections

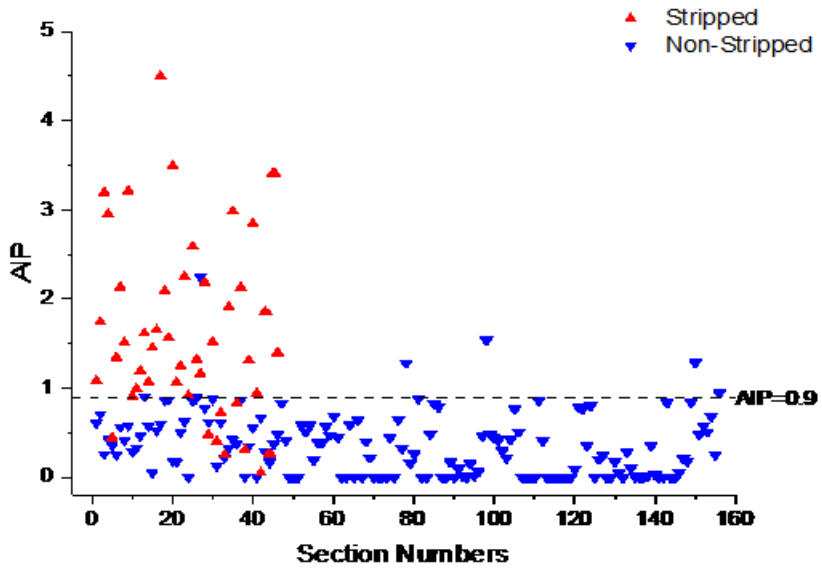

The Interactive Interpolation module of the RADAN software was used to semi-automatically locate and analyze features in the GPR scans by placing "picks." RADAN defines a "pick" as a peak amplitude identified in a scan that corresponds to a layer. The top of the AC layer was identified with yellow picks while the AC-base interface was identified with green picks. The pick locations, depths, and reflection amplitudes for multiple layers were exported to an ASCII file (*.lay) at an interval of 0.01 mile. MS

Excel was used to further convert the extracted data to dielectric values in conjunction with the data collected from the roadway cores.

Based on this analysis, a threshold AIP value of 0.9 was selected to predict stripping damage in a pavement section. A pavement section is predicted to be non-stripped or stripped if its AIP is less than or greater than or equal to 0.9, respectively. Table 16 presents the results of the analysis for 237 pavement sections. The results indicate that AIP is an effective indicator for evaluating stripping damage potential in asphalt pavements. The predictive accuracies of stripped and non-stripped section were 82% and 96%, respectively.

Table 16. Prediction result accuracies based on a threshold of AIP=0.9

		Actual		Predictive Accuracy
		Stripped	Non-stripped	
Predicted	Stripped	45 (correct)	10 (Incorrect)	82%
	Non-stripped	7 (Incorrect)	175 (Correct)	96%
True Accuracy		87%	95%	

Number of sections =237

By comparing the conditions of stripped pavement cores with different AIP values, it was noticed that the AIP value can also be used to assess the severity of AC stripping damage. Figure 68 presents selected cores with different AIP value ranges. Cores in Figure 68(a to c) had an AIP value larger than 2.5. As shown in Figure 68(a to c), the stripping of these cores were severe, as manifested by delamination and missing parts. The core in Figure 68(b) was the most severe; the original AC layer was 13 in. thick and stripping was detected throughout the AC layer. The AIP value of the cores presented in Figure 68(d to f) ranged from 0.9 to 2.5. These cores had moderate delamination and particles loss. The stripping damage occurred at the bottom of the AC layer and started propagating upward. Cores presented in Figure 68(g to i) had AIP values smaller than 0.9. The stripping in these cases were minor, starting at the bottom of the AC layer but the upper part of the AC layer was in good condition. These results show that AIP can quantitatively evaluate the severity of AC stripping damage in flexible pavements.

Figure 68. Illustration of pavement cores with varying AIP values

(a) AIP = 3.20 (b) AIP = 3.50 (c) AIP = 2.85

(d) AIP = 1.17 (e) AIP = 1.65 (f) AIP = 1.86

(g) AIP = 0.72 (h) AIP = 0.83 (i) AIP = 0.05

Effect of Moisture Damage on the Performance and Cost-Effectiveness of Chip Seal and Overlay

Chip Seal Sections

Average Deterioration Rate (ADR). Figure 69(a) shows the effects of moisture-induced damage on the ADR of chip seal sections for different PCI^- conditions. For roads with PCI^- less than 80, the average deterioration rate was 6.5% and 3.5% for pavement sections with and without stripping damage, respectively. For pavements with $PCI^- > 80$, the ADR was almost the same for both stripped and non-stripped sections (see Figure 69(a)). The reason behind these trends is that pavement sections at the early ages, $PCI^- > 80$, may not be affected significantly by the presence of moisture damage. In addition,

ADR was calculated based on performance curves that were fitted to the first four survey cycles (i.e., eight years). During their early years, pavements usually experience similar and low deterioration rates. Therefore, the similar ADR values, which were observed for stripped and non-stripped sections for pavement sections with $PCI^- > 80$, are reasonable.

An Analysis of Variance (ANOVA) test was conducted at 95% confidence level (α=0.05) followed by a Tukey's Honest Significant Difference (HSD) test in order to evaluate the impact of moisture-induced damage on the ADR of chip seal sections. Pavement sections with $PCI^- < 80$ and $PCI^- > 80$ were divided into two subgroups as sections with stripping damage and sections without stripping damage in order to analyze the effect of moisture damage at different PCI^- conditions. As shown in Figure 69, the average value of each performance indicator was represented by letters A, B, or C. Different assigned letters indicate that the two groups are statistically different. As shown in Figure 69(a), the ADR of chip seal sections with $PCI^-<80$ was affected significantly by the presence of moisture-induced damage. However, the effect of moisture-induced damage was insignificant for pavement sections with $PCI^->80$.

Figure 69(b) presents the ADR of stripped and non-stripped road sections for different traffic levels. When ADT was less than 1,100, stripped sections exhibited an ADR of 5% compared to 2% for the non-stripped sections; this difference was statistically significant. However, at medium traffic level, moisture-induced damage increased the deterioration rate by about 1.5%; however, this difference was not statistically significant.

Extension of Pavement Service Life Service (ΔPSL). Figure 69(c) presents the effects of moisture-induced damage on ΔPSL of the sections treated with chip seal for different pre-treatment conditions. For sections with PCI^- less than 80, chip seal extended pavement service life by approximately 9.5 years when placed on pavement sections without moisture-induced damage. This extension was only 5 years when the chip seal was applied on stripped pavements at the same PCI^- level. Tukey's HSD results indicated that moisture damage decreased the service life of chip seal significantly, as illustrated in Figure 69(c). For pavements with $PCI^- > 80$, both stripped and non-stripped sections exhibited similar ΔPSL (about 5 years). The results in Figure 69(c) are consistent with the results presented in Figure 69(a). As previously noted, sections that are in good conditions prior to treatment were not significantly affected by the presence of moisture damage in the underlying layers. In addition, previous results by the authors also found that chip seal had minimal impact on the condition and the deterioration rate of pavements when the PCI^- is greater than 80. Therefore, equal ΔPSL for stripped and non-stripped sections, when PCI^- is greater than 80, is reasonable. Figure 69(d) presents the

effects of moisture damage on chip seals service life at two different traffic levels. At low traffic level (ADT<1100), moisture damage decreased chip seal service life significantly by 8 years, as implied from the Tukey's HSD test results. At medium traffic level (1100<ADT<5300), moisture damage decreased chip seals service life by 3 years; however, the impact of moisture damage was not significant.

Average Performance Increase over Treatment Life Relative to Pre-treatment Condition (PI). Figure 69(e) presents the effects of stripping damage on the PI for different pre-treatment conditions. For the sections with PCI^- less than 80, PI was 16.5% and 1.4% for non-stripped and stripped sections, respectively. These results indicate that the use of chip seal resulted in 16.5% improvement in pavement conditions over its service life for non-stripped sections. On the other hand, the average condition of stripped sections was enhanced by only 1.4%. For the sections with $PCI^->80$, PI was 7.5% when chip seal was applied on pavement sections without moisture damage. On the other hand, stripped sections exhibited an overall condition enhancement of 6.2% after applying chip seal. Similarly, the application of chip seal on sections without moisture damage improved the average pavement condition by 18.0% and 6.4% for low and medium traffic, respectively; see Figure 69(f). However, the PI was 3.5% for sections at both low and medium traffic levels when chip seal was applied on pavement sections with moisture damage.

Cost-Effectiveness (CE). As shown in Figure 69(g), non-stripped and stripped pavements achieved a CE of 1.3% and 0.5%, respectively at a $PCI^- <80$. However, sections with and without moisture damage exhibited similar cost-effectiveness of 0.6% when PCI^- was greater than 80. This trend agrees with the results presented in Figure 69 (a and c). As shown in Figure 69(g), moisture damage decreased the cost effectiveness of chip seal significantly for sections with $PCI^-<80$. On the other hand, the effect of moisture damage for pavement sections with PCI^- greater than 80 was negligible. Moisture damage reduced the CE of chip seal at both traffic levels; see Figure 69(h). At low traffic level, the presence of AC stripping decreased significantly the CE from 1.2% to 0.3%. For sections with medium traffic level, moisture damage decreased CE by 0.1%, which was not statistically significant.

Figure 69. Impact of moisture damage on the performance and cost effectiveness of chip seals

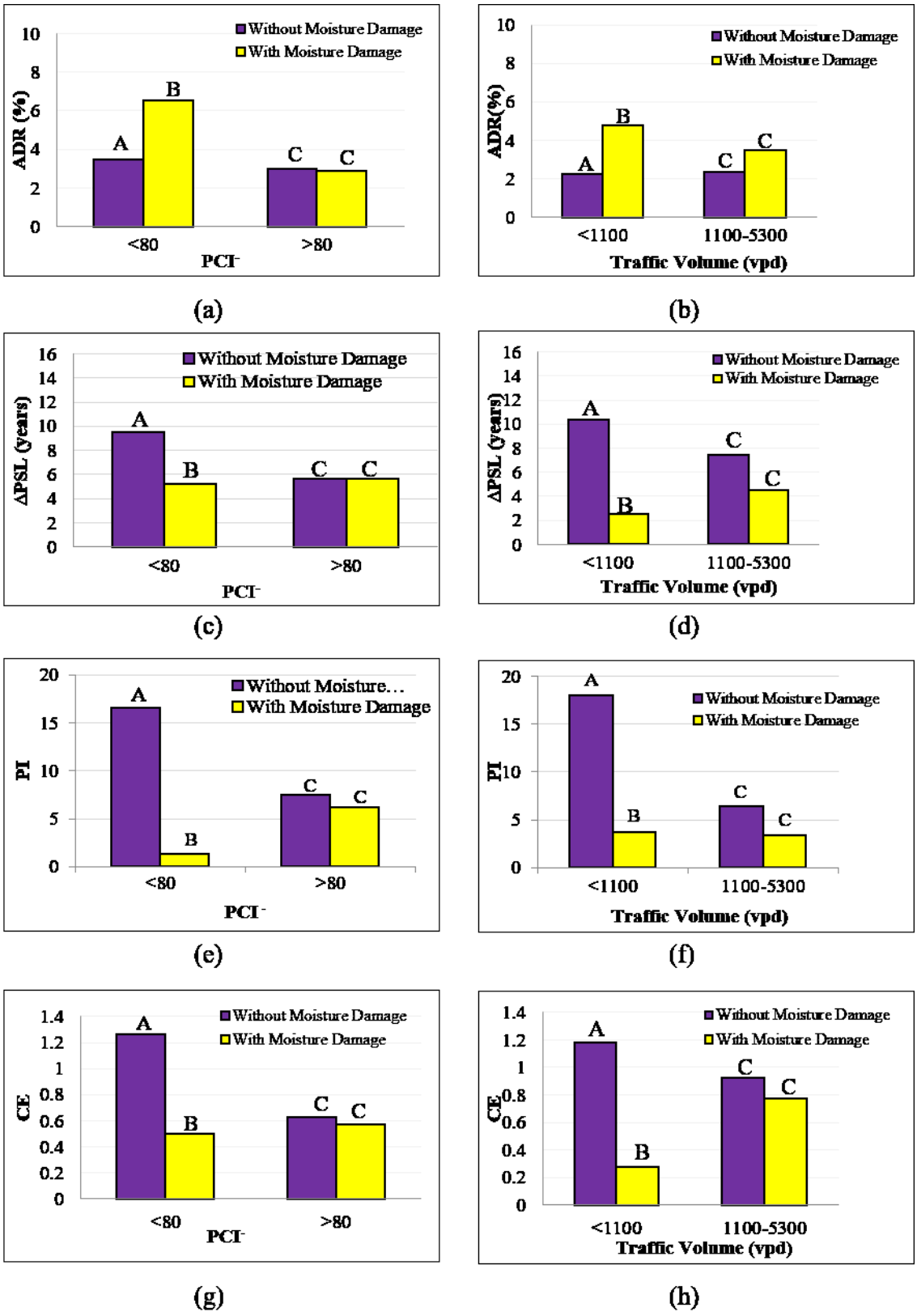

AC Overlay Sections

AC Overlay Average Deterioration Rate (ADR). Table 17 summarizes the effects of moisture damage on the ADR of AC overlays. The average deterioration rates were observed to be 4.0% and 9.4% for pavements without and with moisture damage, respectively. In Figure 70(a), ADR was observed to be lower for sections without moisture damage than that of the sections with moisture damage at all traffic levels. In Table 17, the P-value of 0.00094 obtained from two-tailed t-test (at a confidence level of 95%) indicated a significant effect of moisture damage on the ADR of AC overlays. This significance was also illustrated by the results of the Tukey's HSD test as shown in Figure 70(a).

Table 17. Impact of moisture damage on overlay average deterioration rate

Statistical factor	Average Deterioration Rate (%)	
	without Moisture Damage	with Moisture Damage
Mean ADR	4.0	9.4
P-value	0.00094	

Extension of Pavement Service Life Service (ΔPSL). The effect of stripping damage on the service life of the AC overlay is presented in Table 18 and Figure 70(b). As shown in Table 18, AC overlays extended pavement service life by 13.3 and 8.7 years, on average, for pavements without and with moisture-induced damage, respectively. Furthermore, the average ΔPSL was statistically greater for non-stripped sections than for stripped sections (except for the >16,000 ADT category).

Figure 70(b) shows the effects of moisture-induced damage on the PSL of AC overlay. As shown in the figure, the non-stripped sections outperformed stripped sections with an average increase in pavement service life of 13 years at all traffic levels. Likewise, in all sections, ΔPSL increased with the increase of ADT when an AC overlay was applied on stripped pavements. Based on these observations, it is assumed that the reduction in ΔPSL of AC overlays can be attributed to moisture-induced damage.

In Table 18, a P-value of 0.037 was obtained from a two-tailed t-test, at a confidence level of 95%, indicating a significant impact of moisture damage on AC overlay pavement service life. The different assigned letters (A and B) for stripped and non-stripped sections in Figure 70(b) also show the significant effect of moisture damage. These results imply that moisture damage had a significant impact on the service life of

AC overlays. Moreover, the thicker the AC overlay the less impact of moisture damage on the AC overlay service life would be experienced.

Table 18. Impact of moisture damage on pavement service life

Statistical factor	Pavement Service Life (years)	
	Without Moisture Damage	With Moisture Damage
Mean ΔPSL	13.3	8.7
P-value	0.037	

Average Performance Increase for AC Overlays. Figure 70(c) and Table 19 show the impact of moisture-induced damage on the PI of the sections treated with AC overlays at different traffic levels. For pavement sections without moisture damage, the range of PI was between 35% (at traffic volume between 4,000 and 8,000 vpd) and 12.5% (at traffic volume between 8,000 and 12,000 vpd). For stripped sections, the PI ranged from -1.2% to 7.5%. The negative sign means that at a traffic level of ADT < 4,000, the average pavement condition after placement of AC overlay was less than the PCI^- by 1.2%. It is worth noting that all non-stripped sections performed better, in terms of PI, than the stripped sections. In addition, the PI values were statistically greater for non-stripped sections than for stripped sections at all traffic levels. The stripped and non-stripped section also exhibited significantly different PI values as can be inferred from the P-value of 0.0022 shown in Table 19 and the Tukey's HSD results presented in Figure 70(c).

Table 19. Impact of moisture damage on the PI of AC overlay

Statistical factor	PI (%)	
	Without Moisture Damage	With Moisture Damage
Mean CE	28.0	5.0
P-value	0.0022	

Cost-Effectiveness (CE). The effect of moisture damage on the cost-effectiveness of AC overlays is presented in Table 20 and Figure 70(d). The average values of CE were 1.1% and 0.6% for non-stripped and stripped pavements, respectively, when treated with AC overlay. In Figure 70(d), the cost-effectiveness of AC overlays was significantly lower for AC overlays constructed on sections with existing moisture damage than for AC overlays placed on non-stripped sections (except for traffic volume greater than 16,000 vpd). A P-value of 0.004 obtained from the two-tailed t-test results (at a confidence level of 95%) indicated a significant impact of moisture damage on the CE of AC overlays. The

significance is also supported by the different assigned letters (A and B) obtained from the Tukey's HSD test for stripped and non-stripped sections as shown in Figure 70(d).

Table 20. Impact of moisture damage on overlay cost-effectiveness

Statistical factor	Cost-effectiveness (%)	
	Without Moisture Damage	With Moisture Damage
Mean CE	1.10	0.60
P-value	0.004	

Figure 70. Impact of moisture damage on the performance and cost effectiveness of AC overlays

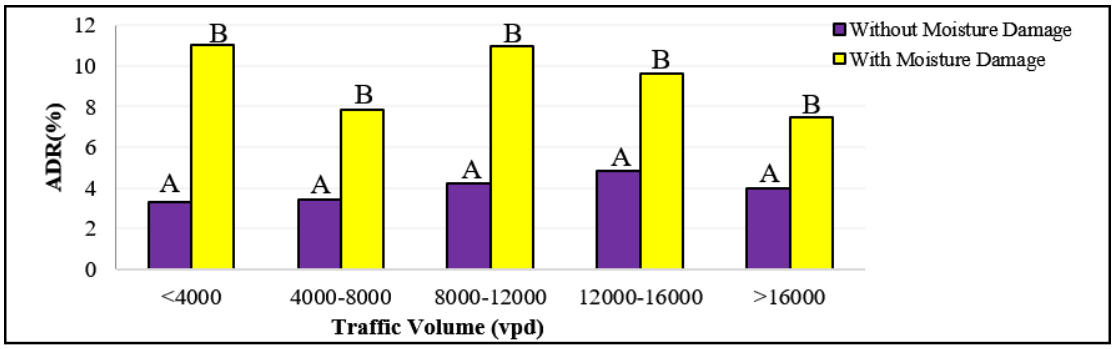

(a)

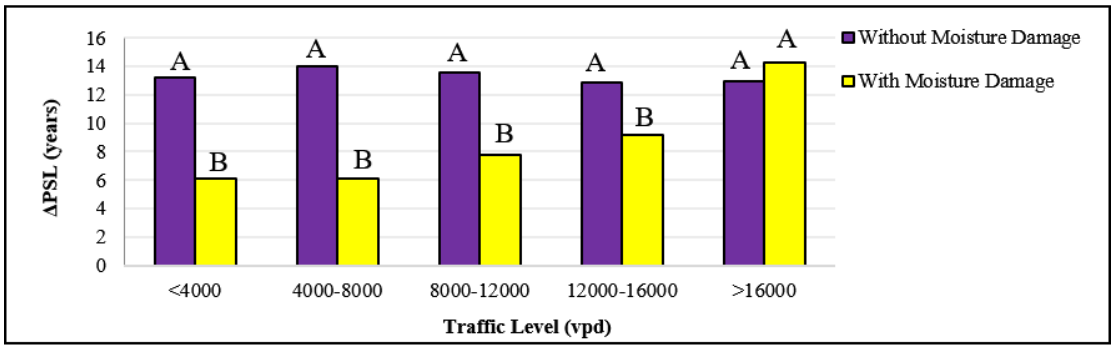

(b)

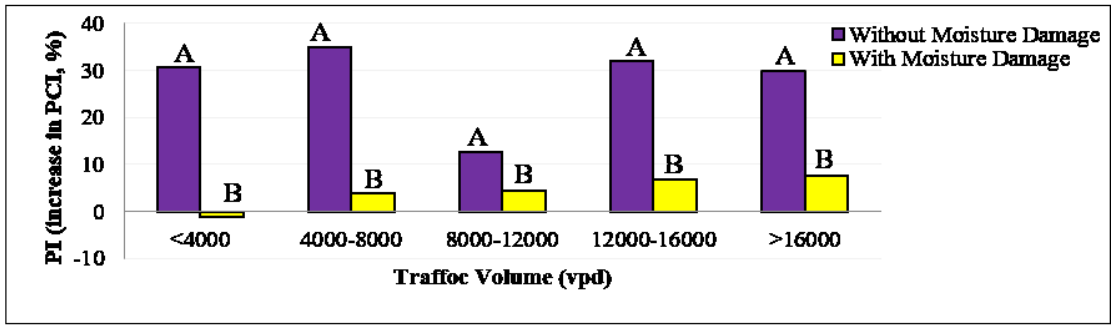

(c)

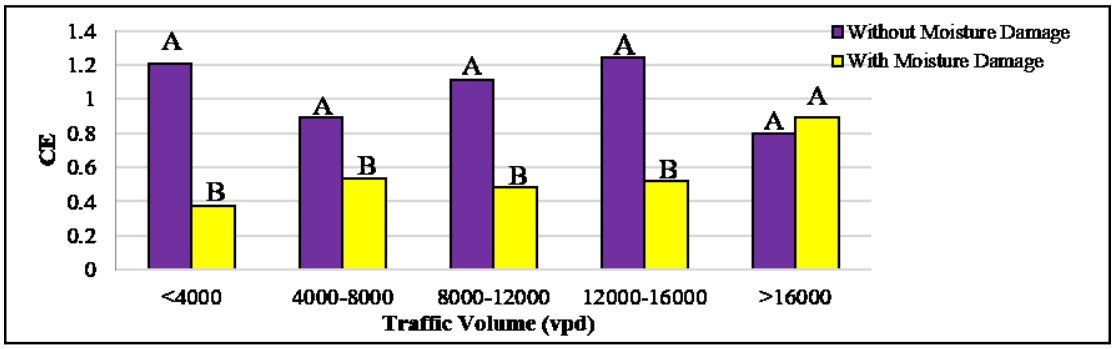

(d)

Prediction of Pavement Roughness Conditions Using Surface Images

CNN Model

A dataset consisting of 850 3D pavement images of size of 1040 x 1609 pixels was used to train and validate the developed CNN model. The images were labeled into four different categories based on the surface roughness conditions, as shown in Table 10. The appropriate selection of the training dataset allows the model to explain the variation in the input data and subsequently develop the optimum model with minimum errors. In addition, a validation dataset is required to assess the performance of the developed model using an independent dataset, which is not included in the training stage. Several trials were conducted with different percentages for the training, testing, and validation datasets in order to obtain the least variance and to avoid overtraining. Eventually, this study used 70%, 20%, and 10% of the data for training, testing, and validation, respectively. The aforementioned percentages were selected since they yielded the best statistics over all stages compared to the other percentages. It is worth noting that the images were selected randomly in all stages.

The accuracy of the CNN model was expressed in the form of confusion matrices, which present the actual and predicted classes in terms of number and percentage. Figure 71 presents the confusion matrices for the training and validation stages. The CNN classified the images into their pre-labeled categories with an overall accuracy of 93.4% in the training stage and 89.6% in the validation stage. For the “Fair” and “Good” groups, the accuracy was 92.0% and 100% in the training stage, respectively. However, the accuracy decreased to 82.8% and 88.2% in the validation stage, respectively. The developed model successfully classified the images in the “Poor” category with accuracies of 86.8% and 92.3% in the training and validation stages, respectively. Furthermore, the model successfully classified the pavement images in the “Very Good” category with 97.3% accuracy in the training stage and with an accuracy of 100% in the validation stage.

Figure 71. Training and validation matrices of the CNN model

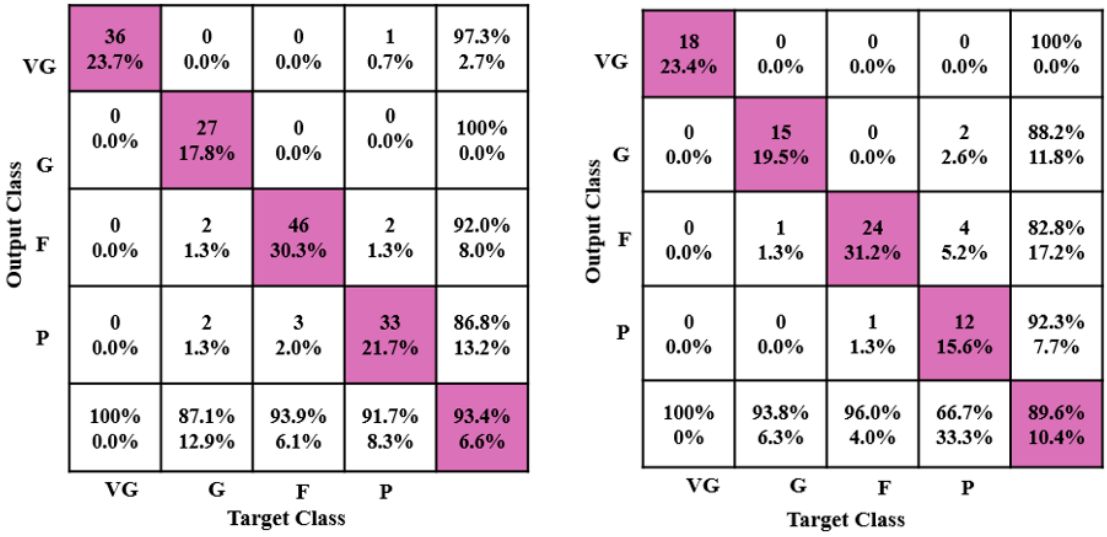

(a) Training Matrix

(b) Validation Matrix

ANN Model

There were 1,142 observations extracted from the DOTD PMS inventory and used to train, test, and validate the ANN model. These data were divided into 70% for training, 15% for testing, and 15% for validation. The training stage was stopped when the validation error leveled to avoid overfitting. Figure 72 demonstrates the confusion matrices for the training and validation phases for the ANN-based pattern recognition model. Overall, the ANN-based model exhibited low accuracies in the training, testing, and validation stages; see Figure 72. This performance was expected as the roughness conditions depend not only on the pavement surface distresses but also on pavement irregularities *[91]*. In all stages, the accuracy of the ANN model was about 58%. This accuracy was significantly lower compared to the accuracy of the CNN model.

Figure 72. Confusion matrices of the ANN model

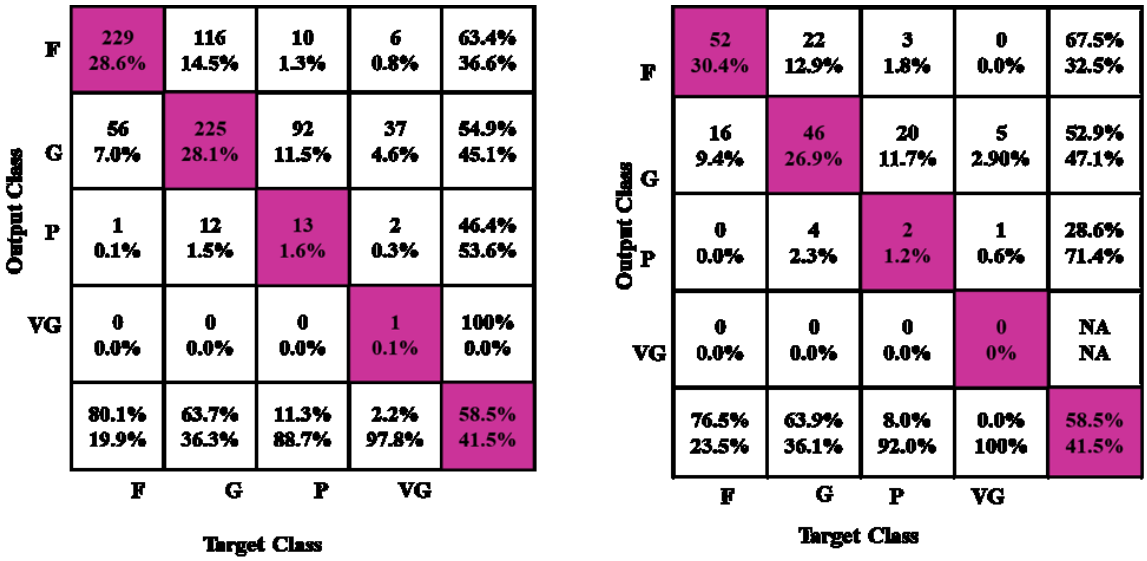

(a) Training Matrix (b) Validation Matrix

MNL Model

The SPSS software package was used to formulate the MNL model using 1,142 observations, which were divided into four groups based on the average IRI value as presented in Table 21. In addition, the study assessed the statistical significance of each independent variable (RTI, RCI, ALCR, and PTCH) on the dependent variable (different IRI categories). Finally, the potential of the MLN models to classify pavement sections into different roughness categories was evaluated.

MNL Model Development. In the current study, MNL models were developed for the evaluation of pavement roughness conditions. Using SPSS, the probability of each section to fall in a specific roughness category (see Table 21) relative to falling in the poor category was calculated according to Equations (40), (41), and (42) as follows:

$$\ln\left(\frac{P_{VG}}{P_p}\right) = -28.126 - 0.015 * RTI + 0.177 * RCI + 0.124 * PTCH + 0.028\ ALCR \quad (40)$$

$$\ln\left(\frac{P_{G}}{P_p}\right) = -3.427 - 0.015 * RTI + 0.028 * RCI + 0.048 * PTCH - 0.003\ ALCR \quad (41)$$

$$\ln\left(\frac{P_{F}}{P_p}\right) = 2.180 - 0.025 * RTI + 0.008 * RCI + 0.013 * PTCH - 0.012\ ALCR \quad (42)$$

Where, P_{VG} = the probability of a section to be in the "Very Good" roughness condition, P_G = the probability of a section to be in the "Good" roughness condition, P_F = the probability of a section to be in the "Fair" roughness condition, and P_P = the probability of a section to be in the "Poor" roughness condition.

Table 21. Wald test results

Parameter Estimates^						
Dependent Variables	**Independent Variables**	**β**	**Std. Error**	**Wald**	**Df**	**p-value**
Very Good	RTI	-0.015	0.012	1.438	1	0.230
	RCI	0.177	0.022	66.424	1	0.000
	PTCH	0.124	0.038	10.840	1	0.001
	ALCR	0.028	0.016	3.165	1	0.075
Good	RTI	-.015	0.011	1.757	1	0.185
	RCI	0.028	0.016	3.135	1	0.077
	PTCH	0.048	0.009	26.199	1	0.000
	ALCR	-0.003	0.012	0.063	1	0.802
Fair	RTI	-0.025	0.012	4.376	1	0.036
	RCI	0.008	0.017	0.211	1	0.646
	PTCH	0.013	0.008	2.937	1	0.087
	ALCR	-0.012	0.013	0.872	1	0.350

^ The reference category is the Poor Category

Statistical Analysis. In logistic regression, the Wald Chi-Square test was used to evaluate the statistical significance of the independent variables on the dependent variable by examining the following hypothesis:

- H_o (null hypothesis): the set of the coefficients (β) are equal to zero;
- H_1 (alternative hypothesis): the set coefficients are not equal to zero.

An independent variable can be neglected if the null hypothesis is accepted, i.e., if the P-value is greater than 0.05. In other words, the removal of this independent variable from the model will not significantly affect the performance of the model. Table 21 presents the results of the Wald Chi-Square test. For the "Very Good" category, the significant independent variables were RCI and PTCH with P-values less than 0.05. Similarly, PTCH was the only significant independent variable for the "Good" category. For the

"Fair" category, only the RTI index was the only significant variable with a P-value of 0.036.

MNL Model as a Classification Tool. The probability of each observation to fall in a specific roughness category was calculated using Equations (40), (41), and (42). A given observation was classified into the "Very Good" if $P_{VG} > P_{G,}$ $P_{VG} > P_{F,}$ and $P_{VG} > P_{P.}$ Table 22 illustrates the confusion matrix for the MNL model. As shown in the table, the model achieved an overall accuracy of only 58%.

Table 22. Confusion matrix of the MNL model

Observations	Predicted				
	Very Good	Good	Fair	Poor	Overall Accuracy (%)
Very Good	332	87	0	0	79.2
Good	179	314	6	1	62.8
Fair	16	123	13	4	8.3
Poor	9	45	12	1	1.5
Overall Percentage (%)	46.9	49.8	2.7	0.5	57.8

IRI Value Prediction

Model Development. The aforementioned results, which showed the superior prediction capability of the CNN model, encouraged the authors to use CNN to predict the IRI values at the project level. For this purpose, the images were divided into 34 road sections with an average IRI value ranging from 50 to 342 in./ mile. The images that were extracted from the DOTD PMS were used in the development and validation of the CNN model.

For each section, 20 out of 25 images were used in the model development phase. The remaining five images were used to evaluate the performance of the developed model using independent datasets; these images were selected randomly and excluded images that were used in the model development phase. In this study, 680 and 170 images were used to develop validate the CNN model, respectively. During the model development phase, the images were divided into 70%, 20%, and 10% for the training, validation, and testing of the CNN model, respectively.

The accuracy of the developed CNN models to predict the IRI value was expressed in term of confusion matrices; however, these matrices cannot be presented in the

manuscript because they were 34 x 34 confusion matrices. For the training stage, the CNN model predicted the IRI value with an accuracy of 89%. In addition, the accuracy of the CNN in the verification stage was 85%. These results indicated that the CNN model could accurately predict the roughness category of the pavement sections as well as estimate their IRI values.

Model Performance Evaluation. The performance of the developed model was assessed using 170 digital images extracted from the DOTD PMS. These images represent 34 (five images from each section) road sections with different IRI values ranging from 50 to 342 in./mile. For each section, the developed model was used to predict the IRI value of each image. Then, the average IRI value of the five images was calculated and was compared with the corresponding measured IRI value.

Figure 73(a) demonstrates the correlation between the measured and predicted IRI values. Overall, the CNN predicted accurately the IRI value with R^2 of 0.985 and a Root Mean Square Error (RMSE) of 5.9% when the measured and predicted IRI values were compared. With respect to precision, the figure illustrates a slope and intercept of 0.959 and 6.046 in./mile of the unconstrained regression line between the measured and predicted values indicating no bias in the model predictions. Furthermore, Figure 73(b) indicates that the mean error is -1.325 indicating precise prediction of the IRI values. Figure 73 shows relatively higher scatter and error values when the CNN model was used to predict the IRI values of the pavement section with IRI value greater than 180. The reason for this behavior may be the high variation in the roughness characteristics of the pavement surface along the road sections at high IRI values, which may result in a significant difference in the performance of sequential segments within the same section. This will result in a wide range of IRI values along these sections resulting in a higher scatter and error values.

Figure 73. (a) Correlation between the measured and predicted IRI value (b) The relation between the residuals and the predicted IRI value from the CNN model

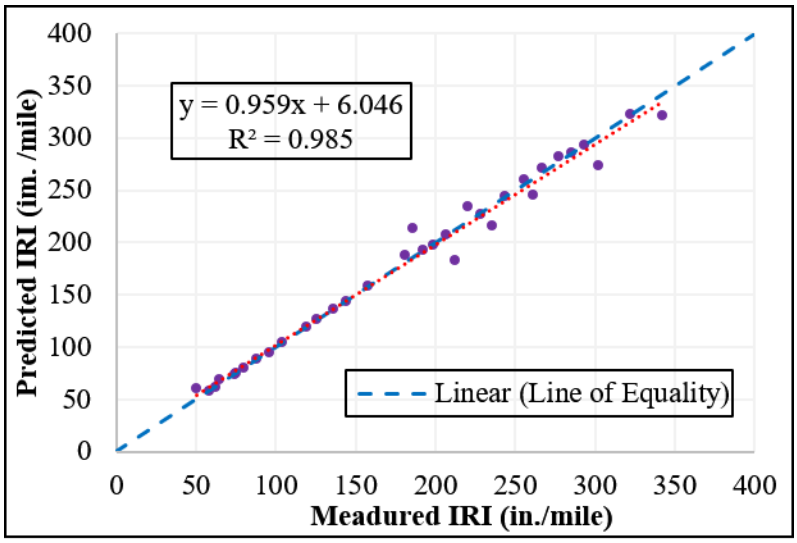

(a)

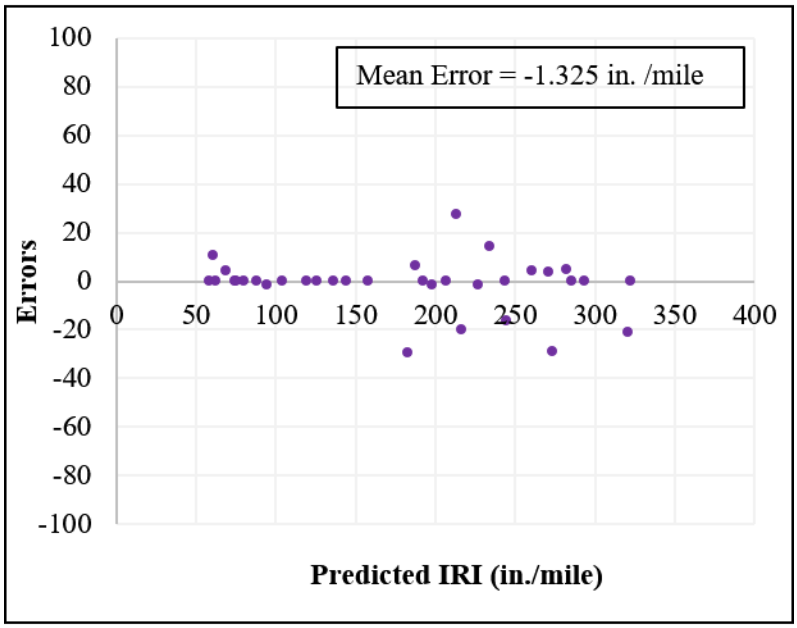

(b)

The performance of the developed model was evaluated statistically by examining the following hypotheses:

Hypothesis 1: the ability of the developed model to produce the same population of the measured IRI values was investigated using a two-tailed Z-test at a significant level of 95%, which examines the following hypotheses:

- H_o: the average of the predicted IRI values = the average of the measured IRI value
- H_1: the average of the predicted IRI values ≠ the average of the measured IRI value

The rejection of the null hypothesis (P-value <0 .05) would indicate that the model did not produce the same population as the measured IRI values.

Hypothesis 2: determine whether the slope of the unconstrained regression line between the predicted and measured IRI values equals the unity by examining the following hypotheses:

- H_o: the slope = 1
- H_1: the slope ≠ 1

The rejection of the null hypothesis (P-value <0 .05) would indicate that the slope of the linear regression model between the measured and predicted values is significantly different from unity. This also would indicate the inability of the model to predict precise IRI values *[92]*.

Hypothesis 3: examine whether the intercept of the unconstrained regression line between the predicted and measured IRI values equals zero by testing the following hypotheses:

- H_o: the intercept = 0
- H_1: the intercept ≠ 0

The rejection of the null hypothesis (P-value < 0.05) would imply that the intercept of the regression model between the measured and predicted IRI values is significantly different from zero. This would also indicate that the model produced biased predictions especially for low IRI values *[93]*.

Table 23 depicts the results of the tested hypotheses. The table shows that the CNN model was able to produce the same population of the measured IRI with a P-value of 0.949. In addition, a P-value of 0.059 indicates that the slope of the regression linear model between the measured and predicted IRI value is not significantly different from unity indicating insignificant bias in the predictions. Similarly, the intercept of the unconstrained linear regression model was not significantly different from zero (P-value

= 0.296), which reflects the model ability to produce accurate results especially at low IRI values.

Table 23. Statistical evaluation of the developed model

Hypothesis		Coefficients	Standard Error	t-state	P-value
1	Ho: Predicted = Measured	-	-	-	0.949
2	Ho: Slope = 1	0.959	0.021	45.940	0.059
3	Ho: Intercept = 0	6.046	4.178	1.447	0.296

Conclusions

Pavement Cracks Classification Using Machine Learning

The study identified and classified top-down, bottom-up, and cement treated reflective cracking in in-service flexible pavements without core extraction or other destructive tools. An image-based CNN model was developed that analyze the characteristics of pavement surface images. Furthermore, a one-step decision-making tool was developed using ANN to cross validate the crack classification obtained from the imaged-based CNN. To achieve this objective, 350 pavement images were pre-processed and were used as inputs for training, testing, and validation of the CNN model. It is worth noting that coring was only conducted for validation of top-down cracking. Additional coring is recommended to validate the propagation mechanisms of alligator fatigue cracking and cement-treated reflective cracking.

The input database for the CNN model contained both high quality pavement images with distinct cracks and images with high complexity such as cracks on shadowed surface, highly textured pavement surface, blurry cracks, and surfaces with poor background illumination and high intensity variation. For unprocessed pavement images, the model achieved an accuracy of 61.7% and 73.4% on testing and validation phases, respectively. The lower accuracy can be attributed to the presence of excessive pavement noise, non-uniform background illumination, pavement marking, spots and stains including cracking pattern. For the data set consisting of 2D images only, the developed network achieved an overall accuracy of 88.9% and 86.7% in the testing and validation phases, respectively. The overall accuracy for 2D and 3D images was 93.8% and 91% in the testing and validation phases, respectively. An ANN-based pattern recognition system was trained and validated based on pavement age, AC thickness, AADT, base type, crack orientation, and crack location to further validate the image-based classification. The developed model showed an acceptable decision prediction accuracy of 92%. Based on the overall accuracy, the approach of using pre-trained convolutional neural network model was observed to be successful for automated pavement crack classification. Based on the ANN classification model, a windows-based application was developed that allows the user to perform crack classification without installing MATLAB in their computer. An application that presents both CNN and ANN classification results was also developed by incorporating CNN classification algorithm into an UI component; however, this application requires the user to install a licensed version of MATLAB on

their computer. The use of the developed applications was successfully demonstrated for in-service pavement sections. While this study is one of the first attempts to classify pavement cracks with respect to their initiation and propagation, further improvement and training of the models is recommended to increase the crack classification accuracy.

Asphalt Concrete Stripping Detection Using Deflection Measurements

A methodology was developed to detect AC stripping in the underlying pavement layers based on TSDD measurements and variables related to pavement characteristics readily available to state agencies. As many agencies are considering the implementation of continuous deflection measuring devices for pavement structural evaluation, the analyses and methods presented in the study may be used for stripping damage detection and as an additional benefit of TSDD testing. From comprehensive modeling and analyses on the use of RWD measurements in stripping detection, the findings and recommendations of this task were as follows:

- The logistic model developed in the study was observed to be reasonable with a sensitivity of 76.1% in predicting the probability of stripping. The false-positive rate was higher compared to false-negative rate implying that the model could be used as a viable tool for initial screening at the network-level.
- The generalized additive model (GAM) successfully described the non-linear relationship between the probability of stripping and predictor variables considered in terms of RWD measurements and other pavement information. These non-linear relationships were validated with an accuracy of 75% in identifying AC stripping in pavement. However, further investigation in interpreting the non-linear relationship is recommended, which would be useful for improved accuracy.
- Compared to logistic and GAM models, the ANN pattern recognition system showed better performance with a stripping prediction accuracy of 78% while validating on a new pavement dataset. This was expected as ANN can adopt complex relationships between the predictor and dependent variables, while logistic model considers only linearity among the predictor and dependent variables and GAM captures the non-linearity that can be further subjected to sophisticated modeling. The ANN model can be used to cross-validate the results obtained from the logistic or GAM models.
- A decision tree was developed to classify stripping and non-stripped sections in the dataset. About 87% of the data could be successfully interpreted using this

classification tree. This is a simple and convenient way for state agencies to identify possible stripped sections for further evaluation.

Moisture Damage Detection Using GPR

The study developed a novel GPR-based indicator, the Accumulating In-layer Peaks (AIP), to detect stripping damage in asphalt pavement. A Finite-Difference Time-Domain (FDTD) based simulation program, gprMax, was used to study the propagation of GPR signal in stripped pavement sections. Field test data including GPR scans and visual inspection of cores were used to study the relationship between GPR traces and AC stripping damage. An indicator that may be used to detect stripping was developed and validated using cores extracted from 237 pavement sections. Based on the results of this task, the following conclusions may be drawn:

- The presence of void in middle of the AC layer resulted in positive peaks in the reflected waves as indicated by the simulation of the GPR signals. When the void was at bottom of the AC layer, the reflected waves from the interface between the void and AC layer, and void and base overlapped resulting in a higher strength of positive peaks compared to the non-stripped pavement.
- Detected intermediate wave peaks between the surface and the interface between AC and base layers on GPR traces were associated with stripping damage in the AC layer.
- The AIP predicted accuracies for stripped and non-stripped sections were 82% and 96%, respectively, indicating its effectiveness to detect stripping damage in flexible pavements. The value of AIP can also be used to quantitatively evaluate the severity of stripping damage in the asphalt layer.

Effect of Moisture Damage on the Performance and Cost-Effectiveness of Chip Seal and Overlay

The performance and cost-effectiveness of in-service pavement sections were evaluated to assess the effects of AC stripping on the performance of chip seal and AC overlay in Louisiana. Pavement sections were categorized and analyzed according to their pre-treatment conditions, traffic volume, and moisture damage in the underlying pavement. Based on the results of the analysis, the following conclusions were drawn:

- Pavement service life, the average performance increase, and cost-effectiveness decreased significantly when chip seal was applied on moisture-damaged pavements with a pre-treatment PCI of less than 80.
- The effect of AC stripping damage on the performance of chip seal was observed to be insignificant on the performance indicators including pavement service life, average deterioration rate, average condition increase, and cost-effectiveness for pavement sections with a pre-treatment PCI greater than 80.
- Similar results were observed for AC overlays. AC overlay extended pavement service life by 13.3 years when placed on non-stripped pavements but only performed adequately for 8.7 years when moisture damage was present in the underlying AC layers.
- Stripping damage decreased the cost-effectiveness of AC overlays from 1.1% to 0.6%. Furthermore, for pavement sections without moisture damage, the range of PI was between 35 and 12.5% but it was -1.2% to 7.5% for sections with moisture damage.

Prediction of Pavement Roughness Conditions Using Surface Images

Roughness prediction models developed during the last two decades have many limitations. First, most of these models require extensive data collection such as climatic and traffic data, pavement distresses, and pavement structural capacity. The collection of these data is costly, time-consuming, and may not be available to the user. Second, these models have geographical limitations; therefore, they cannot be used at different locations without recalibration. Finally, models that were developed based only on pavement surface distresses exhibited low accuracy. This low accuracy was the result of ignoring other irregularities that may affect pavement roughness.

To address these limitations, the present study developed a CNN model using a pre-trained network to classify pavement images into four different categories of pavement roughness conditions (Very Good, Good, Fair, and Poor). The CNN classification tool was trained, tested, and validated using 850 3D pavement images, which were collected from the DOTD PMS inventory. The CNN model classified the pavement images into the pre-labeled categories with an overall accuracy of 93.4% and 89.6% in the training and validation stages, respectively, indicating its effectiveness in predicting pavement roughness conditions.

An image-based CNN model was also developed using 680 3D images to predict the IRI value of the pavement section. The CNN predicted the IRI value with an accuracy of 89% and 85% in the training and validation stages, respectively. The developed CNN model was verified using 170 digital images, which represent 34 test sections with different IRI values ranging from 50 in./mile to 342 in./mile. The developed model accurately predicted the IRI values, which correlated with the measured IRI values at an R^2 of 0.985 and a RMSE of 5.9%.

The study also investigated the potential of ANN and MNL models to predict pavement roughness conditions. The ANN and MNL models were developed based on 1,142 test observations, which included average IRI of the pavement sections and four pavement distress indices (RTI, RCI, ALCR, and PTCH). The developed models achieved an accuracy of about 58% indicating their low accuracy as compared to the CNN models. Based on the results of the study, the developed CNN models are recommended for further validation with independent data sets obtained from different climatic regions. Upon validation, the developed CNN models provide numerous implementation opportunities into PMS activities. The developed model may also be incorporated to predict pavement surface roughness using camera-captured pavement images during the construction and pavement evaluation phases.

Recommendations

While this study introduced numerical methods and approaches to detect and predict moisture damage in pavements, further validation and fine-tuning of the models are recommended. In addition, the following recommendations are provided:

- The training, testing, and validation data set for the developed CNN model consisted of pavement images with known crack types. Further testing on the accuracy of the developed model is recommended by using pavement images with different crack types and core extraction.
- Coring was only conducted for validation of top-down cracking. Additional coring is recommended to validate the propagation mechanisms of alligator fatigue cracking and cement-treated reflective cracking.
- The developed tool can only be used for classification of a single crack pattern in a given image during the early stages of propagation. Therefore, future research studies should extend the developed tool to allow for classification of multiple crack patterns in a single image.
- The developed tool should be extended to a more specific tool that would test every pavement image for a tenth of a mile and label the classified cracks as 1-top-down, 2-bottom-up, or 3-cement treated reflective cracking.
- The pavement network in Louisiana is surveyed every two years. However, due to the inconsistencies in the pavement images before and after the year 2012, only the images after 2012 were used. This limited the number of images for each crack type in the developed model. Further improvement of the model is recommended as more data become available.
- The automated image processing step involved crack enhancement by using few mathematical operations. It is recommended to expand the developed methodology in order to increase crack classification accuracy in flexible pavements. This can be achieved by using advanced image processing techniques or a deep learning CNN that can automatically perform crack segmentation.
- The analyses and statistics presented in the study suggest that TSDD measurements can be useful for stripping detection, which comes as an added benefit of TSDD testing that is primarily used for pavement structural evaluation. By fine-tuning the models, the developed methodology could be applied to other TSDD devices such as

TSD. An algorithm and computer tool should also be developed to implement the results of these models and to provide a final prediction tool for AC stripping detection based on TSDD measurements.

- The AIP indicator is a promising parameter to detect AC stripping damage in asphalt pavements based on GPR test results. Further evaluation and validation of the AIP indicator is recommended prior to its implementation in Pavement Management System (PMS) activities.
- The results indicate that pavement-underlying conditions including AC stripping damage should be taken into consideration in PMS decision and treatment selection process. Furthermore, moisture damage should be effectively corrected before the application of maintenance or rehabilitation strategies for more durable pavements and optimum use of available funds.
- Based on the results of the study, the developed CNN models are recommended for further validation with independent data sets obtained from different climatic regions. Upon validation, the developed CNN models provide numerous implementation opportunities into PMS activities. The developed model may also be incorporated to predict pavement surface roughness using camera-captured pavement images during the construction and pavement evaluation phases.

Acronyms, Abbreviations, and Symbols

Term	Description
AC	Asphalt Concrete
ADR	Average Deterioration Rate
AADT	Annual Average Daily Traffic
ADT	Average Daily Traffic
AIP	Accumulating In-layer Peaks
ANN	Artificial Neural Network
ALCR	Alligator Cracking Index
ARAN	Automatic Road Analyzer
CE	Cost Effectiveness
CNN	Convolutional Neural Network
COV	Coefficient of Variation
CT	Cement-Treated
DOTD	Louisiana Department of Transportation and Development
FHWA	Federal Highway Administration
ft.	foot (feet)
FWD	Falling Weight Deflectometer
GAM	Generalized Additive Model
GPR	Ground Penetrating Radar
HMA	Hot Mix Asphalt
in.	in.(es)
IRI	International Roughness Index
Ksi	Kilo pounds per square in.
lbs.	Pound(s)
LRN	Local Response Normalization
LTRC	Louisiana Transportation Research Center
MNL	Multinomial Logistic

Term	Description
NDE	Non-Destructive Evaluation
PCC	Portland Cement Concrete
PCI	Pavement Condition Index
PMS	Pavement Management System
psi	Pounds per square in.
PSL	Pavement Service Life
PTCH	Patching Index
RFI	Roughness Index
RTI	Rutting Index
RMSE	Root Mean Square Error
RWD	Rolling Wheel Deflectometer
SD	Standard Deviation
SHRP	Strategic Highway Research Program
TDC	Top-Down Cracking
TSD	Traffic Speed Deflectometer
TSDD	Traffic Speed Deflection Devices

References

[1] Cao, Y., S. Dai, J. F. Labuz, and J. Pantelis. Implementation of Ground Penetrating Radar. Minnesota Department of Transportation, Maplewood, MN, 2007.

[2] Rmeili, E., and T. Scullion. Detecting Stripping in Asphalt Concrete Layers Using Ground Penetrating Radar. Transportation Research Record, Vol. 1568, No. 1, 1997, pp. 165–174.

[3] Hammons, M. I., K. Maser, and S. Nazarian. Detection of Stripping in Hot Mix Asphalt. Georgia Department of Transportation, Forest Park, GA, 2005.

[4] Khattak, M.J., Baladi, G.Y., Zhang, Z., and Ismail, S. A Review of the Pavement Management System of the State of Louisiana-Phase. Transportation Research Record: Journal of the Transportation Research Board, pp. 18-27, 2008.

[5] Tong, Z., Gao, J., and Zhang, H. Recognition, Location, Measurement, and 3D Reconstruction of Concealed Cracks Using Convolutional Neural Networks. Construction and Building Materials, 146, 775-787, 2017.

[6] Li, B., Wang, K. C., Zhang, A., Yang, E., and Wang, G. Automatic Classification of Pavement Crack Using Deep Convolutional Neural Network. International Journal of Pavement Engineering, 1-7, 2018.

[7] Svasdisant, T., Schorch, M., and Baladi, G. Y. Mechanistic analysis of top-down cracks in asphalt pavements. Paper presented in Transportation Research Board Annual Meeting, January 13-17, 2002.

[8] Myers, L. A., Roque, R., and Ruth, B. E. Mechanisms of surface-initiated longitudinal wheel path cracks in high-type bituminous pavements. Journal of the Association of Asphalt Paving Technologists, 67, 1998.

[9] Stuart, K., Mogawer, W., Romero, P. Validation of the superpave asphalt binder fatigue cracking parameter using an accelerated loading facility. Publication No. FHWA- RD-01-093. Turner Fairbank Highway Research Centre, McLean, VA, 2001.

[10] Uhlmeyer, J. S., Willoughby, K., Pierce, L. M., and Mahoney, J. P. Top-down cracking in Washington state asphalt concrete wearing courses. Transportation research record, 1730(1), 110-116, 2000.

[11] “DOTD Pavement Management System Guide” 2006.

[12] Elseifi, M. A., and Elbagalati, O. Assessment of continuous deflection measurement devices in Louisiana-rolling wheel deflectometer. Final report 581 (No. FHWA/LA. 17/581). Louisiana Transportation Research Center, 2017.

[13] Maser, K. R. Computational techniques for automating visual inspection. Massachusetts Institute of Technology, Report, Cambridge, MA, 1987.

[14] Li, L., Chan, P., Rao, A., and Lytton, R. L. Flexible pavement distress evaluation using image analysis. In Applications of Advanced Technologies in Transportation Engineering, ASCE, pp. 473-477, 1991.

[15] Otsu, N. A threshold selection method from gray-level histograms. IEEE transactions on systems, man, and cybernetics, 9(1), 62-66, 1979.

[16] Kittler, J., and Illingworth, J. Minimum error thresholding. Pattern recognition, 19(1), 41-47, 1986.

[17] Koutsopoulos, H. N., and Downey, A. B. Primitive-based classification of pavement cracking images. Journal of Transportation Engineering, 119, no. 3, pp. 402-418, 1993.

[18] Georgopoulos, A., Loizos, A., and Flouda, A. Digital image processing as a tool for pavement distress evaluation. ISPRS Journal of Photogrammetry and Remote Sensing, 50(1), pp. 23-33, 1995.

[19] Xu, B., Huang, Y. R. Development of an automatic pavement surface distress inspection system. Report No. FHWA/TX-05/7-4975-1, 2003.

[20] Wu, L., Mokhtari, S., Nazef, A., Nam, B., and Yun, H.B. Improvement of crack-detection accuracy using a novel crack defragmentation technique in image-based road assessment. Journal of Computing in Civil Engineering, 30(1), 04014118, 2014.

[21] Zou, Q., Cao, Y., Li, Q., Mao, Q., and Wang, S. CrackTree: Automatic crack detection from pavement images. Pattern Recognition Letters, 33(3), 227-238, 2012.

[22] Zhou, J., Huang, P. S., and Chiang, F. P. Wavelet-based pavement distress detection and evaluation. Optical Engineering, 45(2), 027007, 2006.

[23] Ying, L., and Salari, E. Beamlet transform based technique for pavement image processing and classification. In Electro/Information Technology, 2009. eit'09. IEEE International Conference on, pp. 141-145, IEEE, 2009.

[24] Subirats, P., Dumoulin, J., Legeay, V., and Barba, D. Automation of pavement surface crack detection using the continuous wavelet transform. In 2006 International Conference on Image Processing (pp. 3037-3040). IEEE, 2006.

[25] Abdel-Qader, I., Abudayyeh, O., and Kelly, M. E. Analysis of edge-detection techniques for crack identification in bridges. Journal of Computing in Civil Engineering, 17(4), 255-263, 2003.

[26] Ayenu-Prah, A., and Attoh-Okine, N. Evaluating pavement cracks with bidimensional empirical mode decomposition. EURASIP Journal on Advances in Signal Processing, 2008(1), 861701, 2008.

[27] Maode, Y., Shaobo, B., Kun, X., and Yuyao, H. Pavement crack detection and analysis for high-grade highway. In 2007 8th International Conference on Electronic Measurement and Instruments (pp. 4-548). IEEE, 2007.

[28] Song, K. Y., Petrou, M., and Kittler, J. Texture crack detection. Machine Vision and Applications, 8(1), 63-75, 1995.

[29] Hu, Y., and Zhao, C. X. A novel LBP based methods for pavement crack detection. Journal of pattern Recognition research, 5(1), 140-147, 2010.

[30] Koch, C., Georgieva, K., Kasireddy, V., Akinci, B., and Fieguth, P. A review on computer vision based defect detection and condition assessment of concrete and asphalt civil infrastructure. Advanced Engineering Informatics, 29(2), 196-210, 2015.

[31] Moussa, G., and Hussain, K. A new technique for automatic detection and parameters estimation of pavement crack. In 4th International Multi-Conference on Engineering Technology Innovation, IMETI, 2011.

[32] Nguyen, T. S., Avila, M., and Begot, S. Automatic detection and classification of defect on road pavement using anisotropy measure. In 2009 17th European Signal Processing Conference (pp. 617-621). IEEE, 2009.

[33] Mokhtari, S., Wu, L., and Yun, H. B. Comparison of supervised classification techniques for vision-based pavement crack detection. Transportation Research Record, 2595(1), 119-127, 2016.

[34] Gopalakrishnan, K., Khaitan, S. K., Choudhary, A., and Agrawal, A. Deep convolutional neural networks with transfer learning for computer vision-based data-driven pavement distress detection. Construction and Building Materials, 157, 322-330, 2017.

[35] Nhat-Duc, H., Nguyen, Q. L., and Tran, V. D. Automatic recognition of asphalt pavement cracks using metaheuristic optimized edge detection algorithms and convolution neural network. Automation in Construction, 94, 203-213, 2018.

[36] Zhang, L., Yang, F., Zhang, Y. D., and Zhu, Y. J. Road crack detection using deep convolutional neural network. In 2016 IEEE international conference on image processing (ICIP) (pp. 3708-3712). IEEE, 2016.

[37] Eisenbach, M., Stricker, R., Seichter, D., Amende, K., Debes, K., Sesselmann, M., and Gross, H. M. How to get pavement distress detection ready for deep learning? A systematic approach. In 2017 international joint conference on neural networks (IJCNN) (pp. 2039-2047). IEEE, 2017.

[38] Gopalakrishnan, K. Deep Learning in data-driven pavement image analysis and automated distress detection: A review. Data 3, no. 3: 28, 2018.

[39] Maeda, H., Sekimoto, Y., Seto, T., Kashiyama, T., and Omata, H. Road damage detection using deep neural networks with images captured through a smartphone. arXiv preprint arXiv: 1801.09454, 2018.

[40] Fan, Z., Wu, Y., Lu, J., and Li, W. Automatic pavement crack detection based on structured prediction with the convolutional neural network. arXiv preprint arXiv: 1802.02208, 2018.

[41] Wang, X., and Hu, Z. Grid-based pavement crack analysis using deep learning. In 2017 4th International Conference on Transportation Information and Safety (ICTIS), pp. 917-924. IEEE, 2017.

[42] Some, L. Automatic image-based road crack detection methods. 2016.

[43] Li, S., and Zhao, X. Image-based concrete crack detection using convolutional neural network and exhaustive search technique. Advances in Civil Engineering, 2019.

[44] Karlaftis, M., and Vlahogianni, E. Statistical methods versus neural networks in transportation research: Differences, Similarities and Some Insights. Transportation Research Part C: Emerging Technologies, Vol. 19, No. 3, pp. 387–399, 2011.

[45] Kim, M., Burton, Y. M., Prozzi, J. A., and Murphy, M. Maintenance and rehabilitation project selection using artificial neural networks. Transportation Research Board 93rd Annual Meeting, No. 14-3620, 2014.

[46] Plati, C., Georgiou, P. and Papavasiliou, V. Simulating pavement structural condition using artificial neural networks. Structure and Infrastructure Engineering, pp. 1–10, 2015.

[47] Leverington, D. A basic introduction to feedforward backpropagation neural networks. Neural Network Basics, 2012.

[48] Kandahl, P. S., and Richards, I. J. Premature Failure of Asphalt Overlays from Stripping: Case Studies, NCAT Report No. 01-01, National Center for Asphalt Technology, Auburn, AL, 2001.

[49] Little, D., and D. Jones. Chemical and Mechanical Processes of Moisture Damage in Hot-Mix Asphalt Pavements. Moisture Sensitivity of Asphalt Pavements -A National Seminar California Department of Transportation; Federal Highway Administration; National Asphalt Pavement Association; California Asphalt Pavement Alliance; and Transportation Research Board., 2003.

[50] Hicks, R. G. NCHRP Synthesis 175: Moisture Damage in Asphalt Concrete. Transportation Research Board, Washington, D.C., 1991.

[51] Sebesta, S., T. Saarenketo, and T. Scullion. SHRP 2 Report S2-R06C-RR-1: Using Infrared and High- Speed Ground Penetrating Radar for Uniformity Measurements on New HMA Layers. Transportation Research Board, Washington, D.C., 2013.

[52] Celaya, M., and S. Nazarian. Stripping Detection in Asphalt Pavements with Seismic Methods. Transportation Research Record: Journal of the Transportation Research Board, Vol. 2005, No. 1, pp. 64–74, 2007.

[53] Ferry, J. D. Viscoelastic properties of polymers. John Wiley & Sons, 1980.

[54] Hoegh, K., L. Khazanovich, and H. T. Yu. Ultrasonic Tomography Technique for Evaluation Concrete Pavements. Transportation Research Record: Journal of the Transportation Research Board, No. 2232, pp. 85–94, 2011.

[55] Germann Instruments. http://germann.org/products-by-application/flaw-detection/mira. Accessed Nov. 10, 2017.

[56] Federal Highway Administration. https://www.fhwa.dot.gov/pavement/concrete/ultrasonic.cfm. Accessed Nov. 10, 2017.

[57] Al-Qadi, I. L., and S. Lahouar. Measuring layer thicknesses with GPR - Theory to practice. Construction and Building Materials, Vol. 19, No. 10, pp. 763–772, 2005.

[58] Adcock, A. D., W. C. Dass, and J. W. I. Rish. Ground penetrating radar for airfield pavement evaluations. Nondestructive Evaluation of Aging Aircraft, Airports, Aerospace Hardware, and Materials, Vol. 2455, pp. 373-384. https://doi.org/10.1117/12.213553, 1995.

[59] Pellinen, T., P. Eskelinen, E. Huuskonen-Snicker, and A. Hartikaine. Assessment of air void content of asphalt using dielectric constant measurements by GPR and with VNA, 2015.

[60] Roimela. Päällystetutkatutkimukset 1996-1997. 1998.

[61] SIR 30 - GSSI. http://www.geophysical.com/sir30.htm. Accessed Nov. 12, 2017.

[62] Geophysical Survey Systems Inc. RADAN 6.5 User's Manual. 2007.

[63] Chen, C., & Zhang, J. A review on GPR applications in moisture content Determination and pavement condition assessment. In Characterization, Modeling, and Performance of Geomaterials: Selected Papers From the 2009 GeoHunan International Conference (pp. 138-143), 2009.

[64] Hammons, M., H. Von Quintus, G. Geary, P. Wu, and D. Jared. Detection of Stripping in Hot-Mix Asphalt. Transportation Research Record, Vol. 1949, pp. 20–31, 2006.

[65] Khamzin, A. K., A. V. Varnavina, E. V. Torgashov, N. L. Anderson, and L. H. Sneed. Utilization of air-launched ground penetrating radar (GPR) for pavement condition assessment. Construction and Building Materials, Vol. 141, pp. 130–139, 2017.

[66] Stubstad, R.N. NCHRP Web Document 52: LTPP data analysis: feasibility of using FWD deflection data to characterize pavement construction quality. Transportation Research Board, Washington, D.C., 2002.

[67] Jahanshahi, M. R., Kelly, J. S., Masri, S. F., and Sukhatme, G. S. A survey and evaluation of promising approaches for automatic image-based defect detection of bridge structures. Structure and Infrastructure Engineering, 5(6), 455-486, 2009.

[68] Krizhevsky, A., Sutskever, I., and Hinton, G. E. Imagenet classification with deep convolutional neural networks. In Advances in neural information processing systems, pp. 1097-1105, 2012.

[69] Deng, X., Q. Liu, Y. Deng, and Mahadevan, S. An improved method to construct basic probability assignment based on the confusion matrix for classification problem. Information Sciences, Vol. 340-341, pp. 250–261, 2016.

[70] Abedin, T., Chowdhury, Z., Afzal, A.R., and Turin, T.C. Application of Binary Logistic Regression in Clinical Research. JNHFB, Vol. 5: 8-11, 2016.

[71] Peng, C. Y. J., Lee, K. L., & Ingersoll, G. M. An introduction to logistic regression analysis and reporting. The journal of educational research, 96(1), 3-14, 2002.

[72] Hastie, T. J., Tibshirani, R. J., and Friedman, J. The Elements of Statistical Learning – Data Mining, Inference and Prediction (2nd ed.), New York, USA: Springer, 2009.

[73] Cleveland, W.S. and Devlin, S. J. Locally Weighted Regression: An Approach to Regression Analysis by Local Fitting. Journal of the American Statistical Association, 83(403), 596-610, 1988.

[74] Rodriguez, G. Smoothing and Non-Parametric Regression, 2001. Available at https://data.princeton.edu/eco572/smoothing.pdf. Accessed June 15, 2019.

[75] Friedman, J., Hastie, T., and Tibshirani, R. The elements of statistical learning (Vol. 1, No. 10), New York: Springer series in statistics, 2001.

[76] Warren, C., Giannopoulos, A., and Giannakis, I. gprMax: Open source software to simulate electromagnetic wave propagation for Ground Penetrating Radar. Computer Physics Communications, 209, 163-170, 2016.

[77] Elhadidy, A. A., S. M. El-Badawy, and E. E. Elbeltagi. A simplified pavement condition index regression model for pavement evaluation, International Journal of Pavement Engineering, 2019. DOI: 10.1080/10298436.2019.1633579.

[78] Louisiana DOTD Distress Identification Protocols for Asphalt and Composite Pavements. DOTD, 2018.

[79] Izeppi, E. D., Morrison, A., Flintsch, G. W., and Mcghee, K. K. Best Practices and Performance Assessment for Preventive Maintenance Treatments for Virginia Pavements. Final Contract, 2015. Virginia Tech Transportation Institute.

[80] Khattak, M. J., Baladi, G. Y., and Sun, X. Development of Index Based Pavement Performance Models for Pavement Management System (PMS) of LADOTD. FHWA/LA.08/460, 2009.

[81] Chen, X., H. Zhu, Q. Dong, and B. Huang .Case study: Performance effectiveness and cost-benefit analyses of open-graded friction course pavements in Tennessee. Int. J. Pavement Eng., 2016. pp.1-14. doi 10.1080 /10298436.2016.1138112, 1–14.

[82] Irfan, M., M. Khurshid, S. Labi, and W. Flora. Evaluating the Cost Effectiveness of Flexible Rehabilitation Treatment Using Different Performance Criteria. Journal of Transportation Engineering, 2009. 135 (10), pp.753-736.

[83] DOTD. Louisiana DOTD Distress Identification Protocols for Asphalt & Composite Pavements, 2018.

[84] Krizhevsky, A., I. Sutskever, and G. E. Hinton. ImageNet Classification with Deep Convolutional Neural Networks. Advances in neural information processing systems, 2012.1097-1105.

[85] Paul, S. Pattern Recognition Algorithms for Multi-Omics Data Analysis. Reference Module in Biomedical Sciences. 2020. doi:10.1016/B978-0-12-801238-3.11538-7.

[86] Elbagalati, O., M. A. Elseifi, K. Gaspard, and Z. Zhang. Development of an Enhanced Decision-Making Tool for Pavement Management using a Neural Network Pattern Recognition Algorithm, 2018. 144(2). doi:10.1061/JPEODX.0000042.

[87] Abedin, T., Z. Chowdhury, A. R. Afzal, F. Yeasmin, and T. C. Turin. Application of Binary Logistic Regression in Clinical Research. JNHFB, 2016. 5, pp.8-11.

[88] Cokluk, O. Logistic Regression: Concept and Application. Educational Sciences: Theory & Practice, 2010. 10(3), pp. 1397-1407.

[89] Wedagama, D. P.A Multinomial Logit Model for Estimating the Influence of household Characteristics on Motorcycle Ownership: A Case Study in Denpasar City, Bali. Journal of Civil Engineering, 2009. 29(1).

[90] Rezapour, M., and K. Ksaibati. Application of multinomial and ordinal logistic regression to model injury severity of truck crashes, using violation and crash data. J. Mod. Transport, 2018. 26(7), pp. 268–277. doi: 10.1007/s40534-018-0166-x.

[91] Patrick, G., and Soliman, H. Roughness Prediction Models using Pavement Surface Distresses in Different Canadian Climatic Regions. Canadian Journal of Civil Engineering, 2019.46(10), pp. 934-940. doi:10.1139/cjce-2018-0697, 2019.

[92] El-Badawy, S. M., F. M. Bayomy, and M. Santi .Regional Calibration of the MEPDG Rutting Models – Idaho Case Study. Ankara, Turkey: 10th International Congress on Advances in Civil Engineering, 2012.

[93] AASHTO. Guide for the Local Calibration of the Mechanistic-Empirical Pavement Design Guide. Washington, DC, United States, 2010.

This public document is published at a total cost of $200.
29 copies of this public document were published in this first printing at a cost of $200. The total cost of all printings of this document including reprints is $200. This document was published by Louisiana Transportation Research Center to report and publish research findings as required in R.S. 48:105. This material was duplicated in accordance with standards for printing by state agencies established pursuant to R.S. 43:31. Printing of this material was purchased in accordance with the provisions of Title 43 of the Louisiana Revised Statutes.